Title

Fifteen years of XMM–Newton and Chandra monitoring of Sgr A ★ : evidence for a recent increase in the bright flaring rate

Journal

Monthly Notices of the Royal Astronomical Society, 454(2)

ISSN

0035-8711

Authors

Ponti, G
De Marco, B
Morris, MR
et al.

Publication Date

2015-12-01

DOI

10.1093/mnras/stv1537

Peer reviewed

MNRAS **453,** 172–213 (2015) doi:10.1093/mnras/stv1331

The *XMM–Newton* view of the central degrees of the Milky Way

G. Ponti,[1⋆] M. R. Morris,[2] R. Terrier,[3] F. Haberl,[1] R. Sturm,[1] M. Clavel,[3,4] S. Soldi,[3,4] A. Goldwurm,[3,4] P. Predehl,[1] K. Nandra,[1] G. Bélanger,[5] R. S. Warwick[6] and V. Tatischeff[7]

[1]*Max Planck Institut für Extraterrestrische Physik, D-85748 Garching, Germany*
[2]*Department of Physics and Astronomy, University of California, Los Angeles, CA 90095-1547, USA*
[3]*Unité mixte de recherche Astroparticule et Cosmologie, 10 rue Alice Domon et Léonie Duquet, F-75205 Paris, France*
[4]*Service d'Astrophysique (SAp), IRFU/DSM/CEA-Saclay, F-91191 Gif-sur-Yvette Cedex, France*
[5]*ESA/ESAC, PO Box 78, E-28691 Villanueva de la Cañada, Spain*
[6]*Department of Physics and Astronomy, University of Leicester, University Road, Leicester LE1 7RH, UK*
[7]*Centre de Sciences Nucléaires et de Sciences de la Matière, IN2P3-CNRS and Univ Paris-Sud, F-91405 Orsay Cedex, France*

Accepted 2015 June 12. Received 2015 June 12; in original form 2015 January 16

ABSTRACT

The deepest *XMM–Newton* mosaic map of the central 1.°5 of the Galaxy is presented, including a total of about 1.5 Ms of EPIC-pn cleaned exposures in the central 15 arcsec and about 200 ks outside. This compendium presents broad-band X-ray continuum maps, soft X-ray intensity maps, a decomposition into spectral components and a comparison of the X-ray maps with emission at other wavelengths. Newly discovered extended features, such as supernova remnants (SNRs), superbubbles and X-ray filaments are reported. We provide an atlas of extended features within $\pm 1^{\circ}$ of Sgr A⋆. We discover the presence of a coherent X-ray-emitting region peaking around G0.1−0.1 and surrounded by the ring of cold, mid-IR-emitting material known from previous work as the 'Radio Arc Bubble' and with the addition of the X-ray data now appears to be a candidate superbubble. Sgr A's bipolar lobes show sharp edges, suggesting that they could be the remnant, collimated by the circumnuclear disc, of an SN explosion that created the recently discovered magnetar, SGR J1745−2900. Soft X-ray features, most probably from SNRs, are observed to fill holes in the dust distribution, and to indicate a direct interaction between SN explosions and Galactic centre (GC) molecular clouds. We also discover warm plasma at high Galactic latitude, showing a sharp edge to its distribution that correlates with the location of known radio/mid-IR features such as the 'GC Lobe'. These features might be associated with an inhomogeneous hot 'atmosphere' over the GC, perhaps fed by continuous or episodic outflows of mass and energy from the GC region.

Key words: plasmas – methods: data analysis – ISM: bubbles – ISM: kinematics and dynamics – ISM: supernova remnants – Galaxy: centre.

1 INTRODUCTION

At a distance of only ∼8 kpc, the centre of the Milky Way is the closest Galactic nucleus, allowing us to directly image, with incomparable spatial resolution, the physical processes typical of galactic nuclei. The central region of the Galaxy is one of the richest laboratories for astrophysics (Genzel, Eisenhauer & Gillessen 2010; Morris, Meyer & Ghez 2012; Ponti et al. 2013). Within the inner ∼200 pc about 3–5 × 10^7 $M_{\odot}$ of molecular material are concentrated, the so-called Central Molecular Zone (CMZ). This corresponds to about 1 per cent of the molecular mass of the entire Galaxy and it is concentrated in a region of about $\sim 10^{-6}$ of its volume (Morris & Serabyn 1996). In this region many thousands of persistent and transient point-like X-ray sources are embedded, such as active stars, bright accreting binary systems (and many more quiescent massive bodies) and cataclysmic variables, which have been beautifully imaged thanks to the superior spatial resolution of *Chandra* (Wang et al. 2002; Muno et al. 2003, 2009). One of the best jewels in the GC is Sgr A⋆, the electromagnetic counterpart of the closest supermassive black hole (BH; Genzel et al. 2010). In addition to this large population of point sources, extended X-ray sources, such as supernova remnants (SNRs), non-thermal filaments, pulsar wind nebulae, and massive star clusters populate

⋆E-mail: ponti@iasfbo.inaf.it, ponti@mpe.mpg.de

the GC (Wang et al. 2002). The GC is considered a mini-starburst environment, giving us the possibility of studying the interaction between SNRs and molecular clouds and the impact of massive-and-young star clusters on their surroundings. It allows us to image, in superb detail, the creation and evolution of bubbles and super-bubbles and the generation of Galactic outflows, powered by past starbursts and/or accretion events on to Sgr A*, and their impact on the GC environment.

Warm ($kT \sim 1$ keV) and hot ($kT \sim 6.5$ keV) thermal plasma emission plus non-thermal hard X-ray emission associated with X-ray reflection nebulae (see Ponti et al. 2013 for a review) pervade the central region, producing a high background of soft and hard X-ray radiation. About 90 per cent (Ebisawa et al. 2001; Wang et al. 2002) of the soft X-ray emission appears to be due to a diffuse, patchy and thermal component (Bamba et al. 2002) with a temperature $kT \sim 1$ keV, most probably associated with SNRs. The origin of the hot component is, instead, still highly debated. At $\sim 1^\circ.5$ from the GC, $\sim$80 per cent of this emission has been resolved into point sources (e.g. accreting white dwarfs and coronally active stars) by a deep *Chandra* observation (Revnivtsev et al. 2009). Although the intensity of the hot-plasma emission increases rapidly towards the GC, point sources continue to make a substantial contribution to the observed hard emission (Muno et al. 2004; Heard & Warwick 2013a). Additionally, some of the emission may arise due to scattering of the radiation from bright X-ray binaries by the dense interstellar medium (Sunyaev, Markevitch & Pavlinsky 1993; Molaro, Khatri & Sunyaev 2014). Nevertheless, it is not excluded that a truly diffuse hot-plasma component is also present in the GC (Koyama et al. 2009; Uchiyama et al. 2013). Such hot plasma would be unbound to the Galaxy and it would require a huge energy ($E \sim 10^{55}$ erg) and energy loss rate of the mass outflow of $\sim 10^{43}$ erg s^{-1}, corresponding to a rate of 1 supernova/yr, to continuously replenish it (Tanaka 2002). However, it has recently been proposed that such hot plasma might be trapped by the GC magnetic field (Nishiyama et al. 2013).

Indeed, the magnetic field is thought to be an important ingredient of the GC environment. The first high-resolution radio images of the Milky Way centre (see the bottom panel of Fig. 6), revealed the presence of many straight, long (up to $\sim$20–30 pc) and thin (with width $\lesssim$0.1 pc), linearly polarized vertical filaments with spectral index consistent with synchrotron radiation (Yusef-Zadeh, Morris & Chance 1984; Yusef-Zadeh et al. 1987a,b; Anantharamaiah et al. 1991; Lang, Morris & Echevarria 1999; LaRosa et al. 2000). These filaments are hypothesized to be magnetic flux tubes trapping energetic electrons and therefore tracing the diffuse interstellar GC poloidal magnetic field (Morris & Yusef-Zadeh 1985; Lang et al. 1999). A staggeringly powerful poloidal magnetic field pervading the GC, with a field strength of $B \gtrsim 50\,\mu$G, and very possibly $B \sim 1$ mG, has been inferred (Morris 1990; Crocker et al. 2010; Ferrière et al. 2011). The details of the physical process creating the filaments and energising the magnetic field are still debated; however, it appears clear that the magnetic filaments are interacting with the ionized surfaces of massive molecular clouds.

Recent far-infrared/sub-millimetre polarization studies of thermal dust emission made it possible to probe the direction of the interstellar magnetic field inside dense molecular clouds. The magnetic field threading GC molecular clouds is measured to be parallel to the Galactic plane (Chuss et al. 2003; Novak et al. 2003; Nishiyama et al. 2009). Therefore, it appears that the large-scale GC magnetic field is poloidal in the diffuse interstellar medium and toroidal in dense regions in the plane. If the strength of the diffuse magnetic field is on the high side ($B \sim 1$ mG) a huge amount of magnetic energy, $E \sim 10^{55}$ erg, would be stored in the central $\sim$300 pc. This is comparable to the kinetic energy associated with the rotation of the gas in the CMZ. Therefore, it is thought to be a key player for the GC physics and phenomenology.

A large-scale structure with a possible magnetic origin and appearing to be interacting with massive clouds of the CMZ (similar to the non-thermal filaments) is the Galactic centre lobe (GCL). The GCL has a limb-brightened shell structure in the 10.5 GHz map, defined primarily by two spurs (see figs 1 and 2 of Law et al. 2009). The eastern one arises from the location of the GC Radio Arc,[1] while the second starts from the Sgr C thread. It was proposed that the GCL is produced by channelling of plasma from the Galactic plane, induced by energetic GC activity (e.g. episode of AGN activity, or a large mass outflow due to the high star formation rate, etc.; see Law, Brentjens & Novak 2011) or from twisting of poloidal magnetic field lines by Galactic rotation (Sofue et al. 1984, 1985; Uchida 1985, 1990; Shibata 1989). Located at the western limb of the GCL is an interesting feature, AFGL 5376 (Uchida et al. 1994), an unusually warm, shock heated and extended IR source, thought to be associated with the GCL.

All major X-ray telescopes devoted a significant fraction of their time to the study of the GC. *Chandra* invested several Ms to monitor both Sgr A*'s activity (Baganoff et al. 2001, 2003; Neilsen et al. 2013) as well as diffuse soft and hard X-ray emission (Wang et al. 2002; Park et al. 2004). *Suzaku* and *Swift* also performed large observational campaigns to scan the Milky Way centre (Koyama et al. 2007; Degenaar & Wijnands 2010) and monitor the transients in the region (Degenaar et al. 2012). The study of the GC is one of the key programmes of the *NuSTAR* mission (Harrison et al. 2013; Mori et al. 2013; Barrière et al. 2014). *XMM–Newton* completed a first shallow ($\sim$30 ks total cleaned exposure in each point) scan of the CMZ within a couple of years after launch (see the conference proceedings: Decourchelle et al. 2003; Sakano et al. 2003, 2004). A larger amount of time (more than $\sim$1.5 Ms) has been invested by *XMM–Newton* on studying the emission properties of Sgr A* (Goldwurm et al. 2003; Porquet et al. 2003, 2008; Bélanger et al. 2005; Trap et al. 2011; Mossoux et al. 2014), focusing on the central $\sim$15 arcmin, only. Using the *XMM–Newton* observations from the shallow scan of the CMZ together with a number of the Sgr A* pointings, Heard & Warwick (2013a,b) have investigated the distribution of the X-ray emission within the central region of the Galaxy. With the aim of studying the propagation of echoes of the past GC activity within the CMZ (Sunyaev et al. 1993; Koyama et al. 1996, 2008; Revnivtsev et al. 2004; Muno et al. 2007; Inui et al. 2009; Ponti et al. 2010, 2013; Terrier et al. 2010; Capelli et al. 2011, 2012; Nobukawa et al. 2011; Clavel et al. 2013, 2014; Ryu et al. 2013; Krivonos et al. 2014), recently, a new deep (with $\sim$100 ks exposure at each location) *XMM–Newton* scan of the CMZ has been completed (in fall 2012). We present here the combined images of both the new and old *XMM–Newton* scans, as well as all the *XMM–Newton* observations within the central degree of the Galaxy.

In Section 2, we present the data reduction process and the key steps to produce the GC EPIC mosaic maps. Section 3 introduces the broad-band X-ray images, discussing the (transient) emission from the brightest point sources, the contribution from the foreground emission, as well as the soft and hard GC diffuse emission. In Section 4, the narrow-band images at the energies of the soft X-ray lines are displayed. Section 5 presents a new technique of

[1] This is a well-known radio feature (see Fig. 6) composed of an array of straight, long, thin and linearly polarized vertical filaments, indicating the importance of the GC magnetic field.

spectral-imaging decomposition of the soft X-ray emission into three physical components. Section 6 presents an atlas of all the new and known diffuse features within the surveyed area. Section 7 presents the comparison with the distribution of column density of intervening matter. Discussion and conclusions are in Sections 8 and 9, respectively. Hereafter, unless otherwise stated, we will state all locations and positions in Galactic coordinates and Galactic cardinal points. Errors are given at 90 per cent confidence for one interesting parameter.

2 DATA REDUCTION AND CLEANING

The new *XMM–Newton* CMZ scan has been performed in 2012 starting on August 30 and ending on October 10. It comprises of 16 *XMM–Newton* (Jansen et al. 2001) observations all performed with all the EPIC instruments in full-frame CCD readout mode with the medium optical blocking filters applied (we refer to Tables A1 and A2 for more details on the instruments set-ups).

This paper is not limited to the use of the 2012 *XMM–Newton* scan of the CMZ. Instead, it is using all *XMM–Newton* observations pointed within 1° from Sgr A*. Therefore we combined the 16 observations of the new CMZ scan with the 14 observations of the previous CMZ scan accumulated between 2000 and 2002. We also include the 30 observations pointing at Sgr A* and other 49 observations aimed at studies of different sources in the vicinity of Sgr A* (see Tables A1 and A2).

We performed the analysis of the EPIC data with the version 13.0.0 of the *XMM–Newton* Science Analysis System (SAS). Periods of increased particle background have been removed from the data. To perform this, we first selected the good time intervals (GTIs) starting from the 7–15 keV background light curves, then we applied a threshold of 8 and 2.5 counts ks^{-1} arcmin^{-2} for EPIC pn (Strüder et al. 2001) and EPIC MOS (Turner et al. 2001), respectively (see e.g. Haberl et al. 2012). The chosen thresholds efficiently cut out all the periods of most extreme activity of soft proton flares. We noted, however, that an enhanced, but weak, background activity was still present in the data during several observations. Because of the non-uniform distribution of the GC diffuse emission, lowering the threshold uniformly in all observations, would result in cutting truly GTIs in observations with higher GC diffuse emission. Thus we decided to visually inspect the background light curve of all data sets and select a different threshold for each observation (see Tables A1 and A2). Such as in Haberl et al. (2012), when the data from several detectors were available, we combined the GTIs using only common time intervals, otherwise we included GTIs of the single detector. Most of the 2012 CMZ scan data were affected by negligible particle flaring activity. On the other hand, many of the previous observations have been severely affected by soft proton flares (see the reduction in exposure in Tables A1 and A2).

To prevent infrared, optical and UV photons from bright sources in the field of view that would increase the noise and degrade the CCD energy scale, the different *XMM–Newton* observations have been performed with different filters applied, according to the optical–UV brightness of the sources in the field of view (see Tables A1 and A2). In particular, we used the filter wheel closed observations to remove the internal EPIC background.

2.1 Images and exposure maps

Images and exposure maps, corrected for vignetting, have been produced with an image pixel size of 2 arcsec × 2 arcsec for each energy band (for the definition of all bands, see Section 2.2). To increase the sky coverage, we selected EPIC-pn events requiring (FLAG & 0xfa0000) = 0, which also includes events in pixels next to bad pixels or bad columns. Moreover, we used single to double pixel events. EPIC-MOS events were required to have FLAG = 0 and single to quadruple-pixel events were allowed.

Fig. 1 shows the combined EPIC exposure map that covers the entire CMZ. Such as done in Sturm et al. (2013), EPIC-MOS1 and -MOS2 exposures are weighted by a factor of 0.4 relative to EPIC-pn, before being added to the latter, to account for the lower effective area. Therefore, the exposure times obtained correspond to the equivalent total EPIC-pn exposure time. This allows us to obtain a better combination of EPIC-pn and EPIC-MOS data for image display purposes. We note, however, that the fluxes cannot be easily read out directly from these combined images. Therefore, the line profiles and the measured fluxes/luminosities are computed from the EPIC-pn and each EPIC-MOS map separately and then combined (averaged) to obtain a better signal to noise.

The top panel of Fig. 1 shows that more than 1.5 Ms of *clean* (after cut of time intervals during increased particle background activity) exposure time (EPIC-pn equivalent) has been accumulated on Sgr A* and over ∼100–200 ks are present in each point of the CMZ. The few pointings above and below the plane have exposures between ∼15and40 ks. Regions with less than 7.2 ks of equivalent EPIC-pn exposure have been masked out.

To check the impact of the bright transients on the images and on the physical quantities under investigation, two sets of maps have been created. The first series keeps all bright transients and point sources, while the second set removes their emission by excising from the data extended regions including the transients whenever they were in outburst (see Section 3.1). The middle and bottom panels of Fig. 1 show the exposure maps (computed in the same way) for the observations of new and old CMZ scans, separately. The maximum exposure times are ∼190 and ∼45 ks during the new and old scan, respectively.

2.2 Energy bands

We created images in several energy bands (see Table 1). Fig. 2 shows the EPIC-pn spectra of the extended emission from several regions within the CMZ. In red and black are the spectra from the *G0.11−0.11* and *Center Superbubble* regions, respectively (see Fig. 6). Both regions are located within 15 arcmin from Sgr A*, thus they have excellent statistics because of the large exposure. In green and blue are the pn spectra of *G0.687−0.146* and *Sgr B1 soft*, respectively, both are located further out, thus having lower exposure.

We first selected the standard broad energy bands for the continuum with the softer band being: E = 0.5–2 keV; the medium 2–4.5 keV and the hard 4.5–12 keV (see Table 1). We note that, at high energies, the EPIC-pn camera shows strong instrumental background emission lines due to Ni K α (at E ∼7.47 keV), Cu K α (∼8.04 keV) and ZnCu (∼8.63 and 8.87 keV) that strongly contribute to the observed X-ray emission in the hard band (see Freyberg et al. 2004). To avoid contamination from these strong internal background lines, we do not consider (for the EPIC-pn images) photons in the 7.2–9.2 keV range (see Fig. 2 and Table 1). We chose these broad energy bands because they are typically used as input by the standard *XMM–Newton* point source detection algorithm and for comparison to other similar surveys of nearby galaxies (e.g. M33: Misanovic et al. 2006; Tüllmann et al. 2011; M31: Henze et al. 2014; Stiele et al. 2011; LMC: Haberl et al. 1999; SMC: Haberl et al. 2012; Sturm et al. 2013). However we note that,

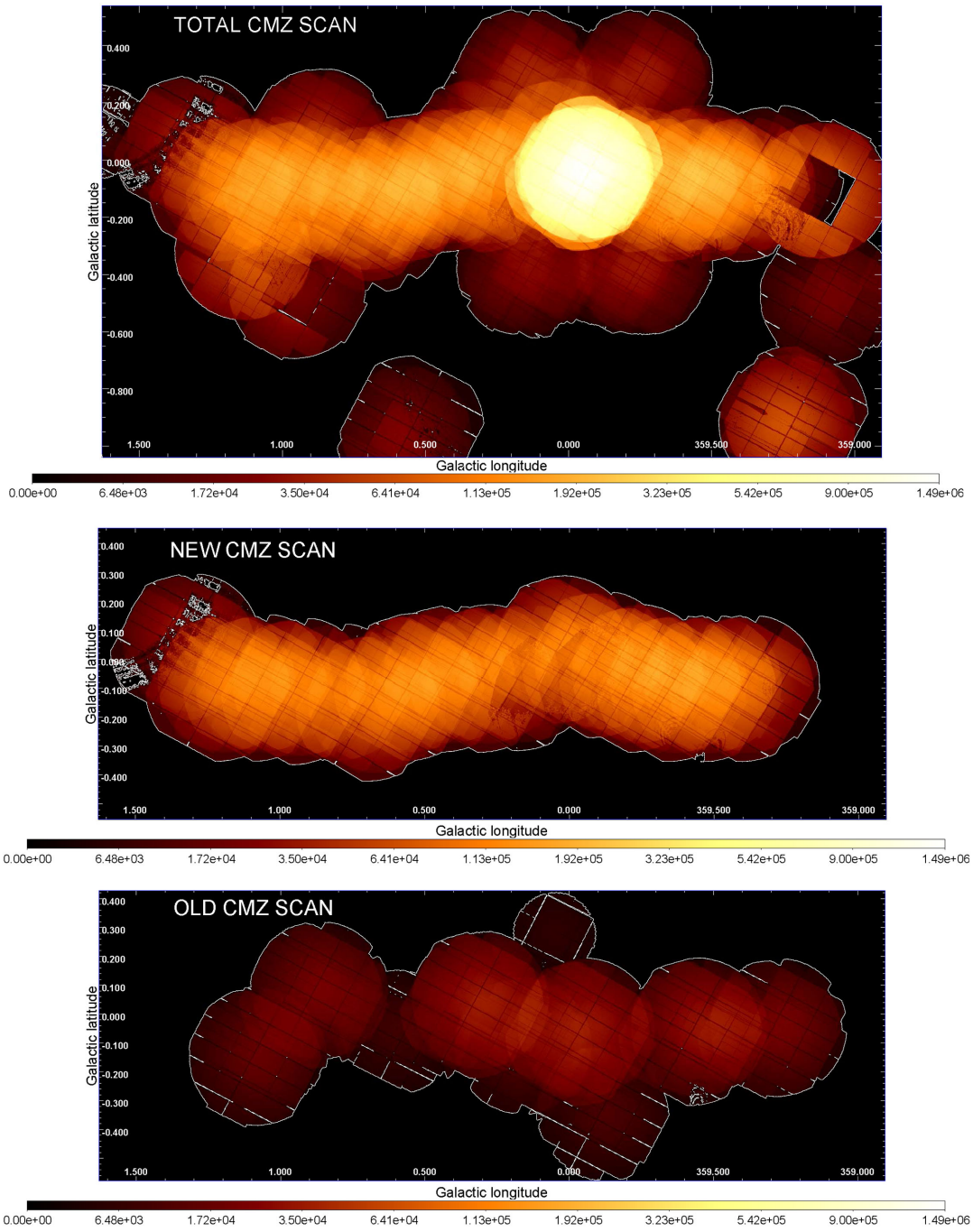

Figure 1. Top panel: combined exposure map of all the *XMM–Newton* EPIC-pn + MOS1 + MOS2 observations within 1° from Sgr A*. Such as done in Sturm et al. (2013), EPIC-MOS1 and -MOS2 exposure is weighted by a factor of 0.4 relative to EPIC-pn to account for the lower effective area. The exposure times, thus, correspond to the equivalent total EPIC-pn exposure time. Regions with less than 7.2 ks of equivalent EPIC-pn exposure have been masked out. The cleaned EPIC-pn equivalent exposure time is reported in seconds. Medium panel: similar exposure map for the observations of the new CMZ scan only. Bottom panel: similar exposure map for the old CMZ scan only (regions with less than 7.2 ks of equivalent EPIC-pn exposure are included). The maximum exposure times are ∼1.5 Ms, ∼190 ks and ∼45 ks during the total, new and old scan, respectively.

given the typical GC neutral column density of several 10^{22} cm^{-2}, the low-energy absorption cut-off occurs at the highest energies of the standard soft band, making standard broad-band RGB images poorly sensitive to column density fluctuations. For this reason we define a second set of broad-bands, the 'GC continuum bands' (see Table 1). The first band (E = 0.5–1.5 keV) contains mainly emission from foreground sources. The second band (E = 1.5–2.6 keV) is selected in order to contain the low-energy GC neutral absorption cut-off, thus making it more sensitive to either column density or soft gas temperature variations. While the 'GC medium' (E = 2.6–4.5 keV) and the 'GC hard' (E = 4.5–12 keV) bands are similar to the standard broad-bands.

We also selected images at the energies of the soft emission lines, such as Si XIII, S XV, Ar XVII and Ca XIX. To perform continuum

Table 1. Energy bands used for each of the different continuum, and narrow line images. Also shown are the energy bands used to determine the continuum underlying the line emission. Units are in keV. Several energy bands, at lower energies compared to the Fe K lines, have been computed to determine the best continuum subtraction for the Fe K lines.

Standard continuum bands:				
Soft	Medium	Hard[a]		
0.5–2	2–4.5	4.5–12		
GC continuum bands:				
Fore	GC soft	GC medium	GC hard[a]	
0.5–1.5	1.5–2.6	2.6–4.5	4.5–12	
Soft emission lines:				
Si XIII	S XV	Ar XVII	Ca XIX	
1.80–1.93	2.35–2.56	3.03–3.22	3.78–3.99	
Continuum subtraction soft emission lines:				
Red–Si	Si–S	S–Ar	Ar–Ca	Blue–Ca
1.65–1.77	2.1–2.3	2.7–2.97	3.27–3.73	4.07–4.5
Fe K lines:				
Fe K α	Fe XXV			
6.3–6.5	6.62–6.8			
Continuum subtraction Fe K:				
CFe K	CsFe K soft	CmFe K medium	ChFe K hard	
5–6.1	4.0–4.7	4.7–5.4	5.4–6.1	

[a]To avoid contribution from the strong internal detector background emission lines, present in the EPIC-pn camera (such as Ni K α, Cu K α and ZnCu), we do not consider photons in the 7.2–9.2 keV from this instrument (on the other hand, we consider such photons detected in the EPIC-MOS cameras).

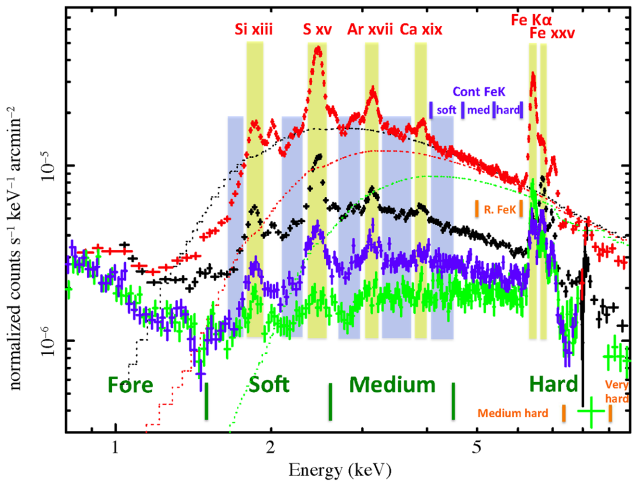

Figure 2. EPIC-pn spectra of the regions: G0.11−0.11 (red), Center Superbubble (black), G0.687−0.146 (green) and Sgr B1 soft (blue). In dark green are the energy bands of the broad GC continuum. In orange (bottom right) is shown the part of the hard energy band excluded in order to avoid contamination by Ni K α, Cu K α and ZnCu instrumental background emission lines. Yellow stripes show the energy bands of the soft and Fe K emission lines. Blue stripes indicate the regions selected for the determination of the amount of continuum underlying the soft lines. The dotted lines, from top to bottom, show the predicted emission of a source with a power-law spectrum (with slope $\Gamma = 1.6$) if absorbed by a column density of $N_{\rm H} = 3$, 5 and 9×10^{22} cm^{-2}, respectively. The blue and orange labels indicate the selected broad energy bands for the determination of the continuum underlying the Fe K line emission.

subtracted line intensity maps as well as line equivalent width maps, it is essential to measure the level of the continuum underlying the emission line. Therefore, we created also several images in energy bands on each side of the soft emission lines[2] (selecting, as far as possible, energy ranges free from line emission; see Fig. 2 and Table 1).

In the Fe K region we selected two energy bands for the Fe K α and Fe XXV emission. At energies higher than Fe XXV the presence of both Fe K β, Fe XXVI, and of the Fe K edge can give a significant contribution. At even higher energies ($E \sim 7.5$–8 keV) the contribution from internal background emission line (in the EPIC-pn camera) becomes very important, thus we decided to determine the continuum emission underlying the Fe K line emission (important to determine the Fe K line intensities and equivalent widths) through the extrapolation of the continuum redwards of the Fe K lines (see Fig. 2 and Table 1). The Fe K line emission and its variations will be the prime scientific focus of two future publication (Ponti et al. in preparation; Soldi et al. in preparation; see also Ponti et al. 2014; Soldi et al. 2014) and will not be discussed here any further.

All images were exposure corrected and, to remove readout streaks, the images from EPIC-pn were corrected for out-of-time (OoT) events. Noisy CCDs in the MOS data (Kuntz & Snowden 2008) have been searched with the SAS task *emtaglenoise* and removed from the mosaic images.

2.2.1 *Stray-light rejection*

Because the GC region is crowded with many bright (transient) X-ray sources, several observations, including the new *XMM–Newton* scan, are badly affected by stray light (see Fig. 3). Stray light is produced by photons from sources located outside of the *XMM–Newton* EPIC instrument's fields of view and singly reflected by the mirror hyperbolas, thus creating concentric arc-like structures in the detector plane (see *XMM–Newton* user handbook). The stray-light contribution is small (the effective collecting area for stray light is less than ∼0.2 per cent of the effective on-axis area), but a very bright source can have an important impact up to ∼1°.4 outside the field of view.

Analogously to the removal of bright transients, we masked the strongest stray-light artefacts in the images of individual observations. In most cases, affected regions are covered by other unaffected observations, thus leaving no features in the final mosaic map. To remove a stray-light artefact, we defined a rough region including the artefact and an individual cut-off value of the surface brightness. Using this cut-off, we created a mask from an image of this region in the total energy band that has been smoothed with a Gaussian kernel with an FWHM of 10 arcsec beforehand. This mask was multiplied by all images and exposure maps of this observation.

2.2.2 *Adaptive smoothing*

All images have been smoothed separately using the SAS tool ASMOOTH. To prevent different smoothing patterns from introducing colour artefacts in RGB images, we adaptively smoothed all energy bands in such images with the same smoothing template. For the broad-band *XMM–Newton* continuum RGB images (see Figs 3–9), we required a minimum signal-to-noise ratio of 6 in the 0.5–12 keV

[2] The energy band redwards of the Si XIII line extends only down to 1.65 keV, because of the presence of the strong Al K α background emission line at $E \sim 1.49$ keV (Freyberg et al. 2004).

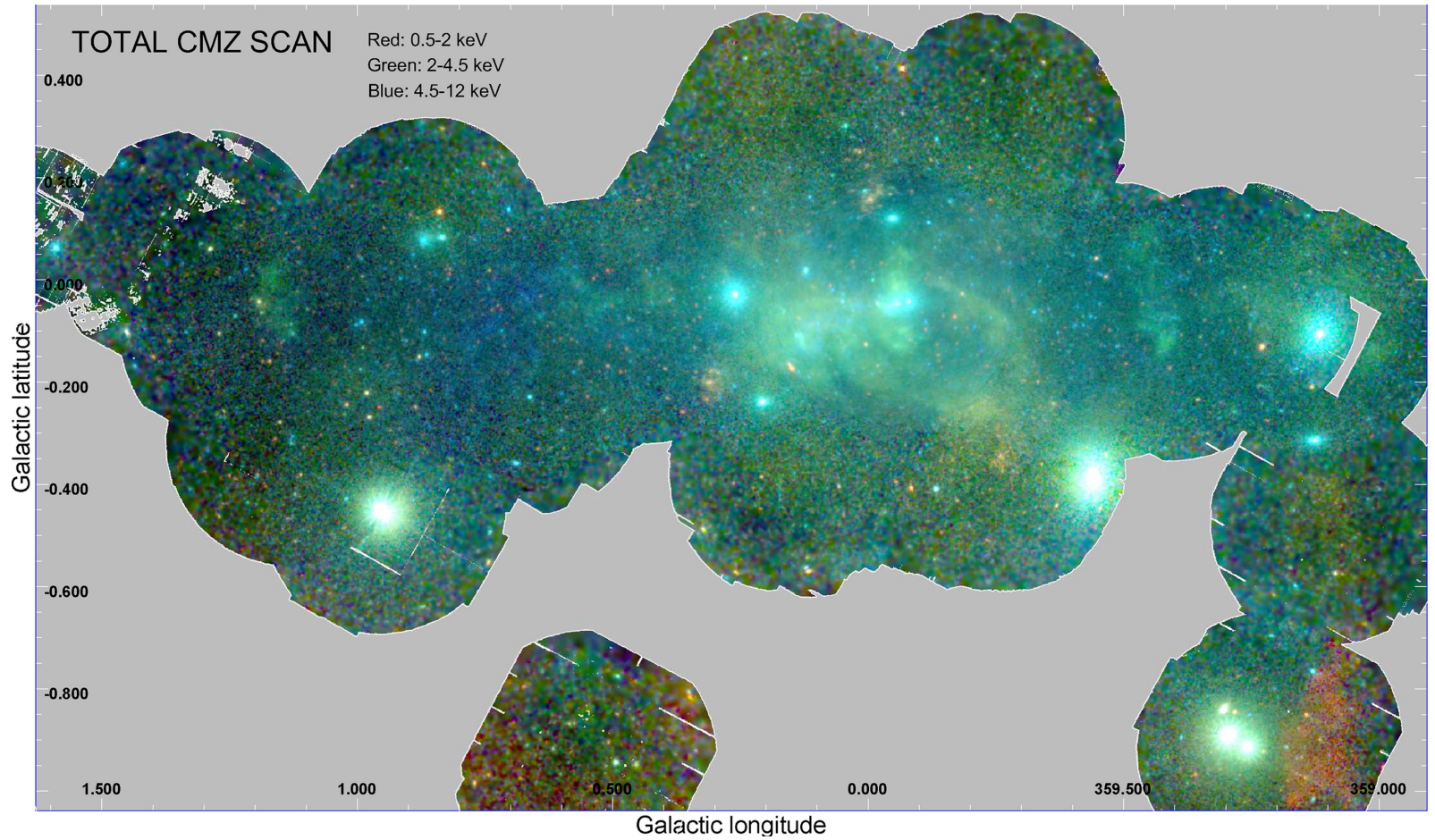

Figure 3. Standard broad energy band (see Table 1 and Fig. 2) RGB mosaic image of all *XMM–Newton* observations within 1° of Sgr A⋆ (see Table A1). This represents the deepest X-ray view of the CMZ region with exposure higher than 0.2 Ms along the Galactic disc and 1.5 Ms in the centre (see Fig. 1). X-ray emission from X-ray binaries, star clusters, SNRs, bubbles and superbubbles, H II regions, PWNs, non-thermal filaments, nearby X-ray active stars, the supermassive BH Sgr A⋆ and many other features are observed (see Figs 5 and 6). The detector background has been subtracted and adaptive smoothing applied. Residual features and holes generated by correction of the stray light from GX 3+1 are visible (see also Fig. 1) at Galactic latitudes between $l \sim 1.^{\circ}2$ and $l \sim 1.^{\circ}4$ and latitudes $b \sim -0.^{\circ}2$ and $b \sim 0.^{\circ}4$.

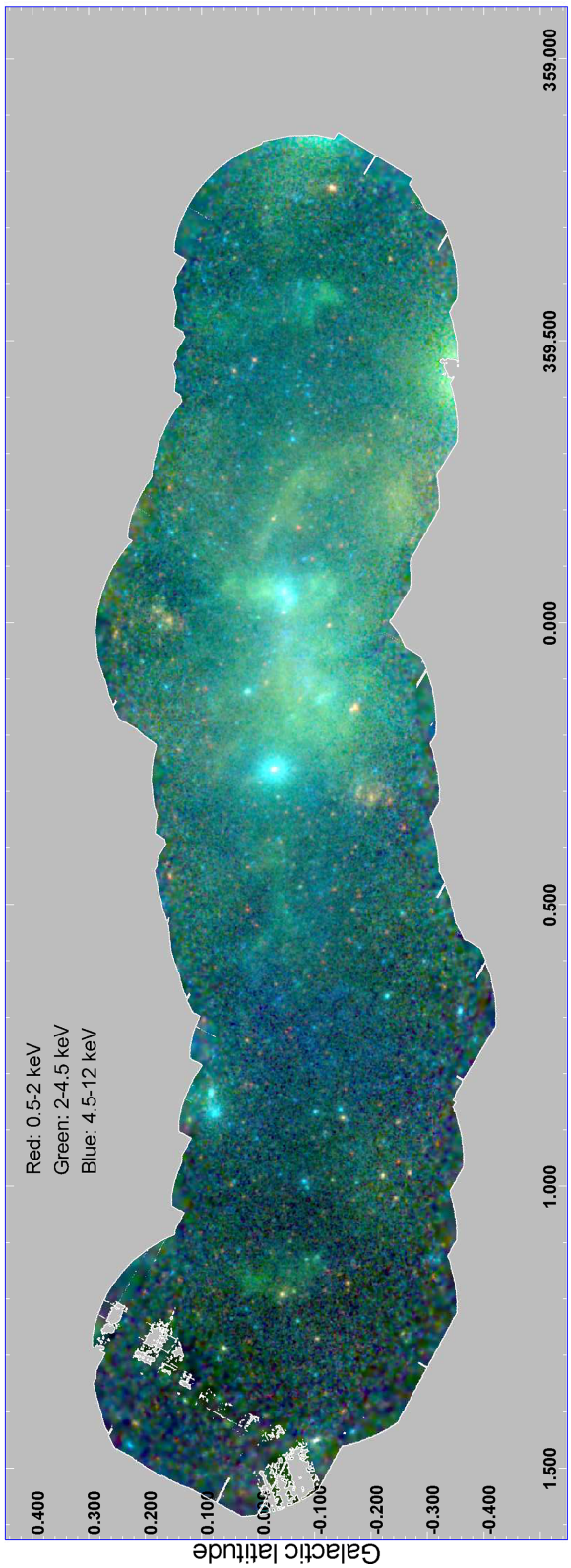

Figure 4. Standard broad energy band RGB image of the *XMM–Newton* CMZ scan performed in 2012. The CMZ is observed with a uniform exposure (see Fig. 1).

energy band image (i.e. the sum of the three energy bands composing the RGB image), as well as the standard minimum and maximum size of the smoothing Gaussian kernel of 10 arcsec (full width at half-maximum) and 200 arcsec, respectively. The signal-to-noise ratio at each pixel is defined as the value at that pixel divided by its standard deviation and the adaptive smoothing that we applied is making the signal-to-noise ratio as close as possible to 6, therefore fainter or less exposed areas are more smoothed than brighter or better exposed regions. For the narrower-band soft-line images (see Figs 10–13), we use the S XV map as a template, requiring a minimum signal-to-noise ratio of 4 and the same standard minimum and maximum of the smoothing kernel. The same smoothing kernel is then applied to all the other bands of the RGB images.

2.2.3 *Internal particle background subtraction*

Unless otherwise specified, internal particle background has been removed from each broad-band image. Following Haberl et al. (2012) we first create, for each selected energy band, both the *total emission* and the *filter wheel closed* images. We then re-normalize and subtract the *filter wheel closed* images from the *total emission* images. The *filter wheel closed* image re-normalization factor is computed by equating, for each instrument, the number of photons in the unexposed corners of the detector to that in the *filter wheel closed* images (see Haberl et al. 2012 for more details). This procedure is reliable and accurate for reasonably long exposures ($t \simeq 5$–10 ks). For this reason data sets with total clean EPIC-pn exposure shorter than 5 ks have not been considered in this analysis.

2.2.4 *Continuum subtraction*

To subtract the continuum emission from an emission-line image, we define a narrow band (B) containing the line, typically sandwiched by two nearby but generally wider energy bands (A and C) that are dominated by continuum emission. Under the assumptions that the emission in the A and C bands is dominated by the continuum and that the continuum emission can be described by a simple power-law, we could in principle determine the intensity of the continuum for each pixel of the band B image. Indeed, using the fluxes in A and C bands, it is possible to derive the continuum parameters (spectral index Γ and intensity). However, this requires the solution of non-linear equations. Therefore, we prefer to implement a different technique based on interpolation. Using XSPEC we simulate, for power-law spectral indices going from $\Gamma = 0.3$ to 3.6, the ratio between the observed flux (e.g. number of photons measured) in the continuum in bands A and C, compared to the simulated continuum flux in band B (e.g. $N_B/(2 \times N_A)$ and $N_B/(2 \times N_C)$). We record these ratios and then plot them as a function of the hardness ratios $(N_C - N_A)/(N_C + N_A)$), which is a proxy for the spectral index Γ. We then find the best-fitting linear relationship between these values, thus determining Con_{AB} and Lin_{AB} that are then allowing us to measure the continuum emission underlying the line emission in band B (N_B) from the intensity in band A (N_A) and the hardness ratio ($N_B = 2 \times N_A \times [\mathrm{Con}_{AB} + \mathrm{Lin}_{AB} \times (N_C - N_A)/(N_C + N_A)]$. To reduce the uncertainties, we perform the same procedure for band C, determining Con_{CB} and Lin_{CB}. We then average these values obtaining, for each pixel: $N_B = N_A \times [\mathrm{Con}_{AB} + \mathrm{Lin}_{AB} \times (N_C - N_A)/(N_C + N_A)] + N_C \times [\mathrm{Con}_{CB} + \mathrm{Lin}_{CB} \times (N_C - N_A)/(N_C + N_A)]$. We finally subtract this continuum emission image from the total emission image B to determine the line intensity map.

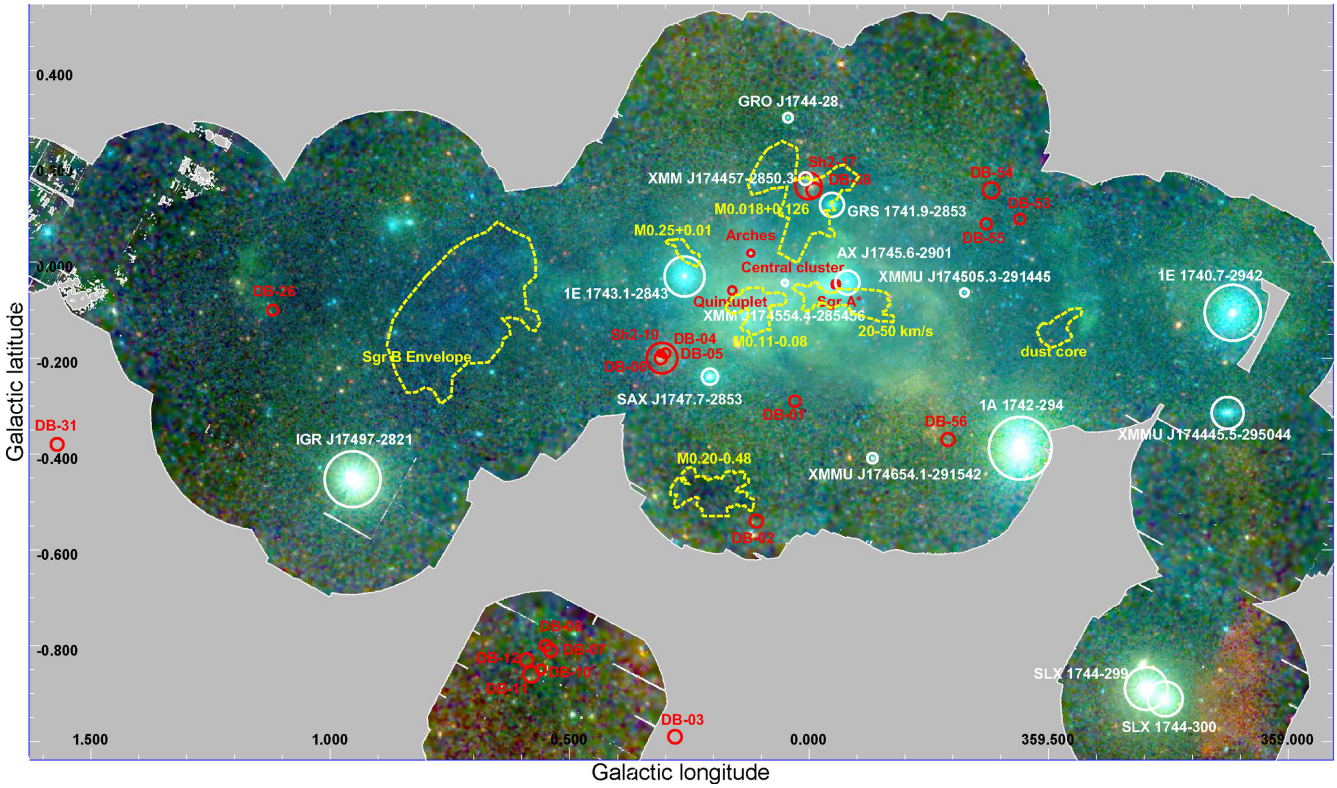

Figure 5. Finding chart. The brightest X-ray point sources (all X-ray binaries) are labelled in white (see Table 2). In red the positions of some star clusters are reported, which are placed either in the GC or along the spiral arms of the Galaxy (see Table 3). With yellow dashed lines the location of some molecular complexes are shown.

3 THE *XMM–NEWTON* BROAD-BAND VIEW OF THE GC

Fig. 3 shows the broad energy band mosaic image of all existing *XMM–Newton* observations within 1° from Sgr A*. Fig. 4 shows the GC image obtained only with data from the 2012 *XMM–Newton* campaign. At the GC distance of 8 kpc, 1 arcmin corresponds to 2.3 pc, 10 pc subtends ∼4.3 arcmin and ∼0.2 corresponds to 28 pc. In red, green and blue, the soft (0.5–2 keV), medium (2–4.5 keV) and hard (4.5–12 keV) continuum bands are shown, respectively. Hundreds of point sources and strong diffuse emission are clearly observed in the map. These point sources are characterized by a wide variety of colours, ranging from distinctive red to dark blue.

3.1 Bright and transient GC point sources during the new (2012) *XMM–Newton* CMZ scan

Many X-ray point sources are clearly visible in Figs 3 and 4. A detailed catalogue of the properties of all the detected point sources is beyond the scope of this paper. Here we briefly describe the brightest GC sources detected by *XMM–Newton* and the X-ray transients in the field of the 2012 scan (see Degenaar et al. 2012 for a compendium of previously noted transients).

The brightest GC point source of the 2012 *XMM–Newton* CMZ scan is 1E 1743.1−2843 (Porquet et al. 2003; Del Santo et al. 2006) a persistently accreting neutron star binary detected at an observed flux level of $F_{2-10\,\mathrm{keV}} \sim 1.1 \times 10^{-10}$ erg cm^{-2} s^{-1} (implying an unabsorbed flux of $F_{2\text{-}10\,\mathrm{keV,\,unab}} \sim 2.6 \times 10^{-10}$ erg cm^{-2} s^{-1}; $N_{\mathrm{H}} \sim 2 \times 10^{23}$ cm^{-2}; obsid: 0694641201). During the 2012 *XMM–Newton* campaign we also detected an outburst from a new, very faint X-ray transient that we name XMMU J174505.3−291445. The source has a typical quiescent luminosity at or below $L_{\mathrm{X}} \sim 10^{33}$ erg s^{-1}, but on 2012 August 31 (during obsid 0694640201) it was observed to go into outburst for about ∼2 h and to reach a peak X-ray luminosity of $L_{\mathrm{X}} \sim 10^{35}$ erg s^{-1}. The detailed spectral and multiwavelength analysis of this new transient will be presented in a separate paper (Soldi et al. in preparation; but see also Soldi et al. 2014).

Another faint X-ray transient, XMM J174457−2850.3, is detected in two 2012 observations: obsid: 0694641101–0694640301. The observed 2–10 keV flux is 1.1 ± 0.3 and $2.9 \pm 0.6 \times 10^{-13}$ erg cm^{-2} s^{-1}, respectively. A power-law fit to the spectrum with the photon index fixed to the value reported by Sakano et al. (2005) yields a column density of $N_{\mathrm{H}} = (1.4 \pm 0.4) \times 10^{23}$ cm^{-2}. This source was discovered in 2001 by Sakano et al. (2005) who reported a tentative detection of an X-ray pulsation of ∼5 s, during the ∼25 ks *XMM–Newton* observation. Both a visual inspection and timing analysis of the X-ray light curve show no evidence for bursts and/or dips. However, even considering the four times longer exposure of the new data, we cannot exclude or confirm the ∼5 s periodic modulation because of the lower flux observed. In fact, during the 2001 *XMM–Newton* observation (obsid: 0112972101) XMM J174457−2850.3 had a flux about 10–40 times higher (∼45×10^{-13} erg cm^{-2} s^{-1}) than in 2012 (in quiescence XMM J174457−2850.3 has a typical 2–10 keV flux lower than 0.2×10^{-13} erg cm^{-2} s^{-1}).

Only upper limits are measured for the other well-known X-ray transients within the field of view. The two bursters GRS 1741.9−2853 and AX J1745.6−2901 (Sakano et al. 2002; Trap et al. 2009; Ponti et al. 2014, 2015) have flux limits of $F_{2-10\,\mathrm{keV}} < 2 \times 10^{-14}$ erg cm^{-2} s^{-1} and $F_{2-10\,\mathrm{keV}} < 10^{-13}$ erg

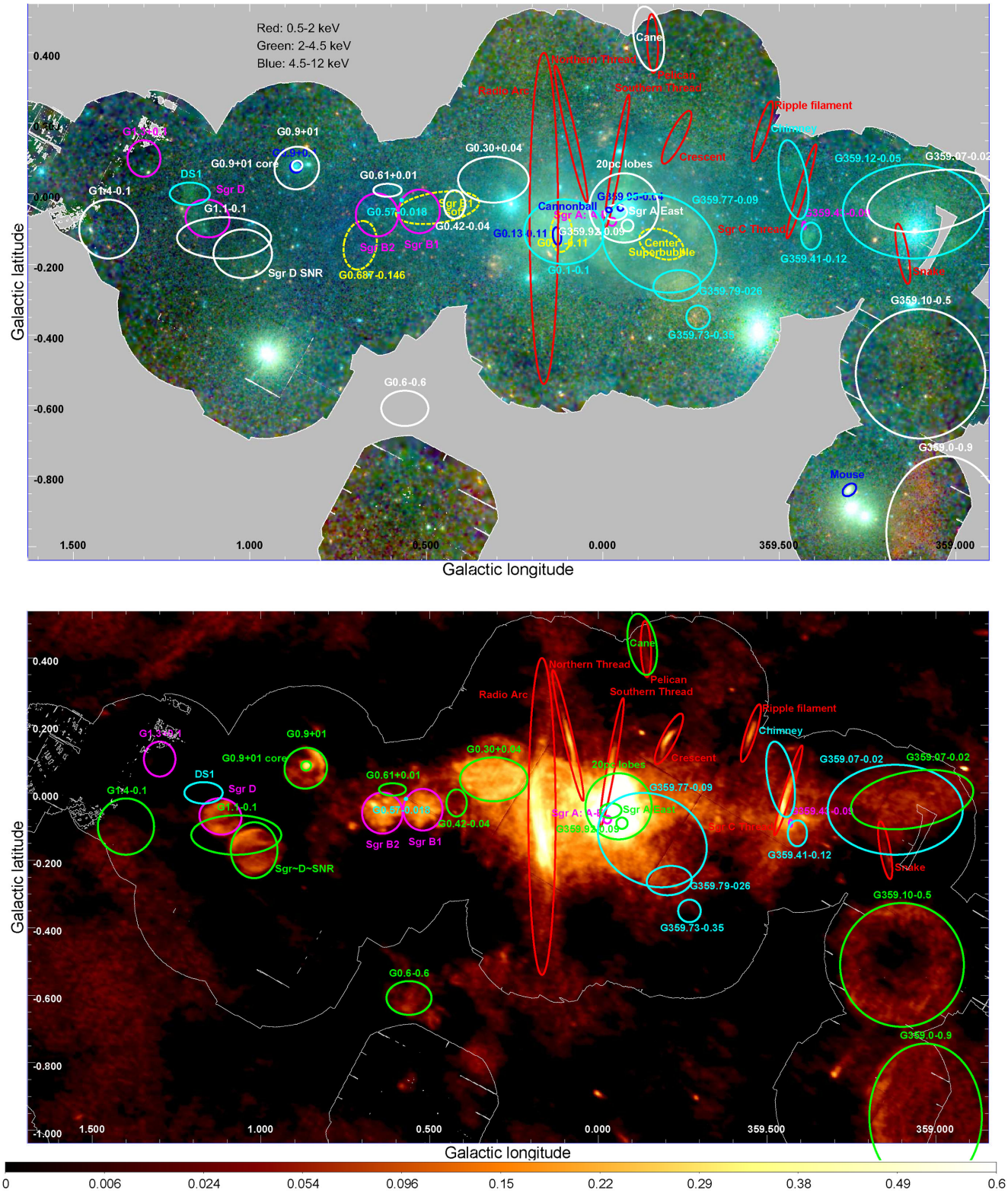

Figure 6. Finding charts. Top panel broad-band X-ray continuum image. White ellipses show the position and size of known, radio-detected SNRs. Cyan ellipses indicate the position and size of bright diffuse X-ray emission possibly associated with SNRs that lack a clear radio counterpart (or such in the case of G359.12−0.05 that show X-ray emission significantly displaced from the radio emission associated with the radio remnant G359.07−0.02). The magenta ellipses show the location and dimension of some bright H II regions, while the red ellipses indicate some of the largest non-thermal filaments detected in radio (see Table 4). Blue ellipses show some PWN and the yellow dashed ellipses show the regions used to accumulate the spectra shown in Fig. 2. Bottom panel: 90-cm radio image of the CMZ region obtained with the VLA (courtesy of LaRosa et al. 2000). For display purposes the radio SNRs are shown with green ellipses. The other regions have the same colour code as the top panel. The image shows the radio flux (Jy beam^{-1} unit).

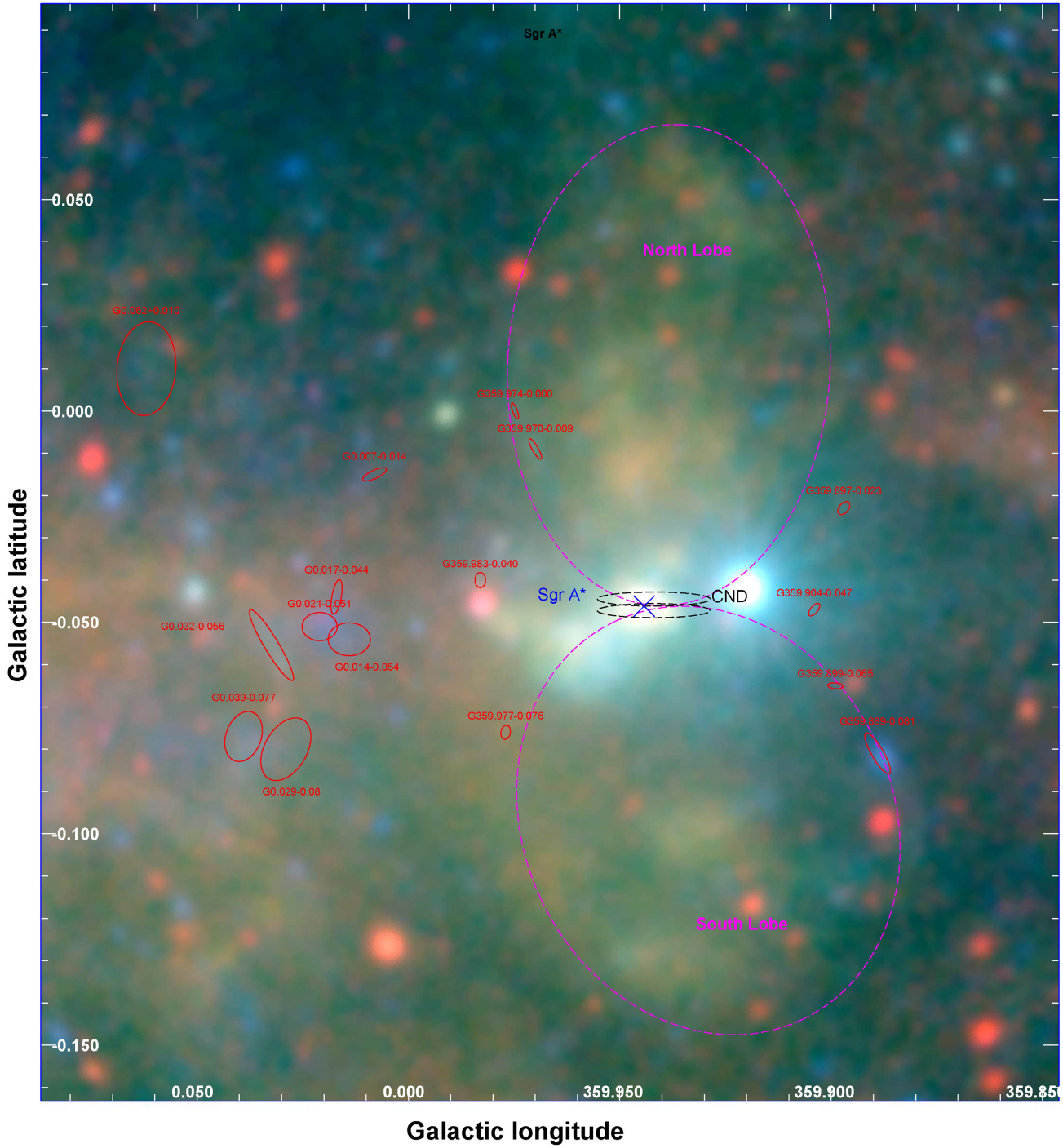

Figure 7. Finding chart. Zoom of the central ∼10 arcmin of the Milky Way as seen by *XMM–Newton* (same energy bands and colour scheme as in Fig. 3). The position of Sgr A* is indicated by the blue cross. The red ellipses show the position and extent of filamentary and diffuse X-ray emission features associated with, e.g. non-thermal filaments (Table 4). The magenta dashed ellipses show the location and extension of the 20 pc bipolar X-ray lobes. The black dashed ellipses indicate the position and orientation of the CND.

cm^{-2} s^{-1} (obsid: 0694641101, 0694640301), respectively. Closer to Sgr A*, we find an upper limit on the 2–10 keV flux of $F_{2-10\,\mathrm{keV}} < 5 \times 10^{-12}$ erg cm^{-2} s^{-1} towards three other sources: CXOGC J174540.0−290031, the low-mass X-ray binary showing X-ray eclipses (Muno et al. 2005b; Porquet et al. 2005b), CXOGC J174540.0−290005 (Koch et al. 2014) and the magnetar discovered on 2013 April 25 (Degenaar et al. 2013; Dwelly & Ponti 2013; Mori et al. 2013; Rea et al. 2013; Kaspi et al. 2014; Coti-Zelati et al. 2015), located at distances from Sgr A* of only ∼2.9, ∼23 and ∼2.4 arcsec, respectively.

Finally, we observe that both XMMU J174554.4−285456, the faint transient with a possible pulsation period of about 172 s (Porquet et al. 2005b) and SAX J1747.7−2853, the bursting (showing also superbursts) X-ray transient (Wijnands, Miller & Wang

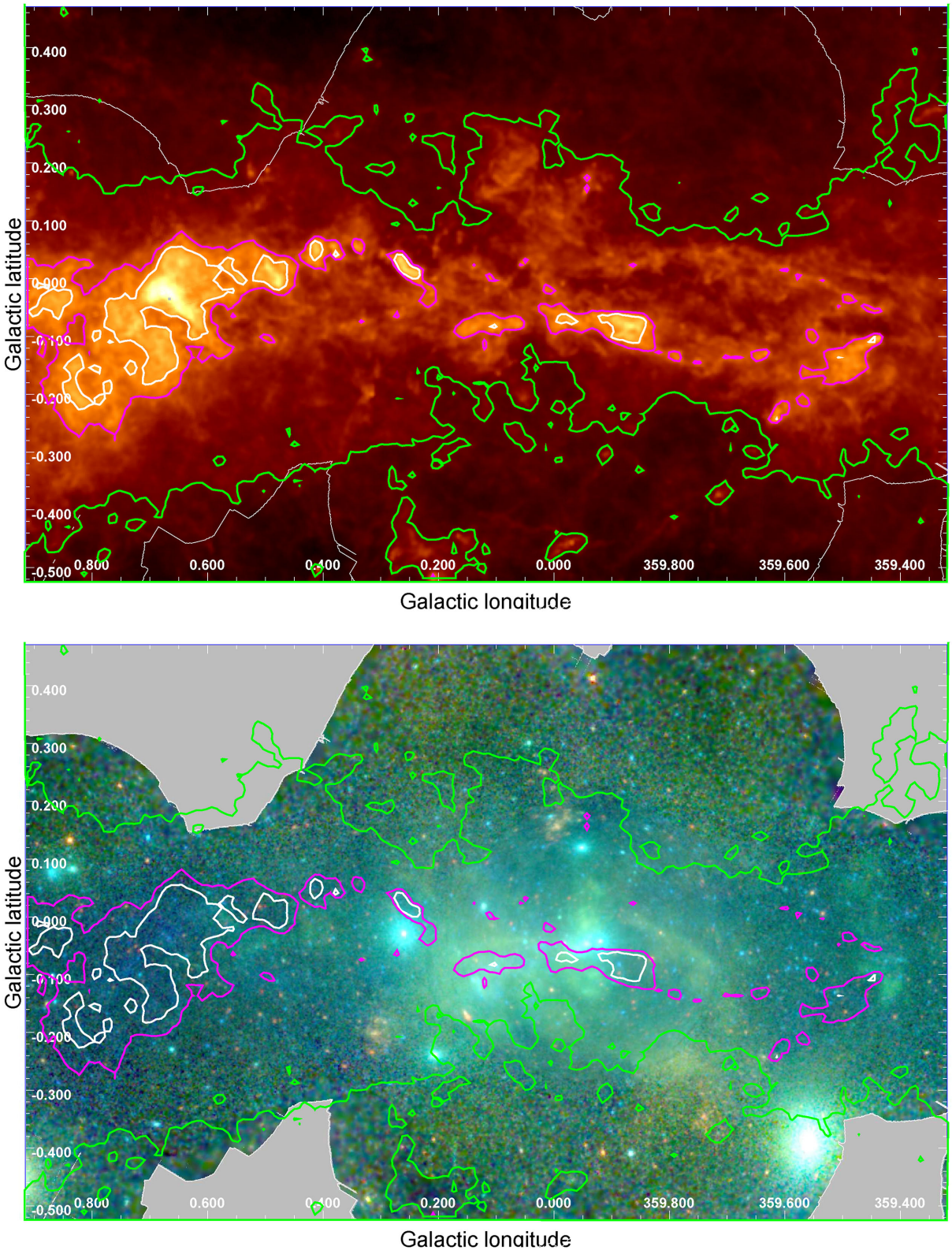

Figure 8. Top panel: neutral hydrogen column density distribution as derived from dust emission (Molinari et al. 2011). The image shows the $N_{\rm H}$ distribution in logarithmic scale from $N_{\rm H} = 4.5 \times 10^{22}$ up to 3.8×10^{25} cm^{-2}. The green, magenta and white contour levels correspond to $N_{\rm H} = 1.5 \times 10^{23}$, 7×10^{23} and 1.5×10^{24} cm^{-2}, respectively. Bottom panel: X-ray continuum RGB map (Fig. 3) with the column density contours overlaid.

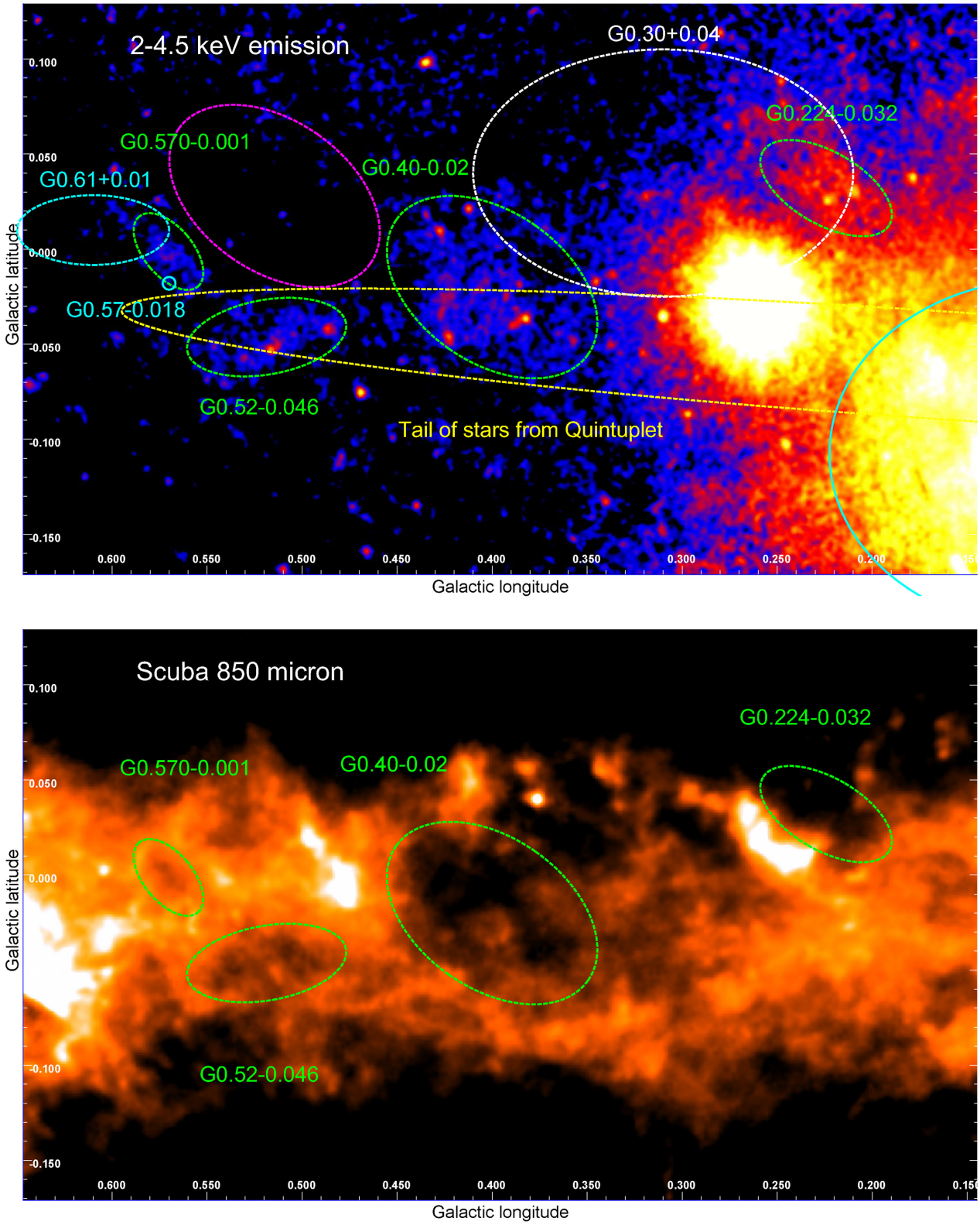

Figure 9. Top panel: 2–4.5 keV map. The dashed white ellipse shows the location of the radio SNR G0.30+0.04. The dashed and solid cyan ellipses show the positions of known X-ray SNRs and superbubbles, respectively. The green dashed ellipses indicate enhancements of soft X-ray-emitting gas (G0.40−0.02 was already observed in X-rays by Nobukawa et al. 2008), the magenta ellipse is used in the spectral analysis as a background region (Back in Table 7). The dashed yellow ellipse shows the location of the massive stars that could be in the tidal tail of the Quintuplet cluster (Habibi et al. 2013, 2014). Bottom panel: 850 μm map of the GC obtained with the SCUBA bolometer (Pierce-Price et al. 2000). The four green-dashed ellipses, selected because they show enhanced X-ray emission, correspond to holes in the 2 mm gas distribution.

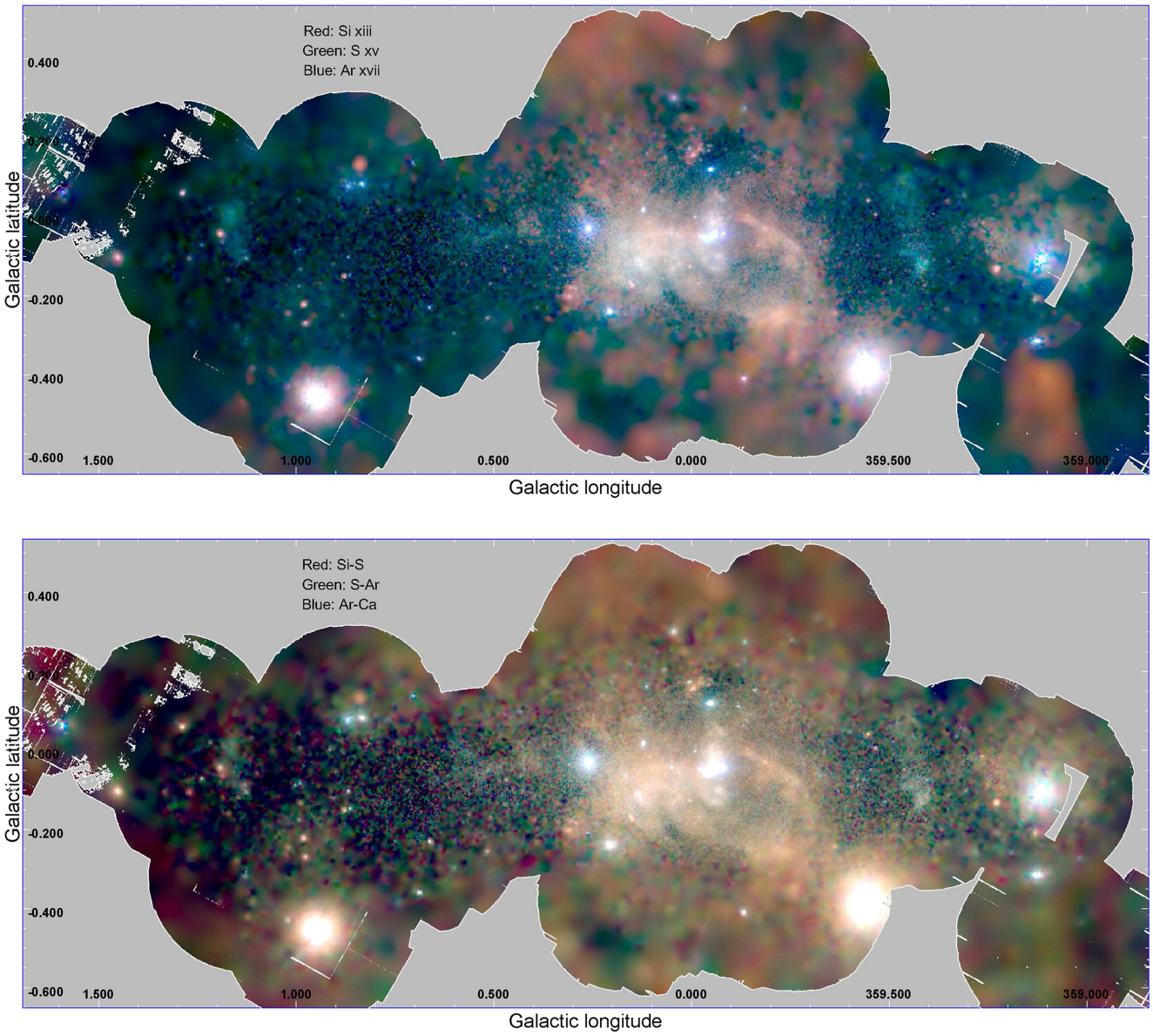

Figure 10. Top panel: soft lines (continuum unsubtracted) RGB image of the CMZ. The Si XIII line emission is shown in red, S XV in green and Ar XVII+ Ca XIX in blue. Bottom panel: RGB image of the energy bands between soft emission lines. The Si–S band emission is shown in red (see Table 1 for a definition of the energy bands), S–Ar in green and Ar–Ca + Blue–Ca in blue. The diffuse emission in this interline continuum is very similar to the soft emission line one, suggesting that the same process is producing both the lines and the majority of the soft X-ray continuum. The colour variations within the map are modulated primarily by abundance variations (top), temperature of the emitting plasma, continuum shape and absorption.

2002; Natalucci et al. 2004; Werner et al. 2004), have flux limits of $F_{2-10\,\mathrm{keV}} < 2 \times 10^{-13}$ erg cm^{-2} s^{-1}.

3.1.1 *Bright sources outside the 2012 scan*

Three very bright sources are outside the field of view during the 2012 CMZ scan; however, they imprint their presence through bright stray-light arcs. The arc features between and south of the Sgr A and C complexes ($l \sim 359.^{\circ}6$–$359.^{\circ}9$, $b \sim -0.^{\circ}15$–$0.^{\circ}4$) testify that the bright X-ray burster 1A 1742-294 (Bélanger et al. 2006; Kuulkers et al. 2007) was active during the 2012 *XMM–Newton* campaign. The very bright arcs east of the Sgr D complex (obsid: 0694641601) are most probably produced by the very bright neutron star low-mass X-ray binary GX 3+1 (Piraino et al. 2012) located about $1.^{\circ}18$ north-east of the arcs.[3] On the far west edge of the 2012 scan a brightening is observed. This is due to 1E 1740.7−2942 (Reynolds & Miller 2010; Castro et al. 2013; Natalucci et al. 2014), a bright and persistent accreting microquasar, at only ∼1.5 arcmin from the edge of the 2012 field of view (see Fig. 3). The lack of stray light south of the Sgr B region suggests that the BH candidate IGR J17497−2821 (Soldi et al. 2006; Paizis et al. 2009) was in quiescence during these observations. Two bright X-ray bursters have been active during the 2003 *XMM–Newton* observation pointed to the pulsar wind nebula

[3] This region is covered only by the observations of the 2012 *XMM–Newton* scan, therefore the removal of the stray-light arcs generates regions with null exposures in the final mosaic maps (e.g. Figs 3 and 4).

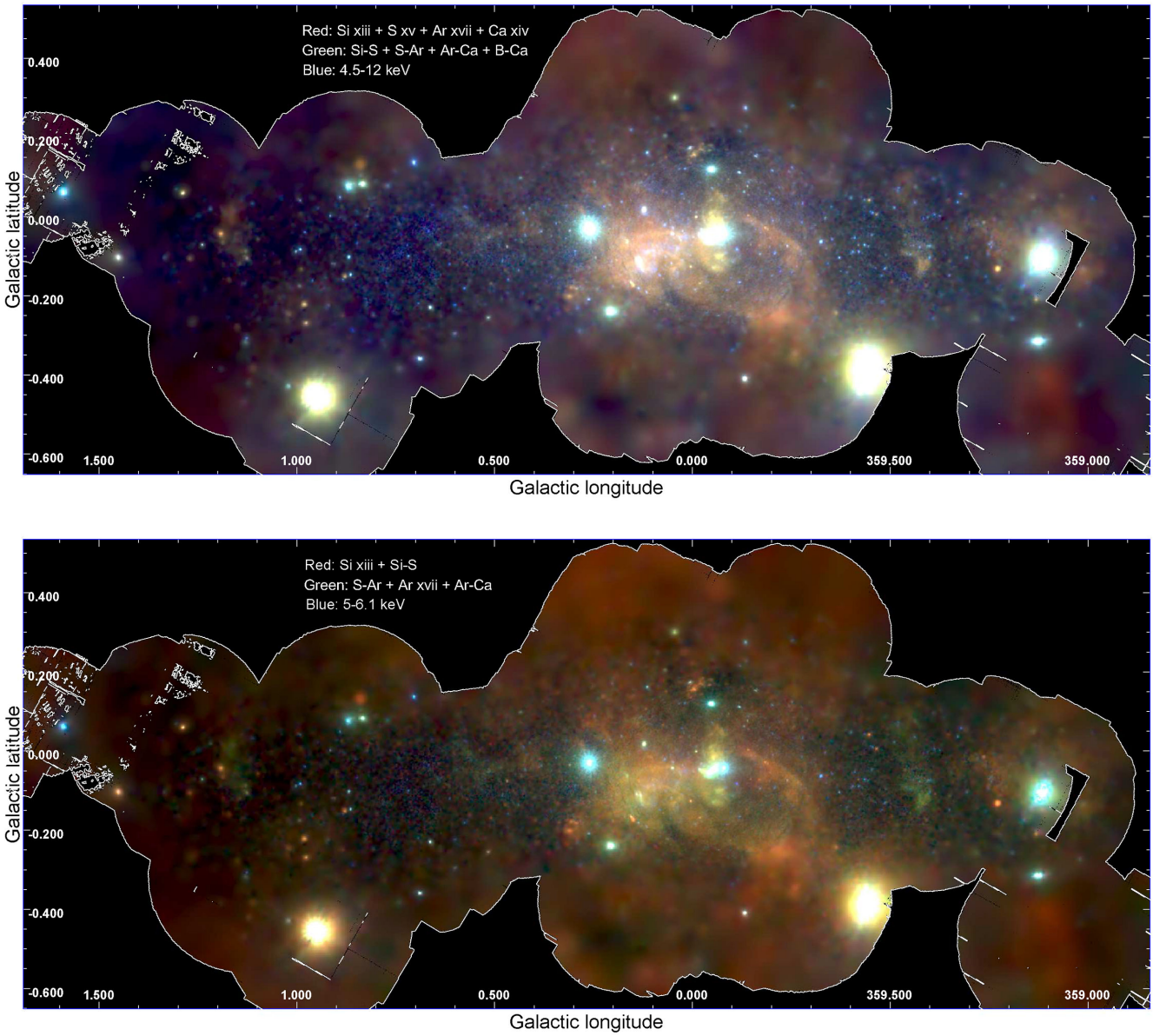

Figure 11. Top panel: RGB image composed of summed, continuum-subtracted line emission (Si XIII + S XV + Ar XVII + Ca XIX) in red, the sum of the interline continua (Si–S + S–Ar + Ar–Ca + Blue–Ca) in green and the CFe K emission in blue (see Table 1). Bottom panel: RGB image, in red the Si XIII + Si–S emission, in green the S–Ar + S XV + Ar–Ca and in blue the CFe K emission.

called The Mouse, i.e. SLX 1744−299 and SLX 1744−300 (Mori et al. 2005).

3.2 Very soft emission: foreground emission

Despite the presence of distinctively soft (red) point sources, Fig. 3 shows no strong, diffuse, very soft X-ray emission. This is mainly due to the very high column density of neutral hydrogen towards the GC (with typical values in the range $N_{\rm H} \sim 3$–9×10^{22} cm^{-2}; see also Section 7). Almost no GC X-ray radiation reaches us below $E \lesssim 1.3$, 1.7 or 2.3 keV for column density values of $N_{\rm H} \simeq 3$, 5, or 9×10^{22} cm^{-2}, respectively (see Fig. 2). The majority of the 'red' sources present in the 0.5–1.5 keV band are point-like and are associated with foreground active stars characterized by an unabsorbed soft X-ray spectrum.

Two clearly extended and soft X-ray-emitting sources are present in Fig. 3. These correspond to Sh2−10 and Sh2−17 (Wang et al. 2002; Dutra et al. 2003; Law & Yusef-Zadeh 2004; Fukuoka et al. 2009), two stellar clusters located in one of the Milky Way spiral arms and thus characterized by a lower column density of absorbing material, consequently appearing stronger in the 1–2.5 keV range (visible in Fig. 3 with orange colours).

3.3 Soft and hard GC emission

GC radiation with energies above ∼2–3 keV can typically reach us and be detected (in green and blue in Fig. 3). GC sources with a significant continuum component (e.g. power-law or bremsstrahlung), such as observed from most GC point sources, the GC stellar clusters (e.g. the Arches, the Quintuplet and the Central cluster) as well

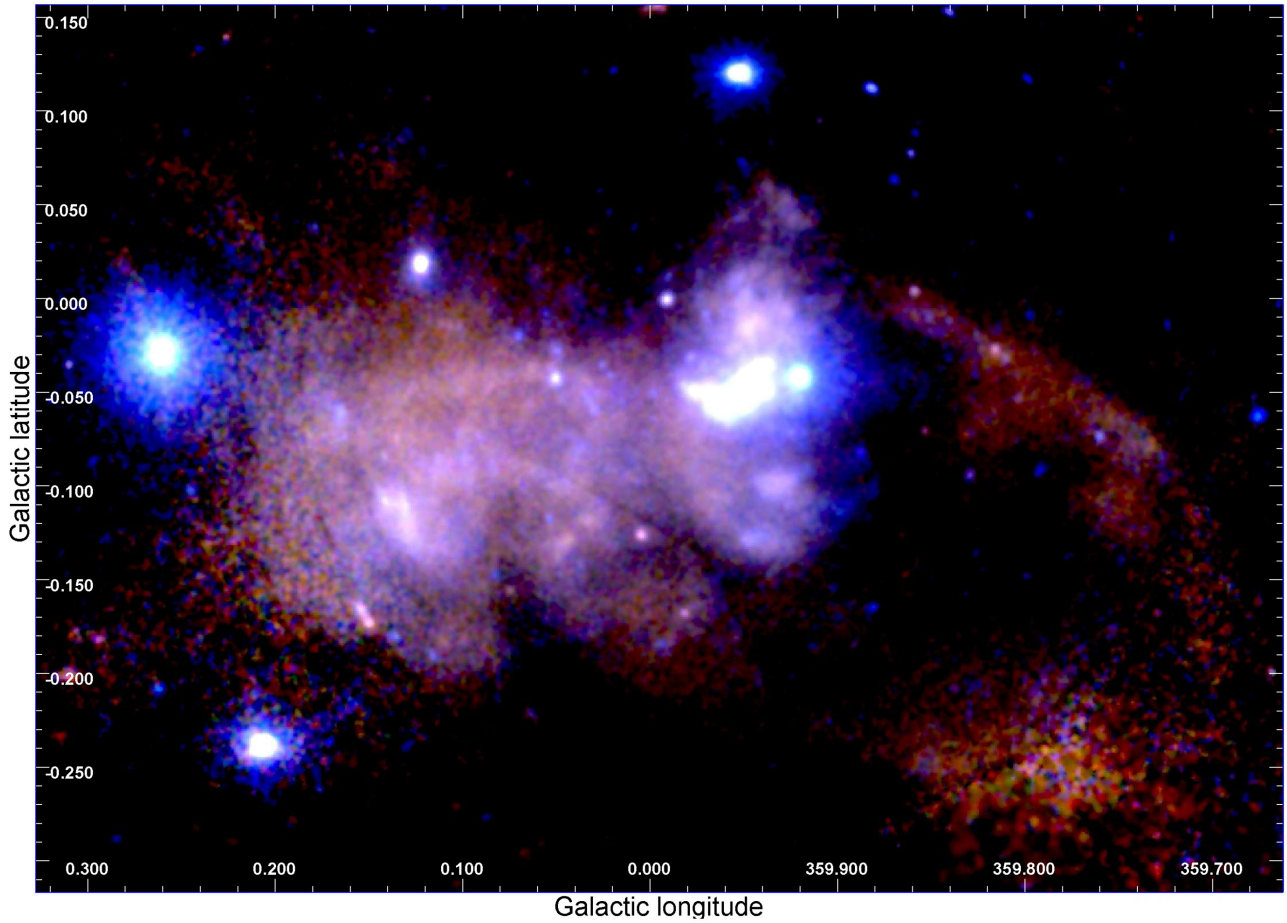

Figure 12. RGB image with colour scale chosen to highlight enhancements and depressions in the diffuse emission east of Sgr A*. In red the sum of the Si–S and S XV bands is shown. In green the sum of S–Ar plus the S XV and Ar XVII bands is shown. The blue image shows the sum of the Ar–Ca plus Blue–Ca and Ca XIX bands (see Table 1 for the definition of the energy bands).

as some SNRs (such as SNR G0.9+0.1 and Sgr A East) appear with a bright light blue colour.

Colour gradients confirm the presence of at least two components of the diffuse emission, each having a different spatial distribution (see Figs 3 and 4). One component dominates the emission in the soft and medium energy bands, thus appearing with a distinctively green colour. Its distribution appears to be very patchy, peaking typically at the position of known SNRs. Another, harder component appears with a dark blue colour (Fig. 3). This harder emission is known to consist of at least two separate contributions. One, which is associated with intense high-ionization Fe K lines, is smoothly distributed and peaks right at the GC; it is likely produced by faint point sources (Muno et al. 2004; Revnivtsev et al. 2009; Heard & Warwick 2013a). The other, which is associated with neutral Fe K emission lines, has a patchy distribution peaking at the position of molecular cloud complexes; it is likely due to an ensemble of X-ray reflection nebulae (see Ponti et al. 2013 for a review). We also note that the Galactic plane emission is dominated by dark blue colours (Fig. 3), while regions located at $b \gtrsim 0.^{\circ}2$ and $b \lesssim -0.^{\circ}35$ have a significantly greener colour. We address this in more detail in Sections 5, 7 and 8.7.

4 SOFT LINE EMISSION

Fig. 2 shows the spectra of the diffuse emission from the regions marked in magenta in Fig. 6. The ∼1.5–5 keV band shows strong, narrow emission lines, the strongest of which are Si XIII, S XV, Ar XVII and Ca XIX. This line emission, as well as the underlying continuum and the intraline emission, are typically well fitted by a thermal model (e.g. APEC in XSPEC) with temperatures in the range 0.6–1.5 keV (Kaneda et al. 1997; Tanaka et al. 2000; Muno et al. 2004; Nobukawa et al. 2010; Heard & Warwick 2013b). At higher energies a power-law component with intense Fe XXV and Fe XXVI lines is also observed over the entire GC region. Additionally, neutral Fe K α and K β lines are also observed. The neutral Fe K emission lines are associated with different processes, therefore they will be the focus of separate publications.

4.1 RGB images of soft emission lines

The top and bottom panels of Fig. 10 show the line (continuum non-subtracted) RGB image and the interline continuum RGB image (see the caption of Fig. 10 and Table 1 for more details). We note that the soft X-ray line image shows very strong colour gradients (less dramatic colour variations are observed in the continuum image). In particular, the sources DS1 (the core of Sgr D), the western part of Sgr B1 (i.e. G0.52−0.046, G0.570−0.001), Sgr C, as well as the Chimney above it, all have a distinctively green–blue colour, while G359.12−0.05, G359.10−0.5, G359.79−0.26, G359.73−0.35 and the entire G359.77−0.09 superbubble are characterized by orange–brown colours. G0.1−0.1, the Radio Arc, the arched filaments (see fig. of Lang, Goss & Morris 2002), G0.224−0.032, and G0.40−0.02

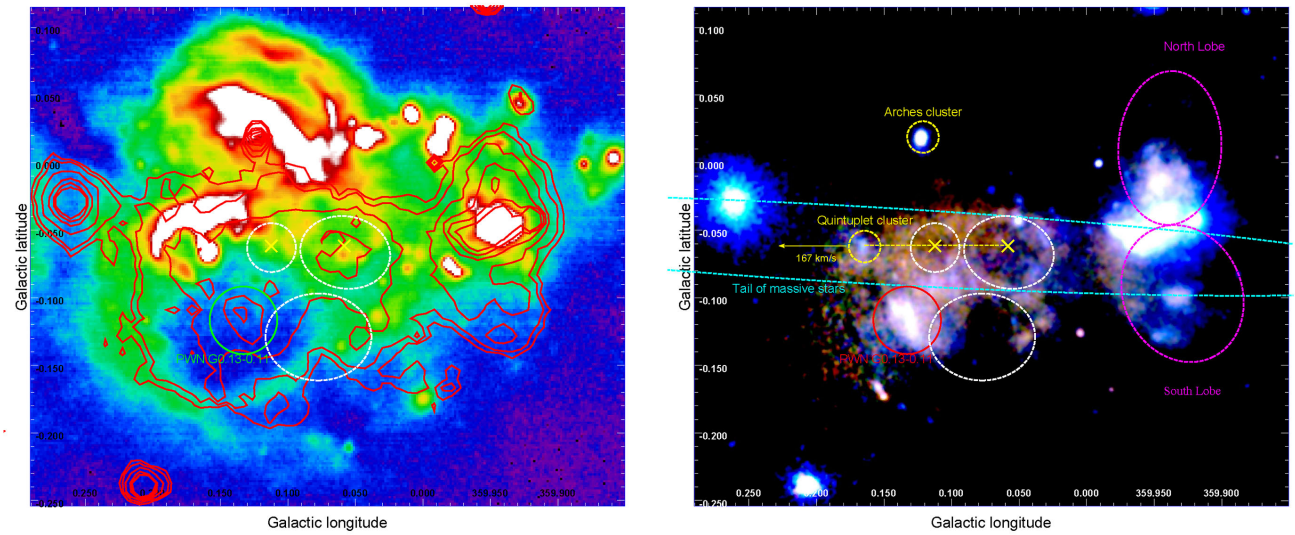

Figure 13. Left-hand panel: 20 μm MSX map of the GC. The contours indicate the intensity of S XV emission. Soft X-ray emission fills the arc bubble observed in the mid-IR. The green solid circle and the white dashed ellipses indicate the position of the PWN G0.13−0.11 and three structures in the soft X-ray emission map (see the right-hand panel). Right-hand panel: soft X-ray map of the GC (the same energy bands used in Fig. 12 are displayed). The position of the PWN G0.13−0.11 is indicated by a red circle with 1.5 arcmin radius. At least three sub-structures, appearing like holes, are observed within G0.1−0.1 (here indicated with white dashed ellipses). The positions of the Arches and Quintuplet star clusters are indicated by yellow dashed circles. The direction of the supersonic motion of the Quintuplet cluster is indicated and its past location is indicated by the yellow dashed line. The inferred positions of the Quintuplet 4×10^4 and 9×10^4 years ago are indicated with yellow crosses. The cyan dashed ellipse indicates the region in which many massive stars that might have been expelled by the Quintuplet cluster are located.

are also characterized by red–brown colours; however, here a gradation of white and green is also present (please refer to Tables 3 and 4 and Figs 5 and 6 for the positions of the regions listed here). The lobes of Sgr A appear with a whiter colour than the surroundings. In addition, we observe bright red–brown emission along two broad, linear ridges having relatively sharp edges to the north-west and north-east of Sgr A*. This latter feature is discussed in detail in Section 8.4.

In spite of the fact that these images show different components (one being dominated by emission lines, the other by continuum emission), they are remarkably similar. No clear diffuse emission component is present in one and absent from the other image. This indicates that most of the diffuse soft X-ray continuum and line emission are, indeed, produced by the same process. In addition, the differences in the ratio between photons emitted in the lines and in the continuum can add valuable information for understanding the radiative mechanism. In fact, such differences could be due, for example, to different cosmic abundances and/or variations in the relative contributions of various thermal and non-thermal radiation mechanisms. In order to better highlight these differences, we map the sum of the interline continua in the same image (see the caption of Fig. 11 and Table 1). As expected, none of the point sources is a strong soft line emitter (they in fact appear brighter in the interline image). We also note that the intense soft X-ray-emitting regions in the Galactic plane, such as Sgr D, Sgr B1, Sgr C, the Chimney and G359.9−0.125 are characterized by distinctively orange–red colours, indicating they are strong line emitters.

For an alternative perspective, the bottom panel of Fig. 11 shows the Si XIII + Si–S bands in red, S–Ar + S XV + Ar–Ca in green, and CFe K in blue. These energy bands are chosen to highlight any energy dependence in the soft X-ray emission that could be due to column density variations of the obscuring matter or temperature fluctuations of the emitting gas. In fact, the softer energy bands (Si XIII + Si–S) will be more affected by absorption or low-temperature plasma emission compared to the medium (S–Ar + S XV + Ar–Ca) or high-energy bands. We defer the detailed discussion of the features present in these images to the discussion of the various physical components presented in Section 8 and subsections.

4.2 Continuum-subtracted soft emission line maps and profiles

From top to bottom, the panels of Fig. 14 show the continuum-subtracted Si XIII, S XV, Ar XVII, Ca XIX intensity maps. Although the continuum subtraction procedure should naturally remove the emission from the line-free point sources, small fluctuations in the continuum subtraction, in the case of the brightest sources, sometimes leave significant residuals. For this reason, we have masked out the brightest point sources in our computation of these maps.

The different curves of Fig. 15 show the continuum-subtracted emission profiles (integrated over latitude from the magenta rectangle in Fig. 14) for the individual soft emission lines. The same four line profiles are compared in Fig. 15 with similar profiles in which the contribution of specific bright structures has been removed.

5 SPECTRAL DECOMPOSITION

In order to better trace the relative contributions of the diffuse thermal (soft and hot) and non-thermal components, we have performed a simple component separation using a list of images depicting various energy bands. We use a total of 17 energy bands: 11 for the continuum[4] and 6 for the lines (tracing Si XIII, S XV, Ar XVII, Ca XIX, Fe K α and Fe XXV, see Table 1). This treatment of the data

[4] The 11 continuum energy bands used are 1.0–1.5 keV; 1.5–1.8 keV; 2.0–2.35 keV; 2.55–3.05 keV; 3.25–3.75 keV; 3.95–4.70 keV; 4.70–5.40 keV; 5.40–6.30 keV; 6.50–6.60 keV; 6.80–7.80 keV and 8.20–9.50 keV.

Table 2. List of bright and transient point sources during the 2012 *XMM–Newton* scan as well as bright point sources observed in all scans of the region (see Fig. 5. To avoid excessive crowding around Sgr A*, CXOCG J174540.0−290005 and SGR J1745−2900 are not shown).

BRIGHT AND TRANSIENT POINT SOURCES			
Source name	Coordinates[a]	Flux[b]	References
Within the 2012 CMZ scan			
1E 1743.1−2843	0.2608,−0.0287	110	90,92,93
XMMU J174505.3−291445	359.6756,−0.0634	14	94
XMMU J174457−2850.3	0.0076,−0.1743	0.3	90,95
GRS 1741.9−2853	359.9528,+0.1202	<0.02	90,59,96
AX J1745.6−2901	359.9203,−0.0420	<0.1	59,90,91,122
CXOGC J174540.0−290031	359.9435,−0.0465	<5	97,98
SGR J1745−2900	359.9441,−0.0468	<5	100,101,102,103
XMM J174445.5–295040	0.0506,−0.0429	<0.2	97
SAX J1747.0–2853	0.2073,−0.2385	<0.2	90,104,105,106
CXOCG J174540.0−290005	359.9497,−0.04269	<5	99
Within the total GC scan			
1E 1740.7−2942	359.1160,−0.1057		110,111,112
1A 1742−294	359.5590,−0.3882		90,107,108
IGR J17497−2821	0.9532,−0.4528		90,113,114
GRO J1744−28	0.0445,+0.3015		90
XMMU J174654.1−291542	359.8675,−0.4086		90
XMMU J174554.4−285456	359.1268,−0.3143		84,85,86
SLX 1744−299	359.2961,−0.8892		37,59,87,88,89
SLX 1744−300	359.2565,−0.9111		37,59,87,88,89

[a]Coordinates are in Galactic format. [b]Fluxes are given in units of 10^{-12} erg cm^{-2} s^{-1} and correspond to the mean flux observed during the 2012 *XMM–Newton* scan of the CMZ.

References: (1) Wang, Dong & Lang (2006b); (2) Yusef-Zadeh et al. (2002); (3) Capelli et al. (2011); (4) Tatischeff, Decourchelle & Maurin (2012); (5) Sakano et al. (2003); (6) Habibi et al. (2013); (7) Habibi, Stolte & Harfst (2014); (8) Krivonos et al. (2014); (9) Clavel et al. (2014); (10) Dutra et al. (2003); (11) Law et al. (2004); (12) Fukuoka et al. (2009); (13) Wang et al. (2002a); (14) Tsuru et al. (2009); (15) Mori et al. (2008); (16) Mori et al. (2009); (17) Heard & Warwick (2013a); (18) Maeda et al. (2002); (19) Park et al. (2005); (20) Koyama et al. (2007b); (21) Kassim & Frail (1996); (22) Nobukawa et al. (2008); (23) Senda, Murakami & Koyama (2002); (24) Renaud et al. (2006); (25) Mereghetti, Sidoli & Israel (1998); (26) Gaensler, Pivovaroff & Garmire (2001); (27) Porquet et al. (2003b); (28) Aharonian et al. (2005); (29) Dubner, Giacani & Decourchelle (2008); (30) Nobukawa et al. (2009); (31) Sawada et al. (2009); (32) Morris et al. (2003); (33) Morris et al. (2004); (34) Markoff (2010); (35) Zhang et al. (2014); (36) Nynka et al. (2014); (37) Gaensler et al. (2004); (38) Pedlar et al. (1989); (39) Cotera et al. (1996); (40) Figer et al. (1999); (41) Johnson et al. (2009); (42) Lu, Yuan & Lou (2008); (43) Lu, Wang & Lang (2003); (44) Yusef-Zadeh et al. (2005); (45) Baganoff et al. (2003); (46) Ho et al. (1985); (47) Bamba et al. (2002); (48) LaRosa et al. (2000); (49) Morris & Yusef-Zadeh (1985); (50) Lang et al. (1999); (51) Anantharamaiah et al. (1991); (52) Yusef-Zadeh & Morris (1987b); (53) Yusef-Zadeh & Morris (1987a); (54) Yusef-Zadeh & Morris (1987c); (55) Muno et al. (2008); (56) Uchida, Morris & Yusef-Zadeh (1992); (57) Predehl & Kulkarni (1995); (58) Senda, Murakami & Koyama (2003); (59) Sakano et al. (2002); (60) Coil & Ho (2000); (61) Murakami (2002); (62) Yusef-Zadeh et al. (2007); (63) Dutra & Bica (2000); (64) Zoglauer et al. (2015); (65) Koyama et al. (2007a); (66) Nakashima et al. (2010); (67) Downes & Maxwell (1966); (68) Tanaka et al. (2009); (69) Tanaka et al. (2007); (70) Wang, Lu & Gotthelf (2006a); (71) Wang et al. (2002b); (72) Phillips & Marquez-Lugo (2010); (73) Hewitt, Yusef-Zadeh & Wardle (2008); (74) Reich & Fuerst (1984); (75) Gray (1994); (76) Roy & Bhatnagar (2006); (77) Marquez-Lugo & Phillips (2010); (78) Borkowski et al. (2013); (79) Yamauchi et al. (2014); (80) Inui et al. (2009); (81) Green (2014); (82) Yusef-Zadeh, Hewitt & Cotton (2004); (83) Nord et al. (2004); (84) Uchiyama et al. (2011); (85) Heinke et al. (2009); (86) Muno et al. (2006); (87) Mori et al. (2005); (88) Skinner et al. (1990); (89) Pavlinsky, Grebenev & Sunyaev et al. (1994); (90) Degenaar et al. (2012); (91) Ponti et al. (2014); (92) Porquet, Decourchelle & Warwick (2003a); (93) Del Santo et al. (2006); (94) Soldi et al. (2014); (95) Sakano et al. (2005); (96) Trap et al. (2009); (97) Porquet et al. (2005b); (98) Muno et al. (2005b); (99) Koch et al. (2014); (100) Degenaar et al. (2013); (101) Dwelly & Ponti (2013); (102) Rea et al. (2013); (103) Kaspi et al. (2014); (104) Wijnands et al. (2002); (105) Natalucci et al. (2004); (106) Werner et al. (2004); (107) Bélanger et al. (2006); (108) Kuulkers et al. (2007); (109) Piraino et al. (2012); (110) Castro et al. (2013); (111) Reynolds & Miller (2010); (112) Natalucci et al. (2014); (113) Soldi et al. (2006); (114) Paizis et al. (2009) (115) Lu et al. (2013); (116) Do et al. (2013); (117) Yelda et al. (2014); (118) Bamba et al. (2000); (119) Bamba et al. (2009); (120) Ohnishi et al. (2011); (121) Hales et al. (2009); (122) Ponti et al. (2015).

allows us to be more confident about the spectral decomposition, e.g. compared to single RGB maps, retaining most of the morphological information on sufficiently large scales (i.e. beyond few arcmin scales).

The general assumption is that the emission at any position can be represented by the linear sum of three main components, namely (i) a soft plasma with a temperature of 1 keV (Kaneda et al. 1997; Bamba et al. 2002); (ii) a hot plasma of temperature 6.5 keV and

Table 3. Atlas of diffuse X-ray-emitting features. The first two columns in the table indicate the name primarily used in this work to refer to the feature as well as the other names used in the previous literature. The third and fourth columns show the coordinates of each feature as well as its approximate projected size. Finally, the fifth column provides references to selected works discussing the feature. For convenience, we report in Table 2 all the references ordered according to the numbering used in this table. The other names column shows the different designations used in previous literature. In the case of bubbles, these features are not necessarily referring to the same structure but to features forming the bubble candidate.

ATLAS OF DIFFUSE X-RAY-EMITTING FEATURES

Name	Other name or associated features	Coordinates (l, b)	Size (arcmin)	References
STAR CLUSTERS:				
Central cluster		359.9442, −0.046	0.33	45,115,116,117
Quintuplet		0.1604, −0.0591	0.5	1,63,11
Arches	G0.12+0.02	0.1217, 0.0188	0.7	1,2,3,4,5,6,7,8,9,11,39,40
Sh2−10[a]	DB−6	0.3072,−0.2000	1.92	10,11,12,63
Sh2−17[a]	DB−58	0.0013, 0.1588	1.65	11,13,63
DB−05[a]	G0.33−0.18	0.31 −0.19	0.4	11,22,63
SNR and Super-bubbles candidates:				
G359.0−0.9[b]	G358.5−0.9–G359.1−0.9	359.03,−0.96	26 × 20	X-R 48,51,75,76,81,118,119
G359.07−0.02	G359.0−0.0	359.07,−0.02	22 × 10	R 14,48,51,66
	G359.12−0.05	359.12,−0.05	24 × 16	X 66
G359.10−0.5[b]		359.10,−0.51	22 × 22	X-R 37,48,51,56,74,75,81,119,120
G359.41−0.12		359.41,−0.12	3.5 × 5.0	X 14
Chimney[c]		359.46,+0.04	6.8 × 2.3	X 14
G359.73−0.35[d]		359.73,−0.35	4	X 58
G359.77−0.09	Superbubble	359.77,−0.09	20 × 16	X 15,16,17,58
	G359.9−0.125	359.84,−0.14	15 × 3	X 15,16,17,58
	G359.79−0.26[e]	359.79,−0.26	8 × 5.2	X 15,16,17,58
	G0.0-0.16[f]	0.00,−0.16		X This work
20 pc lobes		359.94, −0.04	5.88	X-R 32,33,34,17
G359.92−0.09[g]	Parachute – G359.93-0.07	359.93,−0.09	1	R 35,38,43,47,58,60,61
Sgr A East	G0.0+0.0	359.963, −0.053	3.2 × 2.5	X-R 5,18,19,20,48,75,81
G0.1−0.1	Arc Bubble	0.109,−0.108	13.6 × 11	X This work
	G0.13.−0.11[h]	0.13,−0.12	3 × 3	X 17
G0.224−0.032		0.224,−0.032	2.3 × 4.6	X This work
G0.30+0.04	G0.3+0.0	0.34,+0.045	14 × 8.8	R 21,48,51,81,82
	G0.34+0.05			
	G0.33+0.04			
G0.42−0.04	Suzaku J1746.4−2835.4	0.40,−0.02	4.7 × 7.4	X 22
	G0.40-0.02			
G0.52−0.046		0.519,−0.046[i]	2.4 × 5.1	This work
G0.57−0.001		0.57,−0.001	1.5 × 2.9	This work
G0.57−0.018[j]	CXO J174702.6−282733	0.570,−0.018	0.2	X 23,24,58,59,68,80
G0.61+0.01[j]	Suzaku J1747.0−2824.5	0.61,+0.01	2.2 × 4.8	X 22,65,79
G0.9+01[k]	SNR 0.9+0.1	0.867,+0.073	7.6 × 7.2	R 25,26,27,28,29,48,75,81,82
DS1	G1.2−0.0	1.17,+0.00	3.4 × 6.9	X 31
Sgr D SNR	G1.02−0.18	1.02,−0.17	10 × 8.0	R 30,31,48,51,75,77,81,82
	G1.05−0.15			
	G1.05−0.1			
	G1.0−0.1			
G1.4−0.1		1.4,−0.10	10 × 10	R 73,81,82

Notes. [a]The low X-ray absorption towards these star clusters indicate that they are located in front of the GC region. [b]The Chimney is most probably either part of a large-scale structure (see Section 8.7) or an outflow from G359.41−0.12 (Tsuru et al. 2009), therefore most probably it is not a separate SNR. [c]Because of the low X-ray absorption column density ($N_{\rm H} \sim 2 \times 10^{22}$ cm^{-2}) this is most probably a foreground source (Bamba et al. 2000, 2009). [d]Most probably a foreground feature. [e]This feature appears to be part of the superbubble G359.77−0.09. [f]New extended X-ray feature, possibly part of the superbubble G359.77−0.09. [g]The interpretation as an SNR is probably obsolete. [h]This feature appears to be part of the arc bubble. [i]Possibly connected to G0.61+0.01. [j]Possibly due to a thermal filament. [k]X-ray emission primarily non-thermal, therefore it appears also in the next table.

(iii) a non-thermal component modelled by an absorbed power-law plus a neutral, narrow iron line (with 1 keV equivalent width), that are subject to an additional absorbing column of $N_{\rm H} = 10^{23}$ cm^{-2}. All three components are also absorbed by gas in front of the GC region and both thermal plasmas are modelled using the APEC model in XSPEC. The resulting model is therefore PHABS (APEC + APEC + PHABS (POWERLAW + GAUSS)) and has only three free parameters: the relative normalizations of the three components. The hot-plasma component represents the emission associated with faint unresolved point sources, whose cumulative spectrum is well described by a thermal spectrum (Revnivtsev et al. 2009) plus a possibly truly diffuse hot-plasma component (Koyama et al. 2007). The spectral index of the

Table 4. Atlas of diffuse X-ray-emitting features. This table has the same structure as Table 3. Because of possible misplacements between the peak emission of the radio and X-ray counterparts of filaments, SNR, PWN and other diffuse structures (generally related to the different ages of the population of electrons traced at radio and X-ray bands), when available we give the best X-ray position (following the preference: *Chandra*, *XMM–Newton*, *Suzaku*), otherwise we state the radio position. We cite the literature results separating these between the X-ray (X) from the radio (R) detections. For convenience, we report in Table 2 all the references ordered according to the numbering used in this table.

ATLAS OF DIFFUSE X-RAY-EMITTING FEATURES				
Name	Other name or associate features	Coordinates (l, b)	Size (arcsec)	References
	Radio and X-ray filaments and PWN candidates:			
Snake	G359.15−0.2	359.15,−0.17	312 × 54	R 48
G539.40−0.08		359.40,−0.08	27.5 × 5.1	X 41
G359.43−0.14		359.43,−0.14	21.4 × 3.9	X 41
Sgr C Thread		359.45,−0.01	500 × 42	R 48,51
Ripple filament	G359.54+0.18	359.548,+0.177	320 × 55	R 43,44,48,51
G359.55+0.16	X-ray thread Suzaku J174400−2913	359.55,+0.16	56.1 × 8.0	X 13,41,42,43,79
Crescent	G359.79+0.17 Curved filament	359.791,+0.16	300 × 74	R 63,50,51
Pelican	G359.85+0.47	359.859,+0.426	300 × 54	R 48,50,51
Cane	G359.87+0.44 G359.85+0.39	359.87,+0.44	420 × 50	R 48
Sgr A−E	G359.889−0.081- wisp XMM J174540−2904.5 G359.89−0.08	359.889,−0.081	20 × 5	R X 5,35,41,42,43,44,50,55
G359.897−0.023		359.897,−0.023	6.4 × 4	X 55
G359.899−0.065	Sgr A−F G359.90−0.06	359.899,−0.065	6.5 × 2.5	X 42,44,55
G359.904−0.047		359.904,−0.047	6.5 × 3	X 55
G359.915−0.061		359.915,−0.061	7 × 2	X 55
G359.91−1.03		359.919,−1.033	138 × 36	R 48
G359.921−0.030	F7	359.921,−0.030	7.5 × 3	X 42,55
G359.921−0.052		359.921,−0.052	5.5 × 2	X 55
The Mouse	G359.23−0.82	359.30,−0.82	156 × 108	PWN F 37,48,57,121
G359.925−0.051		359.925,−0.051	8 × 2.2	X 55
G359.933−0.037	F2	359.934,−0.0372	12 × 3	X 41,42,55
G359.933−0.039	F1	359.933,−0.039	5 × 2	X 42,55
G359.941−0.029		359.941,−0.029	6 × 2	X 41,55 Stellar wind
G359.942−0.045		359.942,−0.045	5 × 3	X 55
G359.944−0.052		359.944,−0.052	9 × 1.5	X 41,55
G359.945−0.044		359.945,−0.044	6 × 2.5	X 41,1,42,55 PWN
G359.95−0.04		359.950,−0.043	10 × 4	X 55,70 PWN
G359.956−0.052		359.956,−0.052	4 × 2.5	X 55
G359.959−0.027	F5	359.959,−0.027	9 × 3	X 41,42,55
Southern thread	G359.96+0.09 359.96+0.09	359.96,+0.11	500 × 40	R 48,50,51
G359.962−0.062		359.962,−0.062	5.5 × 3.5	X 55
G359.964−0.053	F3	359.964,−0.053	16 × 3.5	X 41,42,45,55 PWN
G359.965−0.056	F4	359.965,−0.056	9 × 3	X 42,55
G359.969−0.033		359.969,−0.033	5 × 2	X 55
G359.970−0.009	F8	359.970,−0.009	10 × 2.5	X 41,42,55 PWN
G359.971−0.038	F6	359.971,−0.038	16 × 8	X 41,42,55 PWN
G359.974−0.000	F9	359.974,−0.000	7 × 2	X 42
G359.977−0.076		359.977,−0.076	6 × 4	X 55
Cannonball	J174545.5−285829	359.983,−0.0459	30 × 15	X-R PWN 36
G359.983−0.040		359.983,−0.040	6.5 × 4.5	X 42,55
G359.98−0.11		359.979,−0.110	Streak	R 50
G0.007−0.014	G0.008−0.015	0.008,−0.015	11 × 3.5	X 41,55
G0.014−0.054		0.014,−0.054	18 × 14	X 55
G0.017−0.044	MC2	0.017,−0.044	15 × 4	X 41,42 FeKa
G0.02+0.04		0.0219,+0.044	Streak	R 50
G0.021−0.051		0.021,−0.051	15 × 12	X 55
G0.029−0.08		0.029,−0.08	29 × 18	X 55
G0.032−0.056	G0.029−0.06 – F10 G0.03−0.06	0.0324,−0.0554	35 × 6	FeKa 41,42,55 PWN

Table 4 – *continued*

ATLAS OF DIFFUSE X-RAY-EMITTING FEATURES				
Name	Other name or associate features	Coordinates (l, b)	Size (arcsec)	References
	Radio and X-ray filaments and PWN candidates:			
G0.039−0.077		0.039,−0.077	22 × 15	X 55
G0.062+0.010	G0.06+0.06	0.062,+0.010	40 × 25	R 50,55
Northern thread	G0.09+0.17	0.09,+0.17	714 × 48	R 48,49,50,51
	G0.08+0.15			
G0.097−0.131		0.097,−0.131	70 × 50	X 55
Radio Arc	GCRA	0.167,−0.07	1690 × 145	R 38,48,49,50,51
	G0.16−0.15			
G0.116−0.111		0.116,−0.111	50 × 40	X 55
G0.13−0.11		0.13,−0.11	55 × 12	71,17,41,42 PWN
G0.15−0.07	Steep spectrum of Radio Arc	0.138,−0.077		R 50
XMM J0.173−0.413	G0.17−0.42	0.173,−0.413	180 × 18	X This work
	S5	0.17,−0.42	160 × 9	R 82
G0.223−0.012		0.223,−0.012	50 × 20	X 41
G0.57−0.018[a]	CXO J174702.6−282733	0.57,−0.0180	0.33	X 23,24,58,59,68,79,80
G0.61+0.01[a]		0.61,+0.01	132 × 288	X 22,65,79
G0.9+0.1		0.9,+0.1		PWN

[a]Possibly part of a young SNR.

non-thermal component is assumed to be $\Gamma = 2$, consistent with the values measured through the combined spectral fits of *XMM–Newton* spectra with higher energy data (e.g. *INTEGRAL* and/or *NuSTAR*; Terrier et al. 2010; Mori et al. 2015, submitted; Zhang et al. 2015, submitted).

The strongest assumptions in this approach are that the emission can be represented everywhere with these three components. This obviously fails on bright point sources or on regions where the emission is much hotter (e.g. Sgr A East). For the soft components the even stronger assumption is that absorption to the GC is assumed to be uniform over the CMZ at a value of $N_{\rm H} = 6 \times 10^{22}$ cm^{-2} (Sakano et al. 2002; Ryu et al. 2009), putting aside absorption in the GC region itself. Clear column density modulations are observed towards different lines of sight (e.g. Ryu et al. 2009; Ryu et al. 2013). We tested significantly different column densities (up to $N_{\rm H} = 1.5 \times 10^{23}$ cm^{-2} characteristic of several GC sources; see e.g. Baganoff et al. 2003; Rea et al. 2013; Ponti et al. 2015). We found that if the soft plasma normalization is significantly modified, the overall morphology is consistent. We tested various values of the other parameters (spectral index or temperatures) and did not find strong effects on the soft plasma morphology or normalization.

We first produced counts, exposure and background maps for each observation and each instrument. Background was obtained from cal-closed data sets distributed in the ESAS[5] calibration data base. For each observation and instrument, an average RMF is computed as well as the unvignetted ARF. For each instrument, individual observation images were reprojected using the final image astrometry and then combined to compose a mosaic. Average ARF and RMF for each instrument were obtained with the FTOOLS[6] routines ADDRMF and ADDARF.

For each pixel of the final maps, we fit the measured numbers of counts in all the energy bands and instruments with a model consisting of the three aforementioned components as well as the background events number and the OoT events for the EPIC-pn camera. The free parameters are the normalization of each individual component. We apply Cash statistics (Cash 1979) to take into account the low statistics in each pixel. This analysis allows us to perform a rough spectral decomposition, better separating the spectral emission components, although retaining the maximum spatial resolution. Fig. 16 presents the map of the normalization (in units of 10^{-4} times the APEC normalization) of the soft thermal emission component. The normalization of the soft thermal component has a distribution similar to the one traced by the soft lines and the continuum (Figs 3, 10, 11 and 14). Enhanced high-latitude soft plasma emission is observed. The white dashed lines show the position of two sharp edges in the distribution of this high-latitude emission (see also Figs 3, 10 and 11). The white solid line shows the edge of the region having more than 7.2 ks of exposure (see Fig. 1).

6 AN ATLAS OF DIFFUSE X-RAY-EMITTING FEATURES

The patchy and non-uniform distribution of the diffuse emission makes the recognition of the shape, the border and connection of the different structures and components difficult. Occasionally, different works report the same X-ray feature with different names and shapes and, in extreme cases, the same X-ray-emitting feature is associated with different larger scale complexes.

In Tables 3 and 4, we report all the new X-ray features discussed in this paper, plus many GC features presented in previous works. The main purpose of these tables is to provide a first step towards the building of an atlas of diffuse X-ray-emitting GC features. The table is available online at: http://www.mpe.mpg.de/HEG/GC/AtlasGCdiffuseX-ray and will be updated, should the authors be notified of missing extended features. This exercise is clearly prone to incompleteness and deficiencies; however, we believe this might help in providing a clearer and more systematic picture of the diffuse X-ray emission from the GC region. The spatial location and size of all these features is shown in the finding charts in Figs 5 and 6.

[5] http://xmm2.esac.esa.int/external/xmm_sw_cal/background/epic_esas.shtml
[6] https://heasarc.gsfc.nasa.gov/ftools/ftools_menu.html

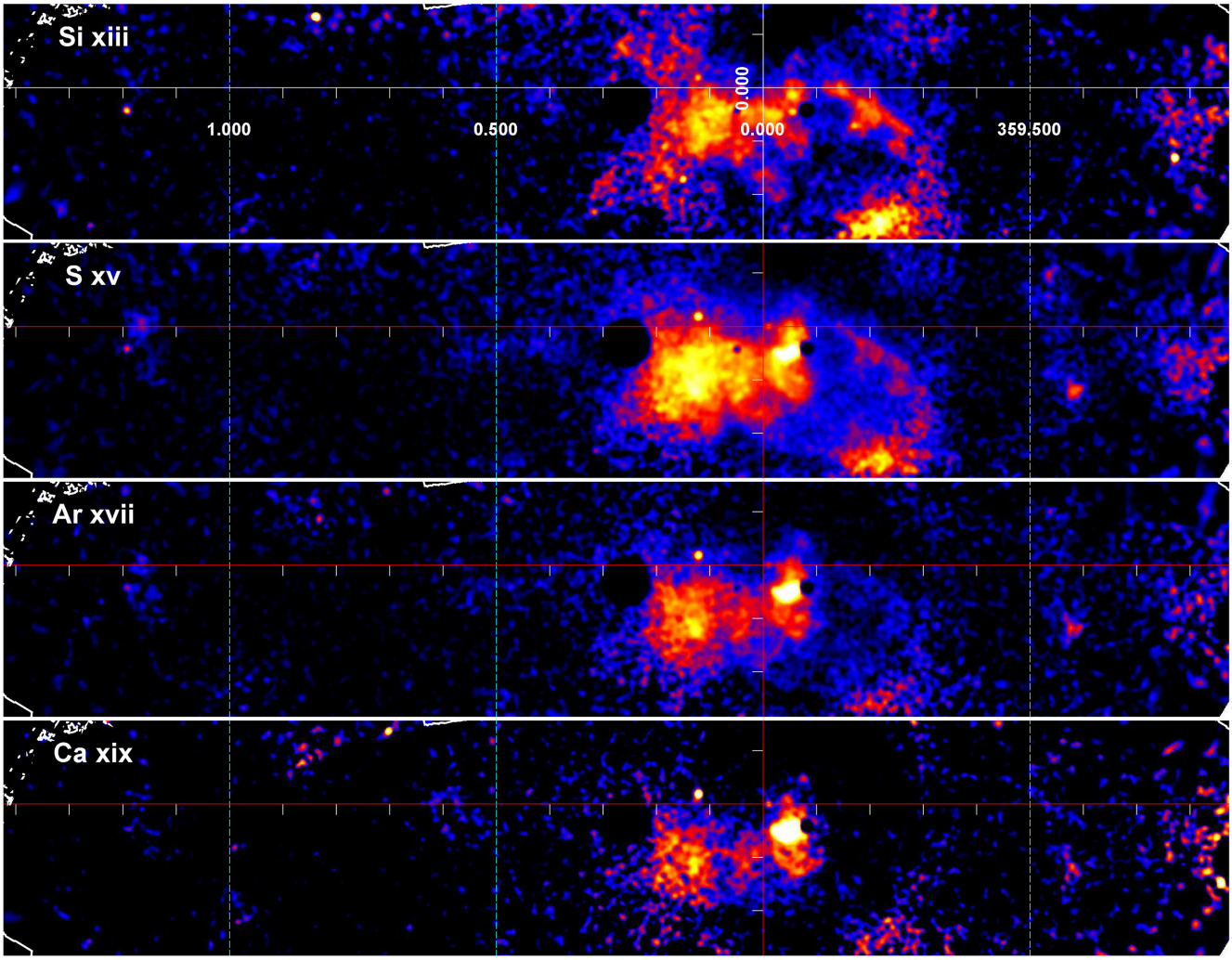

Figure 14. From top to bottom, continuum-subtracted Si XIII, S XV, Ar XVII, Ca XIX intensity maps of all the stacked *XMM–Newton* observations of the CMZ.

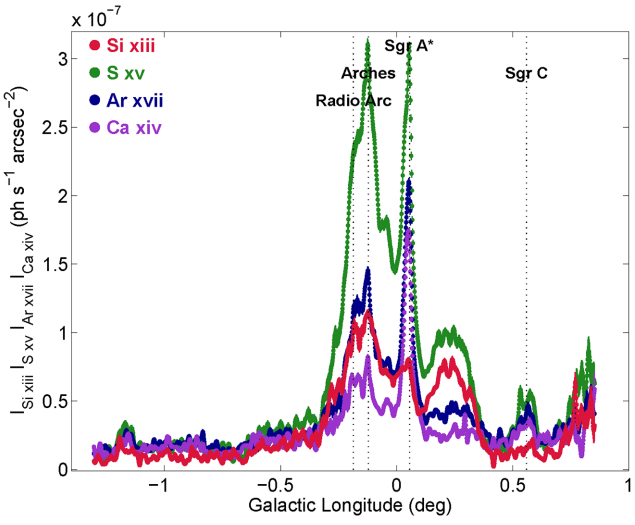

Figure 15. Longitudinal intensity profiles of the Si XIII (red), S XV (green), Ar XVII (blue) and Ca XIX (violet) emission lines, integrated over Galactic latitude within the magenta rectangular region shown in Fig. 14.

7 THE FOREGROUND COLUMN DENSITY

Given the high column densities of neutral or weakly ionized material absorbing the soft X-ray radiation, it is important to estimate the effects of X-ray obscuration. For example, a molecular complex having a column density of $N_{\rm H} \sim 10^{25}$ cm^{-2}, such as the Sgr B2 core, would completely obscure the radiation below about 4 keV, if placed in front of the GC; see Fig. 2.

To calculate the effects of absorption of the X-ray emission, we computed the flux generated by a thermally emitting plasma with temperature of $kT = 1$ keV (using a PHABS*APEC model), in both the 2–4.5 and 4.5–10 keV bands, after being absorbed by a given column density of neutral material (see also Fig. 2). For each column density explored, we report in Table 5 the ratio of the observed flux ($F_{2-4.5}$ and $F_{4.5-10}$) over the respective unabsorbed ($F0$) flux. We note that the hard X-ray band starts to be affected (corresponding to flux reductions up to a factor of 2) for column densities up to $N_{\rm H} \sim 3 \times 10^{23}$ cm^{-2} while it is heavily affected (flux reduction of a factor of 10 or more) for $N_{\rm H} \sim 10^{24}$ cm^{-2} or higher (see Table 5). At lower energies, the obscuration effect is even more pronounced. Already, for $N_{\rm H} \sim 3 \times 10^{22}$ cm^{-2}, the observed flux is less than half and for $N_{\rm H} \gtrsim 5 \times 10^{23}$ cm^{-2} it is less than 0.1 per cent of its unobscured flux. This indicates that the softer band is expected to be heavily affected by absorption.

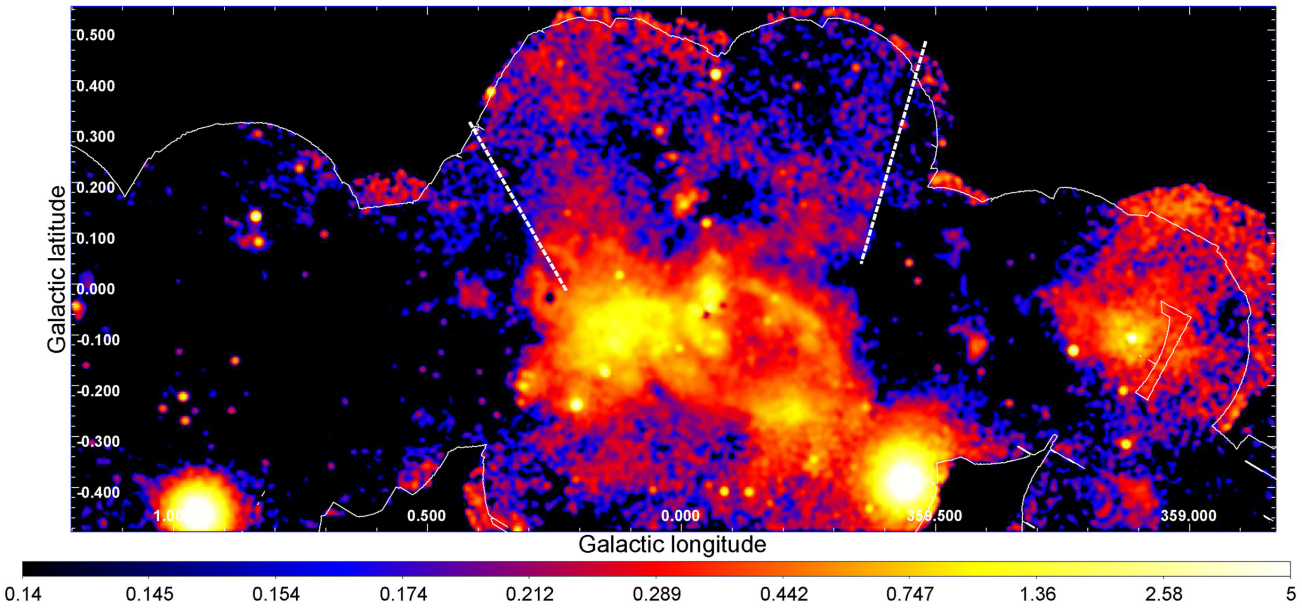

Figure 16. Map of the normalization of the soft thermal gas component (in units of 10^{-4} times the APEC normalization). The white lines indicate the extent of the survey having more than 7.2 ks exposure. The white dashed lines show the position of the two sharp edges in the distribution of the high-latitude plasma. Some bright point sources (i.e. 1E 1743.1−2843, AX J1745.6−2901, 1E 1740.7−2942, GRS 1741.9−2853) have been removed, thereby producing artificial holes in the maps at their respective locations.

Table 5. Expected ratio of the obscured flux to the unobscured flux for different values of the column density of obscuring material. A thermally emitting gas with temperature of $kT = 1$ keV (PHABS*APEC model) is assumed in the computations. The predicted observed flux in both the 2–4.5 and 4.5–10 keV bands ($F_{2-4.5}$ and $F_{4.5-10}$) is computed and compared to the respective unabsorbed ($F0$) flux.

$N_{\rm H}$ (10^{22})	$F_{2-4.5}/F0$	$F_{4.5-10}/F0$
0.01	1	1
1	0.776	0.968
3	0.488	0.912
5	0.322	0.857
7	0.223	0.809
10	0.137	0.737
15	0.0698	0.636
30	0.0156	0.414
50	0.0033	0.244
70	0.0008	0.149
100	1.2×10^{-4}	0.0754
150	6.2×10^{-5}	0.0273

7.1 Column density distribution

The top panel of Fig. 8 shows the neutral hydrogen column density distribution as derived from dust emission (Molinari et al. 2011).[7] The image shows the $N_{\rm H}$ distribution in logarithmic scale in the range $N_{\rm H} = 4.5 \times 10^{22}$–$3.8 \times 10^{25}$ cm^{-2}. This total column density estimated from the dust has large uncertainties that can be mainly ascribed to the uncertainty associated with the dust-to-$N_{\rm H}$ ratio. In particular, the column densities shown in this map appear to be systematically larger than what is measured with other methods. For example, the column density of the G0.11−0.11 massive cloud is estimated to be $N_{\rm H} \sim 5$–6×10^{23} cm^{-2} in this map, while Amo-Baladrón et al. (2009) measure $N_{\rm H} \sim 2 \times 10^{22}$ cm^{-2}, through a detailed modelling of the molecular line emission. The core of Sgr B2 is estimated by Molinari et al. (2011) to have $N_{\rm H} \sim 3 \times 10^{25}$ cm^{-2}, while modelling of the X-ray emission (Terrier et al. 2010) suggests $N_{\rm H} \sim 7 \times 10^{23}$ cm^{-2}, more than an order of magnitude lower. Moreover, the average column densities of G0.40−0.02, G0.52−0.046, G0.57−0.018 and a fourth region (the magenta ellipse in Fig. 9) are estimated to be $N_{\rm H} \sim 4 \times 10^{23}$, 4×10^{23}, 1.2×10^{24} and 1.5×10^{24} cm^{-2}, respectively, from the dust map, while they are measured to be in the range $N_{\rm H} \sim 7$–10×10^{22} cm^{-2}, from modelling of the X-ray emission. Therefore, the total normalization of the $N_{\rm H}$ map built from the dust emission appears to be overestimated. However, the method employed to produce it does not suffer from self-absorption, so it is presumably giving unbiased relative $N_{\rm H}$ ratios.

7.2 X-ray emission modulated by absorption

The bottom panel of Fig. 8 shows the X-ray map with the column density contours overlaid for comparison. We observe that, as expected, no soft X-ray emission is observed towards the central part of the most massive molecular cores. In particular, we observe depressed X-ray emission from (i) the Sgr B2 nucleus and its envelope (with $N_{\rm H} > 7 \times 10^{23}$ cm^{-2}); (ii) the almost perfect coincidence between the hole in soft X-ray emission east of G0.224−0.032 (see Figs 5 and 9) and the shape of the so-called Brick molecular cloud, M0.25+0.01 (see Fig. 5; Clark et al. 2013); (iii) the core of the Sgr C complex;[8] (iv) the regions around DB-58 and at Galactic position

[7] We do not show the entire CMZ, because of the limited coverage of the *Herschel* dust emission map (Molinari et al. 2011).

[8] At this location a sharp transition in the soft X-ray emission, with an arc-like shape, is observed. This is spatially coincident to the edge of a very

Table 6. Fluxes (F) and surface brightnesses (f) of the continuum and the line intensities (line plus continuum) integrated over the small and big boxes described in Section 8.1. The fluxes are given in units of 10^{-12} erg cm^{-2} s^{-1}, while the surface brightnesses are given in 10^{-15} erg cm^{-2} s^{-1} arcmin^{-2}.

Big box		Small box	
Flux	Surf. bright.	Flux	Surf. bright.
$F_{1-2\,\mathrm{keV}} = 19.0$	$f_{1-2\,\mathrm{keV}} = 6.2$	$F_{1-2\,\mathrm{keV}} = 12.9$	$f_{1-2\,\mathrm{keV}} = 6.9$
$F_{2-4.5\,\mathrm{keV}} = 155.0$	$f_{2-4.5\,\mathrm{keV}} = 50.7$	$F_{2-4.5\,\mathrm{keV}} = 119.3$	$f_{2-4.5\,\mathrm{keV}} = 64.3$
$F_{4.5-12\,\mathrm{keV}} = 290.7$	$f_{4.5-12\,\mathrm{keV}} = 95.1$	$F_{4.5-12\,\mathrm{keV}} = 219.0$	$f_{4.5-12\,\mathrm{keV}} = 118.0$
$F_{\mathrm{Si\,XIII}} = 4.4$	$f_{\mathrm{Si\,XIII}} = 1.5$	$F_{\mathrm{Si\,XIII}} = 3.4$	$f_{\mathrm{Si\,XIII}} = 1.8$
$F_{\mathrm{S\,XV}} = 15.1$	$f_{\mathrm{S\,XV}} = 4.9$	$F_{\mathrm{S\,XV}} = 12.0$	$f_{\mathrm{S\,XV}} = 6.4$
$F_{\mathrm{Ar\,XVII}} = 15.1$	$f_{\mathrm{Ar\,XVII}} = 4.9$	$F_{\mathrm{Ar\,XVII}} = 11.9$	$f_{\mathrm{Ar\,XVII}} = 6.4$
$F_{\mathrm{Ca\,XIX}} = 18.4$	$f_{\mathrm{Ca\,XIX}} = 9.9$	$F_{\mathrm{Ca\,XIX}} = 14.3$	$f_{\mathrm{Ca\,XIX}} = 7.7$

$l \sim 0.^\circ2$, $b \sim -0.^\circ48$ also appear to have darker colours and, once again, it is possible to find molecular complexes (M0.018+0.126 and M0.20−0.48) covering roughly the same region (see Figs 5 and 8). All these clouds are characterized by very high column densities $N_{\mathrm{H}} \gtrsim 3$–7×10^{23} cm^{-2} and they most probably lie in front of Sgr A* and of most of the GC (e.g. according to the twisted ring model of Molinari et al. 2011). Therefore, they are absorbing the GC's extended, soft X-ray emission.

All this evidence suggests that at least the most massive clouds located in front of the GC do actually modulate (obscure) the soft X-ray emission. However, fluctuations in column densities cannot be the only cause for the observed distribution of soft X-ray emission for two reasons. First, we do observe only weak soft X-ray emission along some lines of sight having a low column density of molecular material (such as around the Sgr C and Sgr D complexes and south of the Sgr B1 region). Secondly, we do detect intense (among the brightest) soft X-ray emission from several regions such as the Sgr A complex and the cores of the Sgr C and Sgr D complexes, where some of the highest column density clouds are found. In particular, in Sgr A very intense soft X-ray emission is observed along the line of sight towards the 50 km s^{-1}, the Bridge (Ponti et al. 2010) and the G0.11−0.11 clouds, some of the highest column density clouds in the CMZ. Although this might be explained by placing these clouds on the far side of the CMZ, it appears that these regions are characterized by truly enhanced soft X-ray emission (see e.g. Sections 8.4, 8.5 and 8.6). We defer the detailed disentangling of these effects to an elaborate spectral study of these regions.

8 DISCUSSION

In the process of systematically analysing all *XMM–Newton* observations of the central degrees of the Galaxy, we have discovered several new extended features and have produced an atlas of known, extended soft X-ray features. Here we discuss their general properties and investigate the origin/existence of several specific features.

8.1 General properties

To compute the total observed (absorbed) flux from the CMZ we first mask out the emission from the brightest binaries, by excluding a circle with a radius of 1 arcmin around SAX J1747.7−2853; 1.5 arcmin for AX J1745.6-2901 and GRS1741.9-2853; 2 arcmin for XMMU J174445.5−295044; 2.5 arcmin for 1E 1743.1−2843; 3.5 arcmin for IGR J17497−2821 and 1E 1740.7−2942 (see the white circles in Fig. 5). We then compute the total observed count rate from two boxes, one with a size of $1.^\circ5 \times 0.^\circ35$ ($l \times b$) and centred on Sgr A* and one with a bigger size of $2.^\circ08 \times 0.^\circ413$ centred on $l = 0.^\circ232$, $b = 0.^\circ080$. We then measure the total count rate within these regions and convert it into a flux[9] assuming that the soft X-ray diffuse emission is dominated by a thermally emitting plasma with a temperature of $kT = 1$ keV (Kaneda et al. 1997; Bamba et al. 2002). In particular, we assumed an APEC emission component with temperature $kT = 1.08$ keV, absorbed by a column density of neutral material of $N_{\mathrm{H}} = 6 \times 10^{22}$ cm^{-2} and with a solar abundance.

The fluxes of the integrated continuum and line intensities (line plus continuum) within the big and small boxes are reported in Table 6. This corresponds to an observed 2–12 keV luminosity of $L_{2-12} = 3.4 \times 10^{36}$ erg s^{-1} and $L_{2-12} = 2.6 \times 10^{36}$ erg s^{-1} for the big and small boxes, respectively, assuming a distance of 8 kpc to the GC (Reid 1993; Reid et al. 2009).

8.2 A new X-ray filament, XMM J0.173−0.413

We observe a new X-ray filament extending ∼2.2 arcmin perpendicular to the Galactic plane and situated at $l = 0.^\circ173$, $b = -0.^\circ413$, which is almost directly towards negative longitudes from the GC Radio Arc (see Fig. 17). It coincides with the brightest segment of a much longer radio filament that extends towards the southernmost extensions of the filaments of the Radio Arc (Yusef-Zadeh & Morris 1989, 2004; see figs 7a, 16b,c, and 17a,b,c of the latter reference, where the filament is labelled 'S5'), but because it is not continuous or exactly parallel with the filaments of the arc, it is not completely evident that it is an extension of the arc in three dimensions. The X-ray filament has a hard X-ray colour and does not appear in the soft line images, indicating a non-thermal emission spectrum.

Three other non-thermal radio filaments have been found to have X-ray emission along some portion of their lengths: G359.54+0.18, G359.89−0.08 and G359.90−0.06 (Lu, Wang & Lang 2003; Sakano et al. 2003; Lu et al. 2008; Johnson et al. 2009; Morris, Zhao & Goss 2014; Zhang et al. 2014). XMM 0.173−0.413 is the

dense core of dust, suggesting that the modulation in the soft X-ray emission is induced by obscuration by the molecular cloud.

[9] To perform this task we use WEBPIMMS: https:heasarc.gsfc.nasa.govcgi-binToolsw3pimmsw3pimms.pl. As explained in Section 2.1, the combined count rate is the sum of the EPIC-pn plus the EPIC-MOS count rates after scaling the latter exposure maps by 0.4. We then use the EPIC-pn, medium-filter, rate-to-flux conversion computed with WEBPIMMS.

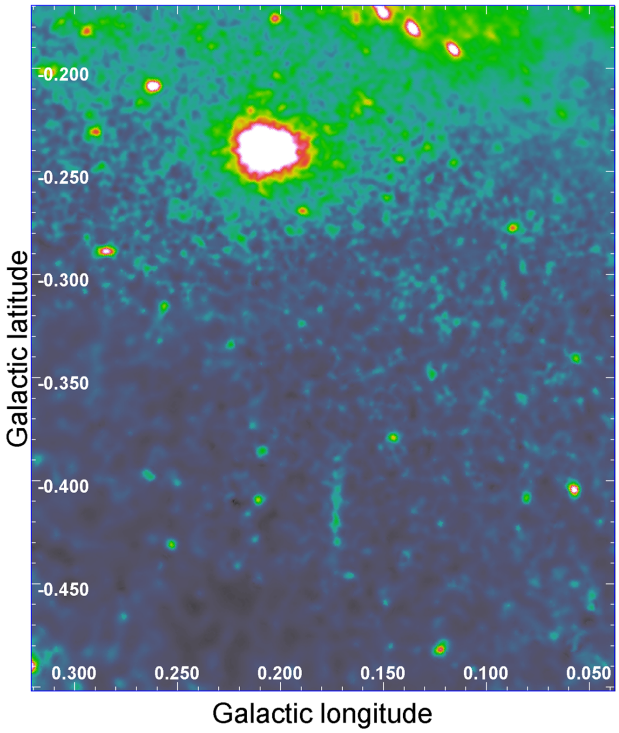

Figure 17. *XMM–Newton* image in the 2–12 keV band showing the new X-ray filament located south of the Radio Arc. The filament is located at $l \simeq 0.^{\circ}173$ and $b \simeq -0.^{\circ}413$ and appears as a thin (<0.15 arcmin) and long (∼2.7 arcmin) filament running along the north–south direction, as the Radio Arc. The brightest source in the image is SAX J1747.7−2853.

only one of the four known cases where the X-ray emission is not at or near a location where the radio filament shows unusually strong curvature.

8.3 SNR excavated bubbles within the CMZ?

The top and bottom panels of Fig. 9 show the X-ray (2.5–4.5 keV) and 850 μm (Pierce-Price et al. 2000) maps of the Sgr B1 region. Four enhancements of X-ray emission are clearly present (shown by the green dashed ellipses in Fig. 9). In particular, G0.570−0.001, G0.52−0.046 and G0.40−0.02 correspond to holes in the dust distribution derived from the 850 μm radiation (see the bottom panel of Fig. 9). To reinforce this evidence, we observe that their X-ray edges can be traced in the dust distribution all around the X-ray enhancements, suggesting a tight connection between the two. Such phenomenology is typical of SNe exploding within or near molecular clouds and interacting with them, creating bubbles in the matter distribution (Ferreira & de Jager 2008; Lakićević et al. 2015). Indeed, in this case, the SN ejecta might have cleared the entire region that is not filled with hot, X-ray-emitting plasma, pushing away the ambient molecular material. However, this is not the only possibility. The apparent X-ray enhancements could have resulted instead from a higher obscuration surrounding the sub-mm holes, leading to higher X-ray extinction at the edges. We note that none of these regions has a known radio SNR counterpart (see Fig. 9). However, the radio emission might be confused within the very high radio background of diffuse emission created by G0.30+0.04, the several H II regions present in this region (see Fig. 6), and the bright, extended synchrotron background of the GC. Enhanced X-ray emission has already been reported towards G0.40−0.02 (Nobukawa et al. 2008) and close to G0.570−0.001 (see the cyan ellipses in Fig. 9).

8.3.1 *Spectral analysis*

To further investigate the origin of these structures, we extracted a spectrum from each of these features (in either obsid 0694641301 or 0694641201). We fitted each spectrum with a model composed of an SNR emission component (fitted with a PSHOCK model; a constant temperature, plane-parallel plasma shock model, meant to reproduce the X-ray emission from an SNR in the Sedov phase) plus the emission components typical of the GC environment such as a hot thermal plasma (with temperature in the range: $kT = 6.5$–10 keV), and an Fe K α emission line, all absorbed by foreground neutral material (PHABS*(PSHOCK+APEC+GAUS) in XSPEC). We assume that all these components have solar abundances. Possible confusion effects produce uncertainties associated with the determination of the correct sizes of these candidate SNRs, so some of the results presented here, such as the dynamical time-scales, could thereby be affected.

G0.40−0.02 shows a best-fitting temperature and normalization of the warm plasma associated with the SNR component of $kT = 0.55 \pm 0.1$ keV and $A_{\rm psho} = 2.4^{+5}_{-1} \times 10^{-2}$, while the column density is observed to be $N_{\rm H} = 7.7 \pm 0.8 \times 10^{22}$ cm^{-2} (see also Nobukawa et al. 2008). To test whether the observed X-ray enhancement is due to a real variation of the intensity of the soft X-ray emission or whether it is the product of lower extinction, we also extracted a spectrum from a nearby background

Table 7. Best-fitting and derived parameters of the SNR candidates described in Section 8.3.

Parameter	Unit	G0.40−0.02	G0.52−0.046	G0.570−0.001	G0.224−0.032	Back
kT	keV	0.55 ± 0.1	$0.77^{+0.7}_{-0.2}$	0.6[a]	0.54 ± 0.1	0.55[c]
$A_{\rm psho}$		$2.4^{+5}_{-1} \times 10^{-2}$	$5^{+9}_{-3} \times 10^{-3}$	$4.3^{+11}_{-4} \times 10^{-3}$	$3^{+6}_{-2} \times 10^{-2}$	$<6 \times 10^{-3}$
τ[b]	s cm^{-3}	$>1.7 \times 10^{11}$	$>7.5 \times 10^{10}$	$>1.4 \times 10^{10}$	$>3.5 \times 10^{11}$	7.5×10^{11} [c]
Size	pc	8.6×5.5	5.9×2.7	4.2×2.1	5.4×2.6	8.6×5.5
$N_{\rm H}$	10^{22} cm^{-2}	7.7 ± 0.8	7.9 ± 1.1	9.5 ± 2	7.4 ± 1	8.8 ± 1
χ^2/dof		807/777	342/364	141/134	369/338	834/741
$n_{\rm e}$	cm^{-3}	1.4	1.4	2.1	11	
$t_{\rm dy}$	yr	3.7×10^3	1.7×10^3	1.6×10^3	1.8×10^3	
$E_{\rm th}$	erg	1.9×10^{50}	5.0×10^{49}	2.6×10^{49}	2.6×10^{50}	

[a]Value weakly constrained by the high column density of neutral material, therefore fixed for the corresponding fit. [b]Ionization time-scale of the shock plasma model. [c]Parameter unconstrained.

comparison region (magenta in Fig. 9 and 'Back' in Table 7). This second region has the same size as G0.40−0.02 and it is located in a fainter region in X-rays, characterized by higher $N_{\rm H}$, as suggested by the 850 μm map (see the bottom panel of Fig. 9). This background region shows a slightly higher absorption column density, $N_{\rm H} \sim 8.8 \pm 1 \times 10^{22}$ cm^{-2}, and no significant warm plasma component. If we impose the presence of a warm plasma component having the same temperature and τ (the ionization time-scale of the shock plasma model) as observed in G0.40−0.02 we obtain an upper limit to its normalization of $A_{\rm psho} < 6 \times 10^{-3}$. This suggests that the enhanced X-ray emission towards G0.40−0.02 is due to a real excess of X-ray emission and is not a simple byproduct of lower extinction. The thermal energy, the dynamical time-scale and the size of G0.40−0.02 are $E_{\rm th} \sim 1.9 \times 10^{50}$ erg, $t_{\rm dy} \sim 3700$ yr and 8.6×5.5 pc^2, respectively, as expected for a young SNR in the Sedov–Taylor phase (derived from the equations shown in Maggi et al. 2012).

Similar parameters characterize G0.52−0.046 ($kT = 0.77 \pm 0.3$ keV, $A_{\rm psho} = 5^{+7}_{-3} \times 10^{-3}$, $N_{\rm H} = 7.9 \pm 1.1 \times 10^{22}$ cm^{-2}). Therefore, this feature also appears to be consistent with an SNR origin. However, although we derive a dynamical age of the same order ($t_{\rm dy} \sim 1700$ yr), the energy inferred for the SN explosion is substantially lower, $E_{\rm th} \sim 5 \times 10^{49}$ erg.

The spectrum of G0.57−0.001 is characterized by significantly lower statistics and a higher column density of absorbing material. The best fit prefers a low temperature plasma, at the limit of detection. We fix its temperature to a relatively low value of $kT = 0.6$ keV and find $A_{\rm psho} = 4.3^{+11}_{-4} \times 10^{-3}$ and $N_{\rm H} = 9.5 \pm 2 \times 10^{22}$ cm^{-2}. The derived thermal energy and dynamical times are $E_{\rm th} \sim 2.6 \times 10^{49}$ erg and $t_{\rm dy} \sim 1600$ yr, respectively. The soft X-ray excess of this feature lies spatially very close to a region of X-ray excess that has been traced by Fe XXV line emission (Nobukawa et al. 2008). We also note that the region defining G0.57−0.001 almost completely contains a diffuse X-ray source detected both by the *Chandra* and *ASCA* satellites (Senda et al. 2002). The *Chandra* image shows a very compact (∼10 arcsec radius) and hot shell, G0.57−0.018, possibly the youngest SNR in the Galaxy, less than about 100 yr old. However, Renaud et al. (2006), because they found neither radio nor nucleosynthetic decay products (such as ^{44}Ti), questioned such an interpretation. Further investigations are required to understand the link, if any, between these features.

The morphology of G0.224−0.032 appears more complex, compared to the other SNR candidates. The edge of the X-ray emission is well defined only towards the Brick molecular cloud (designated M0.25+0.01 in Fig. 5) that, with its very high column density, can obscure the soft X-ray emission there. In any case, the fit of its X-ray spectrum shows parameters typical of an SNR. In particular, we derive a thermal energy and a dynamical time of $E_{\rm th} \sim 2.6 \times 10^{50}$ erg and $t_{\rm dy} \sim 1800$ yr, respectively. Therefore, G0.224−0.032 might be a new SNR partly obscured by the brick molecular cloud. In such a case, the true size and the energy estimate are likely larger.

Overall, we remark that, if these SNR candidates are real, their dynamical time-scales are extremely short, which would imply an extremely high SN rate. The SN rate in the CMZ has been estimated to be as high as 0.4 SN per millennium (Crocker & Aharonian 2011). However, we caution that our dynamical time-scales could be off either because of a higher ambient density than we have assumed, or because absorption or confusion effects do not allow us to distinguish the proper border of the SNRs, or to detect any colder and more extended portions that might be present.

8.3.2 *Expanding molecular shells*

The observed temperatures, ages and sizes of these SNR candidates are consistent with a Sedov–Taylor framework expanding into an average ambient density between 1 and 10 cm^{-3} (higher density environments would result in older and cooler SNRs; Ostriker & McKee 1988).

If the X-ray enhancements described above truly arise from SNRs interacting with and carving bubbles inside or near the surfaces of molecular clouds (preceded, perhaps, by the wind of the massive progenitor), we should observe clear traces of such events also in the kinematics of the surrounding molecular matter. Such a complex and delicate investigation is beyond the scope of the present paper. Nevertheless, we note that Tanaka et al. (2009) discovered an expanding SiO shell (SiO0.56−0.01) centred at $l \sim 0.^{\circ}56$, $b \sim -0.^{\circ}01$ and having a size of $\sim 3.0 \times 3.4$ pc^2. The centre and size of the expanding SiO shell closely match the peak and size of the X-ray emission of G0.57−0.001 and suggest an association between the two. In particular, high-velocity clumps have been found consistent with the idea that the SiO shell consists of swept-up material. Tanaka et al. (2009) calculated a kinetic energy of $E_{\rm kin} \sim 10^{50.4}$ erg for SiO0.56−0.01. This strongly suggests that G0.57−0.001 is indeed an SNR caught in the process of carving its bubble. Further studies of the gas kinematics around the other X-ray enhancements are required to establish their real nature.

We note that the thermal energy estimated for these SNRs is observed to be systematically lower than the theoretical value for the remnant of a standard Type II SN expanding into the interstellar medium. This might result from a relatively higher ambient density in the GC, leading to greater energy dissipation, or from a significant fraction of the energy budget going into the inflation of the bubbles and the production of cosmic rays.

We also note that G0.570−0.001, G0.52−0.046 and G0.40−0.02 are located within the trail of massive stars that have been hypothesized to have tidally escaped from the Quintuplet cluster (see Fig. 9 and Habibi et al. 2013, 2014). This raises the possibility that some of these SNRs might be associated with SN explosions from stars originating in this massive, young stellar cluster.

8.4 Origin of the Sgr A X-ray lobes

All the soft X-ray maps (see Figs 3, 7, 10, 11, 14 and 16) show the presence of two extended features, with a size of roughly 5–10 pc, located to the Galactic north and south of Sgr A*, the so-called bipolar Sgr A lobes (Morris et al. 2003, 2004b; Markoff et al. 2010; Heard & Warwick 2013a,b).

8.4.1 *Lobe morphology*

The lobes appear to have roughly oval shapes with co-aligned major axes oriented perpendicular to the Galactic plane. They appear joined at the position of Sgr A* suggesting the latter is their point of origin (see Fig. 18). The top panel of Fig. 11 and Fig. 7 show that the lobes' emission is characterized by a smaller ratio of soft X-ray lines to continuum (therefore characterized by a greener colour) compared to the surrounding regions (appearing with a redder colour) such as the superbubble, G0.1−0.1 and the Radio Arc (Figs 7, 11 and 18). This suggests that the lobes, although they show thermal emission lines (see Section 4.2), have either a stronger non-thermal component or significantly hotter

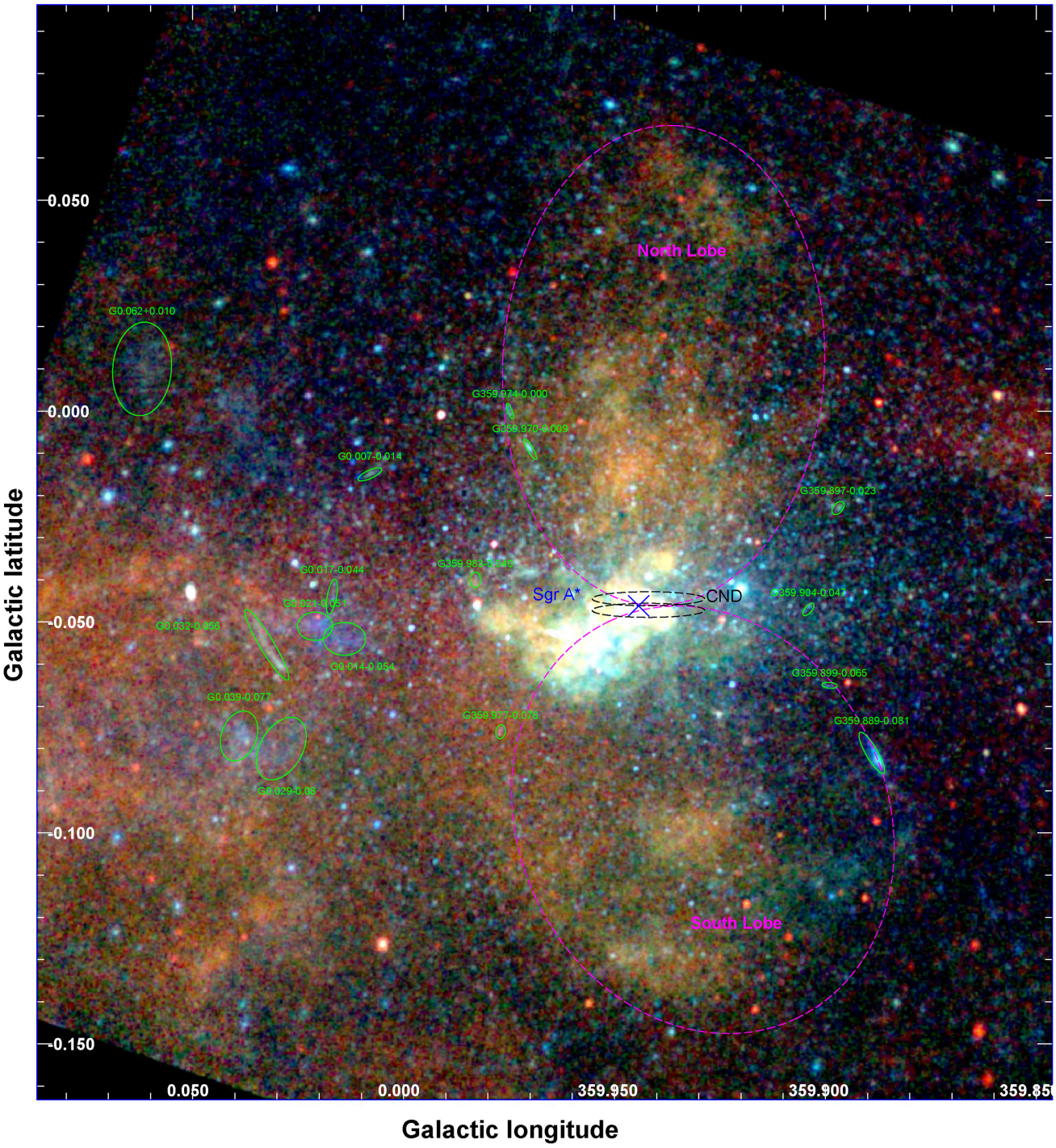

Figure 18. Finding chart. *Chandra* RGB image of all the ACIS-I observations pointed at Sgr A* (see Clavel et al. 2013 for data reduction and details on the image production). The red, green and blue images show the GC soft (1.5–2.6 keV), GC medium (2.6–4.5 keV) and GC hard (4.5–8 keV) energy bands, respectively. The same regions displayed in Fig. 7 are evidenced here.

thermal emission than the surrounding regions.[10] We also note that the eastern portion of what appears to be part of the southern lobe has a colour as red as G0.1−0.1 and the superbubble regions (see Fig. 10). Therefore, this emission might not be associated with the lobes, but rather with G0.1−0.1 or the edge of the superbubble (however, a gap such as might be produced by a foreground dust lane, appears to separate the lobes' emission from G0.1−0.1). Figs 7 and 18 also show that the surface brightness of the northern lobe decreases with distance from Sgr A* (Heard & Warwick 2013).

The bottom panel of Fig. 11 shows that the lobes have an orange colour, indicating harder soft X-ray emission compared to the

[10] A hot plasma, with temperatures of ∼2–4 keV, produces intense X-ray emission but weaker soft X-ray lines, compared to a plasma having a temperature around 1 keV.

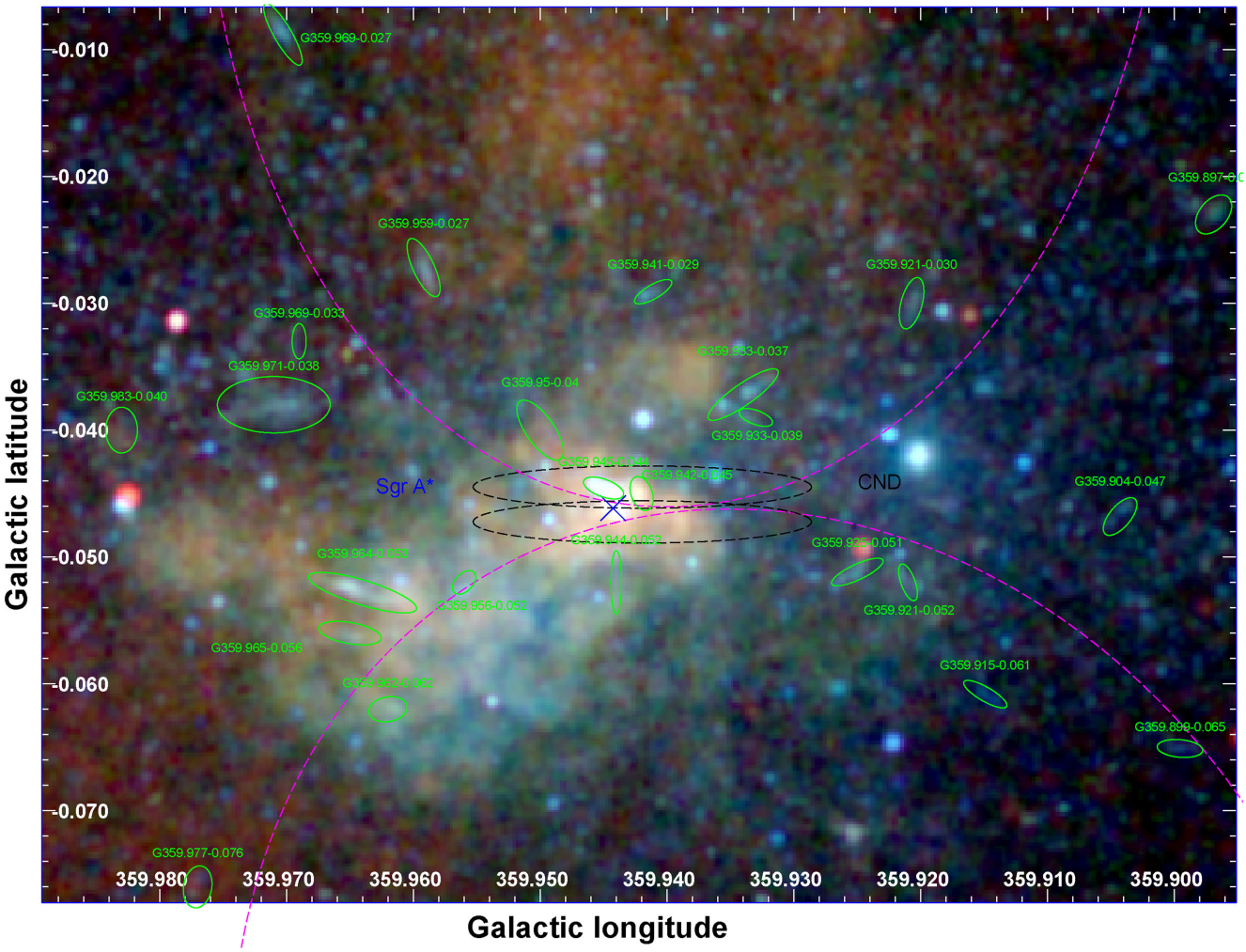

Figure 19. Zoom of the finding chart displayed in Fig. 18.

surrounding regions. In particular, a brighter and harder (yellow–green) linear structure outlines the northern lobe, shaping it to have a well-defined and symmetric spade structure, with a sharp transition at the border. The sharpness of the transition suggests the presence of a limb-brightened shock, indicating that the lobe is a bubble enclosed by a thin shell of hot, compressed material. This claim is strengthened by our analysis of the *Chandra* data (see Figs 18 and 19; Baganoff et al. 2003; Lu et al. 2008; Muno et al. 2008). The superior *Chandra* spatial resolution, in fact, allows us to note that these projected linear features are running right along the lobes' edges, indeed confirming the presence of a shock (Figs 18 and 19). We also note that the emission from the northern half of the lobe seems to be mainly due to three harder filaments converging at the top in a cusp, having radio continuum counterparts (Zhao et al., in preparation) and associated Paschen α emission, indicating that these are thermal features (see Figs 12 and 20).

In the southern lobe, two bright knots are observed in the centre and at the tip. Interestingly these appear to be located approximately at the same distance and in the opposite direction, compared to Sgr A*, as two enhancements present in the northern lobe. Moreover, the two bright knots have a green–yellow colour (upper panel of Fig. 11) similar to their apparent counterparts in the northern lobe. This suggests both (i) a similar physical origin for these features in both the north and south lobes and; (ii) that the process that created the lobes is symmetric about the Galactic plane and its engine is (or is located close to) Sgr A*. The obvious interpretation of this morphology is that energetic events simultaneously ejected diametrically opposed blobs of hot gas.

However, upon closer inspection, the northern and southern lobes do not appear completely symmetric. For example, compared to the northern lobe, the western side of the southern lobe and the region close to Sgr A* appear suppressed (see Figs 7 and 18 and discussion following). On the other hand, the eastern side of the southern lobe appears to extend further (e.g. further east compared to G359.977−0.076) than the corresponding boundary of the northern lobe (located close to e.g. G359.974−0.000). As described before, the emission around and east of G359.977−0.076 has a different colour and might therefore be associated with either the superbubble, with G0.1−0.1, or it could be a feature that is independent of either of these and of the lobes.

The bottom panel of Fig. 8 shows that the region with depressed soft X-ray emission south of Sgr A* and on the western side of the southern lobe spatially coincides with the presence of the 20 km s^{-1} molecular cloud, which is thought to be located in front of Sgr A* (Coil & Ho 2000; Ferrière 2009) and to have a large column density. Soft X-ray emission could be produced there but be completely obscured to us by this intervening cloud (see

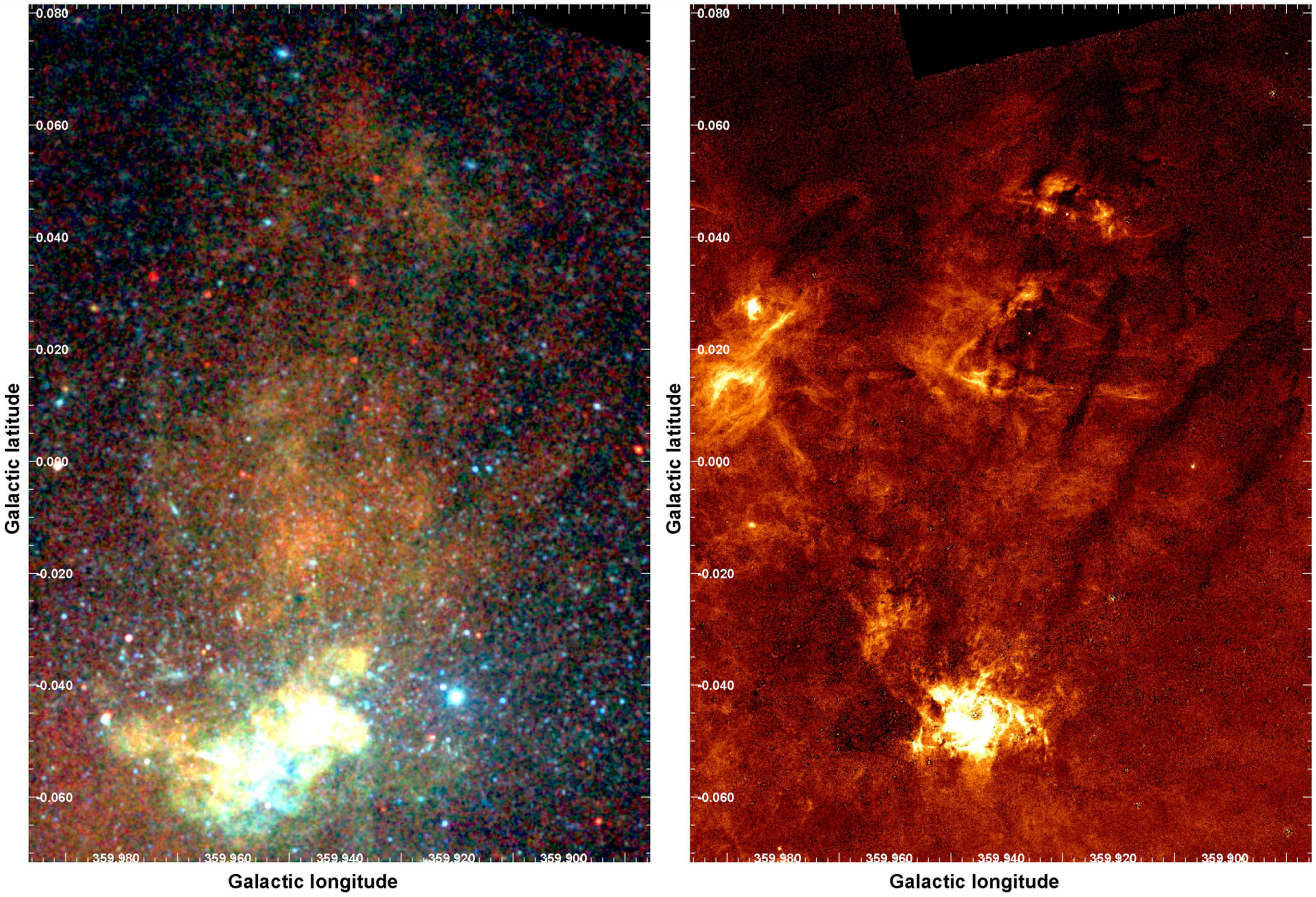

Figure 20. Left-hand panel: *Chandra* RGB image of the northern lobe. See Fig. 18 for more details. Right-hand panel Pa α image of the northern lobe, tracing thermal, ionized gas (from Wang et al. 2010). Continuum emission from stars has been removed (Dong et al. 2011), so the only stars that appear are those that have strong Pa α emission lines. Two Pa α-emitting luminous stars located at $l \sim 359.^{\circ}935$, $b \sim 0.^{\circ}21$ and $l \sim 359.^{\circ}925$, $b \sim 0.^{\circ}45$ (Mauerhan et al. 2010; Dong, Wang & Morris 2012) are probably responsible for at least part of the ionization indicated by the Pa α.

Fig. 2). To reinforce this idea, we note that, in fact, at this position, hard X-ray radiation (between 4.5 and 12 keV) is observed by *Chandra* to have a non-thermal spectrum and to be extended (Morris et al. 2003). Therefore, this hard radiation, which is able to penetrate the cloud, could be produced by strong shocks at the bubble's border. Similar hard non-thermal filaments are observed in several places at the border of the northern lobe (Morris et al. 2003). This strongly suggests that the actual border of the southern lobe is located further west than the images reveal, and that the lobe's soft X-ray emission is obscured there. Therefore, once the effect of absorption by molecular clouds (e.g. the 20 km s^{-1} cloud) is considered, the symmetry between the northern and southern lobes appears more clearly. The linear or filamentary structures (such as G359.974−0.000, G359.970−0.009, G359.959−0.027, G359.945−0.044, G359.942−0.045, 359.933−0.039, see Fig. 18) observed in the northern lobe might be present in the southern one as well, but be suppressed by the intervening absorption. Fig. 20 shows the comparison between the *Chandra* and Pa α emission. The Pa α map clearly show the presence of tendrils of foreground absorbing material, running north–south along the extension of the lobe. Interestingly, the same tendrils are also evident as absorption lanes in the X-ray image. We also note that two Pa α emitting luminous stars are contributing to, if not dominating, the ionization of the gas surrounding them. However, there is a close correspondence between the Pa α emission and the soft X-ray emission at the northern tip of the lobe, so strong shocks might be contributing both to the ionization and to the production of very hot post-shock gas that can emit X-rays. Indeed, we hypothesize that some portion of the hot wind that we see in the softest X-ray bands, presumably emanating from near Sgr A*, is undergoing a shock where it encounters ambient interstellar material at $b \sim 0.^{\circ}02$, and that it is thereby blocked from continuing to higher latitudes. That shock is manifested both as a horizontal feature in the Pa α image, and as a diminution in the brightness of the X-ray emission proceeding north from that latitude. There is still some weaker, extended X-ray emission at higher latitudes, indicating that not all of the outflowing wind is completely blocked. In addition, the portion of the X-ray-emitting plasma lying behind the shock front appears to be absorbed along the shock front, creating a horizontal shadow in the extended X-ray emission, and suggesting that the shock at $b \sim 0.^{\circ}02$ has created a thick, compressed layer that absorbs the X-rays coming from behind it.

8.4.2 Lobes collimated by the circumnuclear disc

Morris et al. (2003) observed that the circumnuclear disc (CND) has a size and orientation that are consistent with it being the agent that collimates an isotropic outflow from the Sgr A* region, thereby

creating the bipolar lobes of hot plasma. Those authors further suggested that the sequence of enhancements along the axis of the lobes might have resulted from a series of energetic mass ejections from the immediate environment of Sgr A⋆. A similar scenario has recently been discussed by Heard & Warwick (2013b). At an outflow velocity of 10^3 km s^{-1}, it would have taken 2–6 $\times$ 10^3 yr to inflate the lobes. Assuming a thermal emission model, an electron density n_e in the range 1–10 cm^{-3} can be inferred (Morris et al. 2003; Heard & Warwick 2013b) and, assuming that the line-of-sight depth is equal to the projected width, the total hot-plasma mass involved in the X-ray lobes is only about 1–3 solar masses.

8.4.3 Energetics of the lobes

Except for the broad intensity enhancements along the axis of the lobes, the surface brightness is relatively smoothly distributed. Assuming a continuous and constant outflow, we examine the energy budget of the lobes. In particular, integrating the measured energy density over a cylinder of 5 pc radius and 12 pc height (the approximate sizes of the lobes), a thermal energy of $E_{th} \sim 9 \times 10^{49}$ erg is estimated.

It has been estimated that the massive stars in the central parsec collectively lose $\sim 5 \times 10^{-3}$ M$_\odot$ yr^{-1} in stellar winds, with velocities ranging from $\sim$300 to 1000 km s^{-1} (Geballe et al. 1987; Najarro et al. 1997; Paumard et al. 2001). The total kinetic energy thermalized by shocks is then $E \sim 5 \times 10^{38}$ erg s^{-1} for such a mass outflow rate and an outflow velocity of 1000 km s^{-1} (Quataert & Loeb 2005). Therefore, the energy released within the time needed to inflate the lobes ($\sim 4 \times 10^3$ yr) is equivalent to $E \sim 5 \times 10^{49}$ erg, therefore giving an important contribution to the generation of the lobes.

The lobes might also be traceable to the accretion flow on to Sgr A⋆. We note that, as estimated by Wang et al. (2013), only $\sim$1 per cent of the matter initially captured at the Bondi radius presently reaches the innermost regions around Sgr A⋆. The rest of the accretion power, estimated to be $\sim 10^{39}$ erg s^{-1} (Wang et al. 2013), is probably converted to kinetic energy and used to drive an outflow that carries away the bulk of the inflow, sculpting the environment with its ram pressure. If so, within the lobe inflation time, a total energy of $\sim 10^{50}$ erg would have been deposited.

Within the CMZ, X-ray reflection nebulae indicate that a few hundred years ago Sgr A⋆ was more active, being $\sim 10^6$ times brighter than at present for approximately 5–10 per cent of the time in the past millennium (experiencing $L_X \sim 10^{39}$ erg s^{-1}; see Ponti et al. 2013 for a review). Could the lobes have been created by similar events that occurred over the past 10^4 yr? The light crossing time of the CMZ limits our capability to trace Sgr A⋆'s past activity beyond about 10^3 yr ago, so it is difficult to directly trace the echoes of possible energetic events on such time-scales. However, if the process has been active over the past (5–10) $\times$ 10^3 yr at roughly the same rate, (therefore active at $L \sim 2 \times 10^{39}$ erg s^{-1} for $\sim 10^3$ yr in the past 10^4 yr), a total integrated energy equal to $\sim 5 \times 10^{49}$ erg should have been generated. If Sgr A⋆'s past activity was characterized by outbursts with associated outflows having kinetic luminosity comparable to the radiated power (therefore much higher than in soft state stellar mass BH; Ponti et al. 2012), then these events could be the primary source (or at least contribute) to form the lobes.

All these processes appear similarly likely to have an impact on the formation of the lobes, from an energetic point of view. However, we note that the first two mechanisms are powered by a quasi-continuous outflow from Sgr A⋆ or from the central stellar cluster. In such scenarios, therefore, the sharpness of the edges at the extremities of the lobes remains rather puzzling, favouring explosive-outbursting scenarios.

8.4.4 Are Sgr A's lobes the SNR of SGR J1745−2900?

The recent discovery of a young magnetar, SGR J1745−2900 (Degenaar et al. 2013; Dwelly & Ponti 2013; Mori et al. 2013), most probably in orbit around Sgr A⋆ (Rea et al. 2013), raises the quest for finding its young SNR. SGR J1745−2900 is estimated to be only about 9 $\times$ 10^3 yr old and to be located at $\lesssim$0.07–2 pc from Sgr A⋆ (Rea et al. 2013). Therefore, the SN that generated SGR J1745−2900 should have exploded near the centroid of the lobes and likely inside the inner radius of the CND. If the shock propagated at the sound speed ($v_s \sim 750$ km s^{-1}), then a present size of $\sim$6.5 pc would be expected. This is slightly smaller than the observed size of the lobes ($\sim$12 pc), but is consistent with the observed size within the uncertainties in the age and the sound speed. We also note that the thermal energy content in the lobes ($E_{th} \sim 9 \times 10^{49}$ erg) is lower, but of comparable order of magnitude, to the energy released by typical SN explosions. It is therefore plausible that the lobes are indeed the SNR associated with SGR J1745−2900.

Another viable possibility is that the lobes have been generated by the SN that created the Pulsar Wind Nebula (PWN) candidate G359.945−0.044, located only $\sim$8 arcsec from Sgr A⋆, with an estimated age of few thousand years (Wang et al. 2006a). It is therefore possible that at least one SN exploded close to Sgr A⋆ within the last $\sim$10 kyr. If so, its blast wave likely propagated into a pre-existing hot, low-density cavity created by Sgr A⋆'s outflows and the collective winds of the central stellar cluster. Given the density and the temperature in the lobes ($kT \sim 2$ keV; Morris et al. 2003), the shock is estimated to reach 15 pc in 9 $\times$ 10^3 yr (Wang, Jiang & Cheng 2005), a value consistent with the observed size of the lobes.

As mentioned above, the presence of the sharp edges to the lobes seems to favour an explosive mechanism for their creation. An SN exploding inside the CND would expand into the pre-existing, stationary outflow from the centre and be collimated in the same way. Hydrodynamical simulations typically show that SN shock fronts are reflected away when encountering the walls of a dense molecular cloud, such as the CND (Ferreira & de Jager 2008). In this scenario the sharp edge of the lobes would be due to the SN shock front. If the SN recurrence time is longer than or comparable to the lobe expansion time (a few thousand years), then this would not appear as a stationary process. Assuming a recurrence time between 1 and 10 $\times$ 10^4 yr (similar to the SN recurrence time of the central young cluster, in which $\sim$100 massive stars presumably becoming SN over an $\sim 10^7$ yr time interval), we estimate a time-averaged kinetic power release of 3–30 $\times$ 10^{38} erg s^{-1}. This indeed suggests that (i) SN explosions of the central star cluster can contribute to powering the lobes; (ii) the lobes are quasi-stationary features; and (iii) it is not unlikely that we observe such features created by a rare event such as an SN explosion.

Finally, we note that, although the characteristics of the X-ray emission from the lobes appear consistent with being the X-ray remnant of a recent SN that exploded within a few parsecs of Sgr A⋆, the lack of associated non-thermal radio emission from such a young SNR is problematical for this hypothesis.

8.5 G359.77−0.09 and G359.79−026: a ring from a hot superbubble south-west of Sgr A*

A series of diffuse, soft features appear to the south-west of Sgr A* (see Fig. 3), namely G359.77−0.09, G359.79−0.26 and a newly recognized extended feature, G0.0−0.16. If these are physically connected, they form, in projection, a roughly elliptical shape whose major axis has an inclination of about 60° with respect to the Galactic plane (see Figs 3, 6, 7, 10, 11, 14 and 16). These features show similar colours and strong, soft line emissions, indicating a similar thermal origin (see Figs 3, 10 and 11). This elliptical structure appears brightest at the softest energies; however, it is not observed below 1.5 keV, suggesting a location near the GC and a low temperature for its plasma, compared to the surrounding emission. We note that this feature is characterized by a very bright edge with strong Si XIII emission on the outside of the ellipse, suggesting a lower temperature of the edge compared to the interior.

The ellipse centre is located at $l \sim 359.^{\circ}9$, $b \sim -0.^{\circ}125$ and it has minor and major axes of about 7.8 and ∼12 arcmin, respectively (corresponding to 18 and 28 pc). Both Mori et al. (2009) and Heard & Warwick (2013) considered that these structures/group of structures were physically connected and form a superbubble candidate. We note that the recognition of such an elliptical ring critically depends on the presence of the dark lane running from $l \sim 0.^{\circ}02$, $b \sim -0.^{\circ}22$ to $l \sim 0.^{\circ}05$, $b \sim -0.^{\circ}07$ (see Figs 3, 7, 10, 11 and 16), which separates G0.0−0.16 from the emission of G0.1−0.1; this dark lane helps define the quasi-continuous elliptical morphology of the ring. However, the lane might simply be due to absorption by foreground material, in which case G0.0−0.16, forming the eastern part of the ring, could simply be connected to G0.1−0.1.

8.5.1 S XV emission filling the superbubble

The S XV emission provides a key piece of information to better understand the superbubble. We note, in fact, that the S XV emission completely fills the region inside the ring with a roughly uniform brightness (several times brighter than in the surrounding region) and sharply drops at the ring's edge. This indicates that the superbubble is a shell of hot gas that we see projected on to the plane of the sky (see the middle top panel of Fig. 14). To further corroborate this, we note that a sharp emissivity drop appears to be located just outside of the ring, running all around the ring's external edge. Such X-ray depression might be produced by a high column density of cold gas pushed away by the superbubble's shock front and accumulated in large quantities just outside the shock. If so, the observed depression could be indicating that the superbubble is located in front of G0.1−0.1. Fig. 7 also shows a small depression in the top part of the northern lobe that could easily be explained by absorption associated with the superbubble if it is located in front of the lobes. This situation would then be somewhat analogous to the colour variation in the south lobe.

Mori et al. (2009) and Heard & Warwick (2013) estimate a total thermal energy contained within the superbubble of $E_{\rm th} \sim 10^{51} f^{1/2}$ erg (where f is the volume filling factor of the emitting plasma). Such a large energy content does, indeed, require multiple SN events. Those authors also estimate for G359.77−0.09 and G359.79−0.26 an ionization time-scale of $t_{\rm ion} \sim 3 \times 10^4$ yr (assuming $f \sim 1$).

8.5.2 Origin

The origin of such a superbubble is not clear. We note that many of the massive stars that are suggested to have escaped from the Quintuplet cluster (Habibi et al. 2013, 2014) are projected inside the superbubble. It is therefore possible that explosions of stars lost by the Quintuplet cluster have contributed to energising the superbubble.

A more speculative point is that the estimated age of the superbubble is of the same order of magnitude as the recurrence time of tidal disruption events by Sgr A*: $t_{\rm TDE} \sim 1$–3×10^4 yr (Alexander & Hopman 2003). While Sgr A* appears, in projection, to be located inside the superbubble, it is ∼6.7 arcmin off from the superbubble's centre. Khokhlov & Melia (1996) suggested that an explosion associated with a tidal disruption event would liberate a large amount of energy on the order of $E \sim 10^{52}$ erg that would propagate as a powerful shock wave into the local interstellar medium. As with the remnant of the SGR J1745−2900, we expect that the shockwaves of a tidal disruption event would interact with the CND. However, the unbound part of the tidally disrupted star would be ejected into a limited solid angle, producing a strongly elongated and asymmetric remnant (Khokhlov & Melia 1996; Ayal, Livio & Piran 2000). Such a remnant would then appear as a very energetic shell of hot gas and remain visible for a time comparable to the age of a typical SNR. Assuming a shock survival time of ~ 1–10×10^4 yr, we could potentially observe a few remnants resulting from tidal disruptions. We suggest that the superbubble G359.77−0.09 has properties that make it a possible candidate. No other feature with properties obviously related to a tidal disruption event appear to be observed close to Sgr A*.

8.6 The arc bubble: a second superbubble in the GC

Highly enhanced soft X-ray emission is observed east of Sgr A* from the region called G0.1−0.1. This feature appears in Figs 10 and 11 as a slightly elliptical feature of enhanced emission with centre at $l \sim 0.^{\circ}09$, $b \sim -0.^{\circ}09$ and with radius of ∼5 arcmin (corresponding to ∼10 pc). The top panel of Fig. 11 shows that G0.1−0.1 and the Radio Arc regions both show distinct red emission. This indicates large equivalent widths of the emission lines from this plasma and therefore a thermal origin. However, the top panel of Fig. 10 and the bottom of Fig. 11 show strong colour gradients within these regions, indicating that they might have different contributions from distinct components.

The PWN candidate G0.13−0.11 ($l = 0.^{\circ}131$, $b = -0.^{\circ}111$; Wang et al. 2002; Heard & Warwick 2013) stands out from the general thermal emission in G0.1−0.1, appearing as a distinct point-like source characterized by a light blue/white colour,[11] indicating its non-thermal origin (dominated by intense soft and hard continuum emission with no soft line emission, see the top panel of Fig. 11).[12] The point-like head of G0.13−0.11 appears to be accompanied by a tail extending to the south for 4.5–5 pc; in Fig. 12, it appears with a white–violet colour.

Heard & Warwick (2013) suggest that the SN that generated G0.13−0.11 might be the source of the soft X-ray emission from this region. Those authors present a spectral study of the X-ray emission from G0.1−0.1 and find a gas temperature of $kT = 1.1 \pm 0.1$ keV, and a column density of $N_{\rm H} = 5.6 \pm 0.5 \times 10^{22}$ cm^{-2}, indicating

[11] Note that in the top panel of Fig. 10 despite an enhancement of diffuse emission from the region surrounding the core of G0.13−0.11, no point like source is detected in the soft X-ray line image.

[12] Please note that an unrelated point source at $l = 0.^{\circ}142$, $b = -0.^{\circ}109$ is located at the same latitude, but ∼1.5 pc to the Galactic east of the PWN candidate G0.13−0.11.

a GC location of this emission, and abundances that are about 1.8 times solar. Assuming that the plasma volume is only 3.5 pc^3, corresponding to only 1.5 arcmin radius around the PWN (see the red circle in Fig. 13), the authors estimated a thermal energy of $E_{th} = 3.1 \times 10^{49}$ erg (and a plasma ionization time-scale of at least $t = 1.8 \times 10^4$ yr), thus consistent with being produced by a single SN explosion.

8.6.1 Energetics of the arc bubble

We note from Figs 3, 7, 10–12, 14 and 16 that G0.1−0.1 extends further from G0.13−0.11 than the 1.5 arcmin region size considered by Heard & Warwick (2013), with no clear boundary at 1.5 arcmin (see Fig. 13). To illustrate this, Fig. 12 shows the soft emission lines RGB image with colour scales chosen to highlight intensity variations present within this region. The left-hand panel of Fig. 13 shows the contours of the S XV emission overlaid on the 20 μm MSX image (Price et al. 2001). Fig. 13 clearly shows that the empty mid-IR bubble (the so-called arc bubble; Levine, Morris & Figer 1999; Rodríguez-Fernández, Martín-Pintado & de Vicente 2001; Simpson et al. 2007) is completely filled with warm X-ray-emitting plasma and that the soft X-ray emission is not confined to within ∼1.5 arcmin of G0.13−0.11, but it extends much further, for about 7 arcmin. Assuming a uniform surface brightness, if the bubble is 4.5 times larger, we would expect a thermal energy of $E_{th} \sim 1.5 \times 10^{51}$ erg, thus most probably requiring multiple SN events, and supporting the notion that G0.1−0.1 is a second superbubble candidate in the GC.

Rodríguez-Fernández et al. (2001) have noticed that the Radio Arc bubble is filled with continuum X-ray emission seen by ASCA which they ascribed to X-ray sources inside the bubble. Here we find that the bubble is in fact filled with diffuse thermal X-rays, most likely originating from SN explosions of massive stars associated with the Quintuplet cluster.

We also note that the soft line emission is at least as extended as the arc bubble and is highly inhomogeneous (see Figs 12 and 13). Three depressions having roughly circular shapes can be discerned in G0.1−0.1 (Fig. 13). Two cavities are located at about the same latitude, with centres close to $l = 0.^\circ057$, $b = -0.^\circ067$ and to $l = 0.^\circ116$, $b = -0.^\circ071$ and with radii of ∼1.6 arcmin (corresponding to ∼3.7 pc) and ∼1 arcmin, respectively. These cavities appear to be surrounded by a thin rim of brighter emission. A third depression is centred at $l = 0.^\circ083$, $b = -0.^\circ123$, with ∼1.8 arcmin radius. This cavity also seems to be confined by a thin shell of brighter material, except for its southern edge, where it appears open (see Fig. 12), possibly because of the presence of a dark absorbing lane.

8.6.2 Association with the Quintuplet cluster?

Despite its offset position from the centre of the mid-IR arc bubble, the Quintuplet cluster is often considered responsible for creating and maintaining the bubble with a combination of SNe and strong stellar winds (e.g. Simpson et al. 2007). Johnson et al. (2009) invoke a possible non-uniformity of the ambient medium as a possible origin of this asymmetry. This might also apply to the X-ray emission. However, we note that the Quintuplet cluster is moving supersonically within the CMZ (Stolte et al. 2014). Given its projected velocity, the cluster would have taken ∼100 kyr to cross the width of the IR arc bubble, in which case the bubble would have been inflated on a time-scale much smaller than typical superbubble formation times (Castor, McCray & Weaver 1975; Weaver et al. 1977; Mac Low & McCray 1988). Several SN explosions in that amount of time would therefore have been required. Furthermore, the Quintuplet cluster would have been located in the middle of the two northern cavities about 4×10^4 and 9×10^4 yr ago, respectively (the right-hand panel of Fig. 13 illustrates the direction of the cluster's motion and the position of the cavities). The relatively small cavities observed in the northern part of G0.1−0.1 are unlikely to have been generated by multiple cluster stars. In fact, an SN exploding in the hot plasma of G0.1−0.1 is expected to undergo a significantly different evolution than a typical SNR. In particular, the sound velocity is significantly larger than in a typical low-pressure medium. Tang & Wang (2005) have shown that the shock velocity follows a Sedov solution but quickly deviates from it when it becomes mildly supersonic. This translates into a much faster evolution and much larger cavities would be expected if the SN exploded 4×10^4 and 9×10^4 yr ago, when the Quintuplet cluster was at that location. It is more likely, therefore, that the two cavities to the Galactic west of the Quintuplet might have been generated by SN explosions of massive stars either stripped from the Quintuplet cluster (Habibi et al. 2013) or having no association with it.

The large thermal energy filling the arc superbubble could have been produced by some combination of winds from the young stars and by multiple SN explosions, including the SN explosion associated with the PWN G0.13−0.11.[13]

8.7 A hot atmosphere around the GC – A link to the GC lobe? And to the *Fermi* bubbles?

8.7.1 General morphology

As observed in all soft X-ray maps (Figs 3, 10 and 11) and confirmed by the soft plasma intensity map (obtained through spectral-image decomposition, Fig. 16), the regions at higher Galactic latitudes are significantly brighter in soft X-rays than the regions closer to the disc, presumably in part because of the smaller extinction at the higher latitudes.

The western border of this enhanced emission is defined by a relatively sharp edge between $l = 359.^\circ63$, $b = 0.^\circ06$ and $l = 359.^\circ55$, $b = 0.^\circ46$ (Fig. 16, see also Figs 10 and 11). The soft X-ray emission peaks above the location of the GC Radio Arc, appearing as a continuation of the Radio Arc itself. Further west the soft X-ray emission appears to fade with increasing Galactic longitude. In particular, the spectral decomposition provides hints for the presence of an eastern edge, fainter but similar to the western edge, of this hot GC atmosphere. However, the presence of an edge to the west is less obvious because of the soft X-ray extinction likely caused by a series of molecular clouds (e.g. the Brick) present at that location and because of the partial high-latitude coverage of this region.

8.7.2 Radiative process

The presence of intense, soft X-ray emission lines (see Figs 10 and 11) and, in particular, the good fit of a spectral decomposition based on a thermally emitting gas (see Fig. 16) indicate that most of the high-latitude emission is generated by a thermal radiative process in a warm plasma. To demonstrate this, we accumulate the EPIC-pn spectrum from a circular region of 8.28 arcmin radius centred at $l = 0.^\circ181$, $b = 0.^\circ359$. The resulting spectrum is

[13] We note that the PWN G0.13−0.11 is located right in the middle of the mid-IR arc bubble.

well fitted with an absorbed thermal emission component (APEC) with $kT = 0.96 \pm 0.1$ keV, $N_{\rm H} = (2.3 \pm 0.2) \times 10^{22}$ cm^{-2} and $A_{\rm apec} = (1.5 \pm 0.4) \times 10^{-2}$ cm^{-5}.

8.7.3 *Eastern edge*

The eastern edge of the high-latitude emission rises from the position of the Radio Arc. This raises the interesting question of whether the soft X-ray emission at the location of the Radio Arc might have two contributions, one associated with the G0.1−0.1 superbubble (filling the mid-IR arc bubble; see Section 8.6), while the second is associated with enhanced soft X-ray emission due to the presence of the Radio Arc and its polarized radio plumes at higher latitudes (Seiradakis et al. 1985; Tsuboi et al. 1986; Yusef-Zadeh & Morris 1988). If that is indeed the case and if the two structures have different X-ray colours (e.g. the superbubble produces lower temperature thermal X-ray lines, while the Radio Arc has a larger continuum to lines ratio), then we should observe variations in the X-ray colour distribution. In particular, we would expect a whiter colour and a green–yellow colour (similar to the one characterizing the lobes of Sgr A) at the location of the Radio Arc region compared to G0.1−0.1, in the top panel of Fig. 10 and in Fig. 11, respectively. This idea is, indeed, in agreement with the colour variations and the evolution of the line intensities observed between the G0.1−0.1 and Radio Arc complexes (Figs 10 and 11).

8.7.4 *Western edge, the Chimney and AFGL5376*

Running almost parallel to the western edge of the high-latitude plasma is another region of enhanced soft X-ray emission, located near the Galactic plane, the so-called Chimney ($l = 359\overset{\circ}{.}45$; Tsuru et al. 2009). The Chimney appears as a column of soft X-ray-emitting plasma extending all the way between the core of Sgr C and the northern limit of the *XMM–Newton* scan ($b \sim 0\overset{\circ}{.}15$; see Figs 8, 10 and 11). Tsuru et al. (2009) suggested that the Chimney is an outflow emanating from the SNR candidate G359.41−0.12. They estimated a thermal energy and dynamical time for G359.41−0.12 and the Chimney of $E_{\rm th} = 5.9 \times 10^{49}$ erg, $t_{\rm dy} = 2.4 \times 10^4$ yr and $E_{\rm th} = 7.6 \times 10^{49}$ erg, $t_{\rm dy} = 4 \times 10^4$ yr, respectively. The energetics and time-scales are consistent with typical GC SNRs and Tsuru et al. (2009) suggested that the very peculiar morphology of the outflow producing the Chimney might be due to a peculiar distribution of molecular clouds that block the plasma expansion in the other directions (Tsuru et al. 2009). We note that the morphology of the Chimney resembles that of the Radio Arc. It originates near the Galactic plane (where dense and massive molecular clouds are located) and extends almost perpendicular to the Galactic plane. Within the gap between the Chimney and the western edge (see Fig. 6), a bright non-thermal radio filament with an X-ray counterpart is observed: G359.54+0.18 – the Ripple filament, with a radio length of $0\overset{\circ}{.}08$ (Lu et al. 2003; Yusef-Zadeh et al. 2005). It is oriented parallel to the edge of the soft X-ray plasma distribution (Bally & Yusef-Zadeh 1989; Yusef-Zadeh, Wardle & Parastaran 1997; Staguhn et al. 1998; Yusef-Zadeh et al. 2004; see also Yamauchi et al. 2014). Similar to the Radio Arc, other X-ray and non-thermal radio filaments are observed at the base of the Chimney. The high concentration of non-thermal filaments indicates the importance of magnetic structures in this region (e.g. Morris 2014).

The bright IR source AFGL5376 is located further to the northwest, along the continuation of the sharp X-ray edge and the Chimney (unfortunately just off the *XMM–Newton* map; see Uchida, Morris & Serabyn 1990; Uchida et al. 1994). It is associated with high-velocity CO emission and defines the most prominent portion of a strong large-scale (∼90 pc) shock front that extends all the way down to Sgr C (Uchida et al. 1994). Because the Chimney appears to be associated with a shock, and because it is spatially coincident with magnetic filaments along its length (Yusef-Zadeh et al. 2004), we suggest that it is not a simple SNR, but is a phenomenon associated with a footpoint of a larger scale structure, the GCL.

8.7.5 *Is the outflow confined inside the GCL? Inside the* Fermi *bubbles?*

The GC is considered a mini-starburst environment, producing intense outflows (Crocker 2012; Yoast-Hull et al. 2014). The warm plasma detected at high latitudes is therefore, most probably, associated with intense star formation and it can be a pervasive atmosphere above the entire CMZ. Even in the absence of another confining force, the gravitational potential (e.g. that of Breitschwerdt, McKenzie & Voelk 1991; Launhardt, Zylka & Mezger 2002) would bind the ∼1 keV plasma (having a sound speed of ∼500 km s^{-1}; Muno et al. 2004) to the Galaxy, but in hydrostatic equilibrium, would allow it to extend to heights of several hundred parsecs. If so, it would require a large average star formation rate and concomitant energy input to generate and maintain it.

However, the detection of edges in its distribution suggests that such plasma might be confined within known structures. As noted by Blanton (2008), the locations of the eastern and western footpoints of the GCL (Law, Brentjens & Novak 2011) correspond to the positions of the Radio Arc and the Chimney, respectively. Indeed, the GCL and its possible magnetic nature might confine the warm plasma observed in soft X-rays. This opens the exciting possibility that the observed high-latitude enhanced X-ray emission from the GC 'atmosphere' is indeed the warm plasma filling the GCL. Based on the spectral fit, we deduce a density of $n_{\rm e} = 0.06$ cm^{-3} inside the GCL. Assuming uniform physical conditions inside the GCL (a cylinder of 45 pc radius and 160 pc height) and extrapolating over the entire GCL, we estimate a mass of $\sim 4 \times 10^3$ M$_\odot$ filling the GCL with a total thermal energy of $\sim 10^{52}$ erg. This value is of the same order of magnitude as the energy required to inflate the GCL as estimated by Law et al. (2011).

Just after the first detection of the GCL, Uchida, Sofue & Shibata (1985) noted its similarity with the lobes in nearby radio galaxies (although smaller in size and strength). The authors interpreted the lobes as created by a magnetodynamic acceleration mechanism where the magnetic twist is produced by the rotation of a contracting disc of gas in the Galactic plane. Under such conditions, the plasma is accelerated into a conical cylinder with a helical velocity field (Uchida et al. 1985). Alternatively, Bland-Hawthorn & Cohen (2003) suggested that the GCL could be produced by a large-scale bipolar Galactic wind, that would be the result of a powerful ($E = 10^{54-55}$ erg) nuclear starburst that took place a few 10^6 yr ago. These authors show that dust is associated with the entire GCL structure and they suggest that the GC (and the centres of many Galaxies) would drive large-scale winds into the halo with a recurrence time of about 10 Myr (Bland-Hawthorn & Cohen 2003). Other, alternative, scenarios for the origin of the GCL involve outflows associated with enhanced activity of Sgr A* (Ponti et al. 2013) or intense star formation (Crocker et al. 2011; Crocker 2012).

It is not excluded that the GCL could be simply one part of an even larger scale feature extending over a physical scale of several kiloparsecs above and below the Galaxy, the so-called *Fermi* bubbles (Su, Slatyer & Finkbeiner 2010). These gamma-ray bubbles,

detected with *Fermi*, are interpreted as produced by highly relativistic particles emitting brightly at GeV energies and beyond and they appear to contain and confine soft X-ray-emitting plasma traced by the *ROSAT* all sky survey, from very large scales down to the Milky Way's centre (Su et al. 2010). However, close to the Galactic plane, the bubbles' edges start to become confused. Whatever their origin might be, the *Fermi* bubbles appear to originate (and be collimated) from the CMZ, within the region that *XMM–Newton* scanned here.

Additional *XMM–Newton* observations at high Galactic latitudes, in particular, inside and at the border of the GCL, covering the AFGL 5376 source and the edges of the base of the *Fermi* bubbles will be needed to measure the extent of this high-latitude emission and to help disentangle the hypotheses for its origin. Furthermore, higher spatial resolution observations (such as provided by *Chandra*) at high latitudes would allow one to pin down what fraction of the extended, high-latitude X-ray emission is associated with faint point sources that are relatively less subject to extinction than sources near the plane.

8.8 Soft X-ray emission from the Sgr D and Sgr E regions

Intense, soft, diffuse X-ray emission is observed from G359.12−0.05, the region around 1E1740.7−2942. A radio SNR (G359.07−0.02) is observed at about the same position (LaRosa et al. 2000). G359.12−0.05 has an emission spectrum typical of an SNR (Nakashima et al. 2010). In particular, the high extinction suggests it is located at the GC. Nakashima et al. (2010) suggest that G359.12−0.05 might be associated with the great annihilator and therefore be the second system (such as SS433 and the radio SNR W 50) where a BH is associated with its SNR.

The core of the Sgr D complex is also observed to show enhanced medium energy emission (see Fig. 3). In radio, an SNR southwest of Sgr D's core and H II regions are clearly observed (Fig. 6; LaRosa et al. 2000). Sawada et al. (2009) analysed X-ray data from the *XMM–Newton* and *Suzaku* satellites and observed soft X-ray emission from two diffuse X-ray sources, DS1 and one associated with the core of Sgr D. They suggest that DS1 is a new SNR at the GC.

8.9 Star formation estimate from counts of SNRs

We observe a total of ∼10–12 SNR candidates in the CMZ (plus ∼5 independent radio SNR; see Table 7) plus two superbubbles, each likely created by many (3–10) SN events. These remnants have typical estimated ages of a few tens of thousands of years and temperatures of $kT \sim 0.4$–1.5 keV. Due to the presence of the two superbubbles requiring multiple SNe and the high absorption towards the GC (such as in the star-forming region Sgr B) that hampers us from observing a potentially larger population of remnants characterized by lower temperatures, the number of SNR observed in the GC is most probably underestimated. However, assuming lifetimes of 10–40 kyr, the observed number of SNR yields a rate, averaged over the past several thousands of years, of $r_{\rm SN} \sim 3.5$–15×10^{-4} yr^{-1}, consistent with other estimates (Crocker 2012). This implies a kinetic energy input higher than 1.1×10^{40} erg s^{-1}. To estimate the star formation rate, we assume that all stars with masses greater than 8 M$_\odot$ produce SNe and that all SNR are observable. Therefore, we multiply the SN rate by the integral of the initial mass function (IMF) over all masses divided by the integral of the IMF above 8 M$_\odot$. To reflect the GC IMF, we assume the Kroupa (2002) formulation. The star formation rate then results to be: $r_{\rm SFR} \sim 0.035$–0.15 M$_\odot$ yr^{-1}. If the IMF in the CMZ is top heavy, as some have argued, then a smaller star formation rate is implied.

As noted also by Mori et al. (2008, 2009) and Heard & Warwick (2013), we observe that the two superbubbles have far hotter temperatures (higher density and smaller size) than all the ones observed in the Galactic plane or in the Large Magellanic Cloud (typically with temperatures $kT \sim 0.1$–0.3 keV, densities $n_{\rm e} \sim 0.01$–0.03 cm^{-2}, sizes $l \sim 140$–450 pc; but see also Sasaki et al. 2011; Kavanagh, Sasaki & Points 2012). This could simply be the consequence of the high extinction towards the GC, hiding a population of normal and very soft superbubbles, or it could be a characteristic feature of GC superbubbles, inducing a different evolution because of the interaction with the peculiar GC environment. Further investigation is required to solve this problem.

9 CONCLUSIONS

We have systematically analysed more than 100 *XMM–Newton* observations pointed within 1° of Sgr A* and have created the deepest, few arcsec resolution, X-ray images of the CMZ. This includes a total of about 1.5 Ms of EPIC-pn cleaned exposure in the central 15 arcmin and about 200 ks at all other points of the CMZ. We present here, for the first time, not only broad-band X-ray continuum maps, but also mosaicked maps of both soft line intensities and interline emission from the entire CMZ region.

(i) The remarkably similar distributions of both the soft line emitting plasma (Si XIII, S XV, Ar XVII and Ca XIX) and the soft continuum (intraline bands) indicate that most of the diffuse soft X-ray emission arises from a thermal process generating both continuum and lines.

(ii) Starting from the mosaic maps of the different narrow energy bands and assuming the GC emission is produced by three different components, we fit the maps at different energies and derive the integrated intensity map of the thermal plasma emission. Integrating over the entire CMZ, the total observed (unabsorbed) flux is: $F_{2-4.5\,\rm keV} = 4.2 \times 10^{-11}$ erg cm^{-2} s^{-1}, $F_{4.5-12\,\rm keV} = 1.2 \times 10^{-10}$ erg cm^{-2} s^{-1}, corresponding to a luminosity of $L_{2-12} = 3.4 \times 10^{36}$ erg s^{-1} at an assumed 8 kpc distance.

(iii) Counting the number of SNRs in the CMZ, we estimate an SN rate between $r_{\rm SN} \sim 3.5 - 15 \times 10^{-4}$ yr^{-1}, consistent with other estimates (Crocker 2012), that corresponds to a star formation rate of $r_{\rm SFR} \sim 0.035$–0.15 M$_\odot$ yr^{-1} over the past several thousand years. This implies a kinetic energy input greater than 1.5×10^{40} erg s^{-1}.

(iv) We report the discovery of a new X-ray filament XMM J0.173−0.413 perpendicular to the Galactic plane and south of the GC Radio Arc spatially corresponding to a non-thermal radio filament. XMM J0.173−0.413 is the first of the four cases known where the X-ray emission is not at or near a location where the radio filaments show unusually strong curvature.

(v) The soft GC X-ray emission is absorbed not only by high-column-density foreground clouds located in the Galactic disc, but also by some clouds located on the near side of the CMZ, such as the core and envelope of Sgr B2, M0.25+0.01 (the 'Brick'), and even a few clouds at higher Galactic latitudes, M0.18+0.126 and M0.20−0.48. However, the majority of the observed variations in the soft X-ray emission are true emissivity modulations and not a product of absorption.

(vi) Several SNR candidates are identified by their soft X-ray emission that appears to fill holes in the column density distribution of gas-and-dust derived from sub-millimetre maps.

(vii) Our data shed new light on two quasi-symmetric lobes situated to Galactic north and south of Sgr A⋆. The northern lobe shows a bright and sharp transition at its edge, suggesting the presence of a shock. Such features are possibly the remnant of the SN that generated SGR J1745−2900 or the PWN candidate G359.945−0.044. Alternatively, the lobes might constitute a long-lived bipolar structure produced by an isotropic outflow produced by either (1) the cumulative winds from the young stars of the central cluster, (2) a wind associated with the accretion flow on to Sgr A⋆ or (3) the same process that generated the X-ray reflection nebulae (if such activity has been recurrent over the past millennia).

(viii) The uniform X-ray colour of the superbubble G359.9−0.125, its sharp external edge and its being filled with S XV emitting plasma suggest that the soft X-ray features south-west of Sgr A⋆ form a unique shell-like structure with total energy $E_{\rm th} \sim 10^{51}$ erg, therefore making it a superbubble candidate in the GC (high absorption indicates that G359.9−0.125 is located at the GC). Alternatively, it might be the remnant of a very energetic event at the GC, such as a tidal disruption event.

(ix) We discover new evidence for the GC superbubble G0.1−0.1, also known as the arc bubble from mid-IR observations: its soft X-ray (e.g. S XV) emission completely fills the mid-IR bubble, and indicates a thermal energy as large as $E_{\rm th} \sim 1.5 \times 10^{51}$ erg. At present the Quintuplet cluster, which is moving at very high speed through the CMZ, is located at the border of the superbubble. However, it was more centrally located a few 10^4 yr ago and it could have, at least in part, energized it. We do not observe similar soft X-ray emission trailing the Arches cluster, but this might be ascribed to its younger age.

(x) We suggest that the GCL might be a magnetic structure filled with warm, soft, X-ray-emitting plasma. In fact, we observe: (i) enhanced soft X-ray emission at high Galactic latitudes; (ii) enhanced soft X-ray emission at, and between, the longitudes of the Radio Arc and the Chimney associated with Sgr C, corresponding to the east and west foot-points of the GCL; (iii) a sharp edge (at $l = 359.^{\circ}63$, $b = 0.^{\circ}06$ and $l = 359.^{\circ}55$, $b = 0.^{\circ}46$), running parallel to the non-thermal ripple filament (G359.54+0.18) and Sgr C thread, defining the western border of the enhanced soft X-ray emission. The GCL could be the relatively small base of an even larger structure, the so-called *Fermi* Bubbles. Additional observations will be needed to clarify this.

(xi) A new very faint X-ray transient, XMMU J17450.3−291445, has been discovered during the new *XMM–Newton* campaign to reach a peak luminosity of $L_{\rm X} \sim 10^{35}$ erg s^{-1} for ∼2 h (Soldi et al. 2014).

ACKNOWLEDGEMENTS

This research has made use both of data obtained with *XMM–Newton*, an ESA science mission with instruments and contributions directly funded by ESA Member States and NASA, and data obtained from the Chandra Data Archive. We kindly acknowledge Sergio Molinari for providing the Herschel map, Casey Law for the GBT images and Namir Kassim for the VLA 90-cm map. GP acknowledges Roland Crocker, Barbara De Marco and Pierre Maggi for useful discussions. MC, AG, RT, SS acknowledge support from CNES. GP also acknowledges Frederick Baganoff and Nanda Rea for discussions about the origin of the lobes and the association with the SNR of SGR J1745−2900. We thank the referee for a careful reading of the paper. GP acknowledges support via an EU Marie Curie Intra-European Fellowship under contract no. FP7-PEOPLE-2012-IEF-331095. The GC *XMM–Newton* monitoring project is partially supported by the Bundesministerium für Wirtschaft und Technologie/Deutsches Zentrum für Luft- und Raumfahrt (BMWI/DLR, FKZ 50 OR 1408) and the Max Planck Society. Partial support through the COST action MP0905 Black Holes in a Violent Universe is acknowledged. We thank the ISSI in Bern.

REFERENCES

Aharonian F. et al., 2005, A&A, 432, L25
Alexander T., Hopman C., 2003, ApJ, 590, L29
Amo-Baladrón M. A., Martín-Pintado J., Morris M. R., Muno M. P., Rodríguez-Fernández N. J., 2009, ApJ, 694, 943
Anantharamaiah K. R., Pedlar A., Ekers R. D., Goss W. M., 1991, MNRAS, 249, 262
Ayal S., Livio M., Piran T., 2000, ApJ, 545, 772
Baganoff F. K. et al., 2001, Nature, 413, 45
Baganoff F. K. et al., 2003, ApJ, 591, 891
Bally J., Yusef-Zadeh F., 1989, ApJ, 336, 173
Bamba A., Yokogawa J., Sakano M., Koyama K., 2000, PASJ, 52, 259
Bamba A., Murakami H., Senda A., Takagi S.-i., Yokogawa J., Koyama K., 2002, preprint (arXiv:astro-ph/0202010)
Bamba A., Yamazaki R., Kohri K., Matsumoto H., Wagner S., Pühlhofer G., Kosack K., 2009, ApJ, 691, 1854
Barrière N. M. et al., 2014, ApJ, 786, 46
Bélanger G. et al., 2005, ApJ, 635, 1095
Bélanger G. et al., 2006, ApJ, 636, 275
Bland-Hawthorn J., Cohen M., 2003, ApJ, 582, 246
Blanton M. C., 2008, PhD thesis
Borkowski K. J., Reynolds S. P., Hwang U., Green D. A., Petre R., Krishnamurthy K., Willett R., 2013, ApJ, 771, LL9
Breitschwerdt D., McKenzie J. F., Voelk H. J., 1991, A&A, 245, 79
Capelli R., Warwick R. S., Porquet D., Gillessen S., Predehl P., 2011, A&A, 530, A38
Capelli R., Warwick R. S., Porquet D., Gillessen S., Predehl P., 2012, A&A, 545, A35
Cash W., 1979, ApJ, 228, 939
Castor J., McCray R., Weaver R., 1975, ApJ, 200, L107
Castro M., Maiolino T., D'Amico F., Wilms J., Pottschmidt K., Braga J., 2013, preprint (arXiv:1302.6213)
Chuss D. T., Davidson J. A., Dotson J. L., Dowell C. D., Hildebrand R. H., Novak G., Vaillancourt J. E., 2003, ApJ, 599, 1116
Clark P. C., Glover S. C. O., Ragan S. E., Shetty R., Klessen R. S., 2013, ApJ, 768, L34
Clavel M., Terrier R., Goldwurm A., Morris M. R., Ponti G., Soldi S., Trap G., 2013, A&A, 558, A32
Clavel M., Soldi S., Terrier R., Tatischeff V., Maurin G., Ponti G., Goldwurm A., Decourchelle A., 2014, MNRAS, 443, L129
Coil A. L., Ho P. T. P., 2000, ApJ, 533, 245
Cotera A. S., Erickson E. F., Colgan S. W. J., Simpson J. P., Allen D. A., Burton M. G., 1996, ApJ, 461, 750
Coti-Zelati F. et al., 2015, MNRAS, 449, 2685
Crocker R. M., 2012, MNRAS, 423, 3512
Crocker R. M., Aharonian F., 2011, Phys. Rev. Lett., 106, 101102
Crocker R. M., Jones D. I., Melia F., Ott J., Protheroe R. J., 2010, Nature, 463, 65
Degenaar N., Wijnands R., 2010, A&A, 524, A69
Degenaar N., Wijnands R., Cackett E. M., Homan J., in't Zand J. J. M., Kuulkers E., Maccarone T. J., van der Klis M., 2012, A&A, 545, A49
Degenaar N., Reynolds M. T., Miller J. M., Kennea J. A., Wijnands R., 2013, Astron. Telegram, 5006, 1
Del Santo M., Sidoli L., Bazzano A., Cocchi M., De Cesare G., Paizis A., Ubertini P., 2006, A&A, 456, 1105
Do T., Lu J. R., Ghez A. M., Morris M. R., Yelda S., Martinez G. D., Wright S. A., Matthews K., 2013, ApJ, 764, 154
Dong H. et al., 2011, MNRAS, 417, 114

Dong H., Wang Q. D., Morris M. R., 2012, MNRAS, 425, 884
Downes D., Maxwell A., 1966, ApJ, 146, 653
Dubner G., Giacani E., Decourchelle A., 2008, A&A, 487, 1033
Dutra C. M., Bica E., 2000, A&A, 359, L9
Dutra C. M., Ortolani S., Bica E., Barbuy B., Zoccali M., Momany Y., 2003, A&A, 408, 127
Dwelly T., Ponti G., 2013, Astron. Telegram, 5008, 1
Ebisawa K., Maeda Y., Kaneda H., Yamauchi S., 2001, Science, 293, 1633
Ferreira S. E. S., de Jager O. C., 2008, A&A, 478, 17
Ferrière K., 2009, A&A, 505, 1183
Figer D. F., Kim S. S., Morris M., Serabyn E., Rich R. M., McLean I. S., 1999, ApJ, 525, 750
Freyberg M. J. et al., 2004, Proc. SPIE, 5165, 112
Fukuoka R., Koyama K., Ryu S. G., Tsuru T. G., 2009, PASJ, 61, 593
Gaensler B. M., Pivovaroff M. J., Garmire G. P., 2001, ApJ, 556, L107
Gaensler B. M., van der Swaluw E., Camilo F., Kaspi V. M., Baganoff F. K., Yusef-Zadeh F., Manchester R. N., 2004, ApJ, 616, 383
Geballe T. R., Wade R., Krisciunas K., Gatley I., Bird M. C., 1987, ApJ, 320, 562
Genzel R., Eisenhauer F., Gillessen S., 2010, Rev. Mod. Phys., 82, 3121
Goldwurm A., Brion E., Goldoni P., Ferrando P., Daigne F., Decourchelle A., Warwick R. S., Predehl P., 2003, ApJ, 584, 751
Gray A. D., 1994, MNRAS, 270, 835
Green D. A., 2014, Bull. Astron. Soc. India, 42, 47
Haberl F. et al., 2012, A&A, 545, A128
Habibi M., Stolte A., Brandner W., Hußmann B., Motohara K., 2013, A&A, 556, A26
Habibi M., Stolte A., Harfst S., 2014, A&A, 566, A6
Hales C. A., Gaensler B. M., Chatterjee S., van der Swaluw E., Camilo F., 2009, ApJ, 706, 1316
Harrison F. A. et al., 2013, ApJ, 770, 103
Heard V., Warwick R. S., 2013a, MNRAS, 428, 3462
Heard V., Warwick R. S., 2013b, MNRAS, 434, 1339
Heinke C. O., Tomsick J. A., Yusef-Zadeh F., Grindlay J. E., 2009, ApJ, 701, 1627
Henze M. et al., 2014, A&A, 563, A2
Hewitt J. W., Yusef-Zadeh F., Wardle M., 2008, ApJ, 683, 189
Ho P. T. P., Jackson J. M., Barrett A. H., Armstrong J. T., 1985, ApJ, 288, 575
Inui T., Koyama K., Matsumoto H., Tsuru T. G., 2009, PASJ, 61, 241
Jansen F. et al., 2001, A&A, 365, L1
Johnson J. L., Greif T. H., Bromm V., Klessen R. S., Ippolito J., 2009, MNRAS, 399, 37
Kaneda H., Makishima K., Yamauchi S., Koyama K., Matsuzaki K., Yamasaki N. Y., 1997, ApJ, 491, 638
Kaspi V. M. et al., 2014, ApJ, 786, 84
Kassim N. E., Frail D. A., 1996, MNRAS, 283, L51
Kavanagh P. J., Sasaki M., Points S. D., 2012, A&A, 547, A19
Khokhlov A., Melia F., 1996, ApJ, 457, L61
Koch E. W. et al., 2014, MNRAS, 442, 372
Koyama K., Maeda Y., Sonobe T., Takeshima T., Tanaka Y., Yamauchi S., 1996, PASJ, 48, 249
Koyama K. et al., 2007a, PASJ, 59, 221
Koyama K. et al., 2007b, PASJ, 59, 245
Koyama K., Inui T., Matsumoto H., Tsuru T. G., 2008, PASJ, 60, 201
Koyama K., Takikawa Y., Hyodo Y., Inui T., Nobukawa M., Matsumoto H., Tsuru T. G., 2009, PASJ, 61, 255
Krivonos R. A. et al., 2014, ApJ, 781, 107
Kroupa P., 2002, Science, 295, 82
Kuntz K. D., Snowden S. L., 2008, A&A, 478, 575
Kuulkers E. et al., 2007, A&A, 466, 595
Lakićević M. et al., 2015, ApJ, 799, 50
Lang C. C., Morris M., Echevarria L., 1999, ApJ, 526, 727
Lang C. C., Goss W. M., Morris M., 2002, AJ, 124, 2677
LaRosa T. N., Kassim N. E., Lazio T. J. W., Hyman S. D., 2000, AJ, 119, 207
Launhardt R., Zylka R., Mezger P. G., 2002, A&A, 384, 112
Law C., Yusef-Zadeh F., 2004, ApJ, 611, 858
Law C. J., Backer D., Yusef-Zadeh F., Maddalena R., 2009, ApJ, 695, 1070
Law C. J., Brentjens M. A., Novak G., 2011, ApJ, 731, 36
Levine D., Morris M., Figer D., 1999, in Cox P., Kessler M. F., eds, ESA SP-427: The Universe as Seen by ISO. ESA, Noordwijk, p. 699
Lu F. J., Wang Q. D., Lang C. C., 2003, AJ, 126, 319
Lu F. J., Yuan T. T., Lou Y.-Q., 2008, ApJ, 673, 915
Lu J. R., Do T., Ghez A. M., Morris M. R., Yelda S., Matthews K., 2013, ApJ, 764, 155
Mac Low M.-M., McCray R., 1988, ApJ, 324, 776
Maeda Y. et al., 2002, ApJ, 570, 671
Markoff S., 2010, Proc. Natl. Acad. Sci., 107, 7196
Marquez-Lugo R. A., Phillips J. P., 2010, MNRAS, 407, 94
Mauerhan J. C., Muno M. P., Morris M. R., Stolovy S. R., Cotera A., 2010, ApJ, 710, 706
Maggi P. et al., 2012, A&A, 546, A109
Mereghetti S., Sidoli L., Israel G. L., 1998, A&A, 331, L77
Misanovic Z., Pietsch W., Haberl F., Ehle M., Hatzidimitriou D., Trinchieri G., 2006, A&A, 448, 1247
Molaro M., Khatri R., Sunyaev R. A., 2014, A&A, 564, A107
Molinari S. et al., 2011, ApJ, 735, L33
Mori H., Maeda Y., Pavlov G. G., Sakano M., Tsuboi Y., 2005, Adv. Space Res., 35, 1137
Mori H., Tsuru T. G., Hyodo Y., Koyama K., Senda A., 2008, PASJ, 60, 183
Mori H., Hyodo Y., Tsuru T. G., Nobukawa M., Koyama K., 2009, PASJ, 61, 687
Mori K. et al., 2013, ApJ, 770, L23
Morris M., 1990, in Beck R., Kronberg P. P., Wielebinski R., eds, Proc. IAU Symp. 140, Galactic and Intergalactic Magnetic Fields. Kluwer, Dordrecht, p. 361
Morris M. R., 2014, preprint (arXiv:1406.7859)
Morris M., Serabyn E., 1996, ARA&A, 34, 645
Morris M., Yusef-Zadeh F., 1985, AJ, 90, 2511
Morris M. et al., 2003, Astron. Nachr. Suppl., 324, 167
Morris M., Howard C., Muno M., Baganoff F. K., Park S., Feigelson E., Garmire G., Brandt N., 2004, Proc 4th Cologne-Bonn-Zermatt Symp. Vol. 91, The Dense Interstellar Medium in Galaxies. Springer, Berlin, p. 281
Morris M. R., Meyer L., Ghez A. M., 2012, Research in Astronomy and Astrophysics, 12, 995
Morris M. R., Zhao J.-H., Goss W. M., 2014, in Sjouwerman L., Lang C., Ott J., eds, Proc. IAU Symp. 303, The Galactic Center: Feeding and Feedback in a Normal Galactic Nucleus. Cambridge Univ. Press, Cambridge, p. 369
Muno M. P. et al., 2003, ApJ, 589, 225
Muno M. P. et al., 2004, ApJ, 613, 326
Muno M. P., Pfahl E., Baganoff F. K., Brandt W. N., Ghez A., Lu J., Morris M. R., 2005a, ApJ, 622, L113
Muno M. P., Lu J. R., Baganoff F. K., Brandt W. N., Garmire G. P., Ghez A. M., Hornstein S. D., Morris M. R., 2005b, ApJ, 633, 228
Muno M. P., Bauer F. E., Bandyopadhyay R. M., Wang Q. D., 2006, ApJS, 165, 173
Muno M. P., Baganoff F. K., Brandt W. N., Park S., Morris M. R., 2007, ApJ, 656, L69
Muno M. P., Baganoff F. K., Brandt W. N., Morris M. R., Starck J.-L., 2008, ApJ, 673, 251
Muno M. P. et al., 2009, ApJS, 181, 110
Murakami H., 2002, PhD thesis, Kyoto Univ.
Najarro F., Krabbe A., Genzel R., Lutz D., Kudritzki R. P., Hillier D. J., 1997, A&A, 325, 700
Nakashima S., Nobukawa M., Tsuru T. G., Koyama K., Uchiyama H., 2010, PASJ, 62, 971
Natalucci L., Bazzano A., Cocchi M., Ubertini P., Cornelisse R., Heise J., in 't Zand J. J. M., 2004, A&A, 416, 699
Natalucci L. et al., 2014, ApJ, 780, 63
Neilsen J. et al., 2013, ApJ, 774, 42
Nishiyama S. et al., 2009, ApJ, 690, 1648

Nishiyama S. et al., 2013, ApJ, 769, L28
Nobukawa M. et al., 2008, PASJ, 60, 191
Nobukawa M., Sawada M., Matsumoto H., Tsuru T. G., Koyama K., 2009, Adv. Space Res., 43, 1045
Nobukawa M., Koyama K., Tsuru T. G., Ryu S. G., Tatischeff V., 2010, PASJ, 62, 423
Nobukawa M., Ryu S. G., Tsuru T. G., Koyama K., 2011, ApJ, 739, L52
Nord M. E., Lazio T. J. W., Kassim N. E., Hyman S. D., LaRosa T. N., Brogan C. L., Duric N., 2004, AJ, 128, 1646
Novak G. et al., 2003, ApJ, 583, L83
Nynka M. et al., 2014, ApJ, 789, 72
Ohnishi T., Koyama K., Tsuru T. G., Masai K., Yamaguchi H., Ozawa M., 2011, PASJ, 63, 527
Ostriker J. P., McKee C. F., 1988, Rev. Mod. Phys., 60, 1
Paizis A. et al., 2009, PASJ, 61, 107
Park S., Muno M. P., Baganoff F. K., Maeda Y., Morris M., Howard C., Bautz M. W., Garmire G. P., 2004, ApJ, 603, 548
Park S. et al., 2005, ApJ, 631, 964
Paumard T., Maillard J. P., Morris M., Rigaut F., 2001, A&A, 366, 466
Pavlinsky M. N., Grebenev S. A., Sunyaev R. A., 1994, ApJ, 425, 110
Pedlar A., Anantharamaiah K. R., Ekers R. D., Goss W. M., van Gorkom J. H., Schwarz U. J., Zhao J.-H., 1989, ApJ, 342, 769
Phillips J. P., Marquez-Lugo R. A., 2010, MNRAS, 409, 701
Pierce-Price D. et al., 2000, ApJ, 545, L121
Piraino S. et al., 2012, A&A, 542, L27
Ponti G., Terrier R., Goldwurm A., Belanger G., Trap G., 2010, ApJ, 714, 732
Ponti G., Fender R. P., Begelman M. C., Dunn R. J. H., Neilsen J., Coriat M., 2012, MNRAS, 422, L11
Ponti G., Morris M. R., Terrier R., Goldwurm A., 2013, in Torres D. F., Reimer O., eds, Astrophys. Space Sci. Proc. Vol. 34, Cosmic Rays in Star-Forming Environments. Springer-Verlag, Berlin, p. 331
Ponti G. et al., 2014, in Sjouwerman L., Lang C., Ott J., eds, Proc. IAU Symp. 303, The Galactic Center: Feeding and Feedback in a Normal Galactic Nucleus. Cambridge Univ. Press, Cambridge, p. 333
Ponti G. et al., 2015, MNRAS, 446, 1536
Porquet D., Decourchelle A., Warwick R. S., 2003a, A&A, 401, 197
Porquet D., Rodriguez J., Corbel S., Goldoni P., Warwick R. S., Goldwurm A., Decourchelle A., 2003b, A&A, 406, 299
Porquet D., Grosso N., Burwitz V., Andronov I. L., Aschenbach B., Predehl P., Warwick R. S., 2005a, A&A, 430, L9
Porquet D., Grosso N., Bélanger G., Goldwurm A., Yusef-Zadeh F., Warwick R. S., Predehl P., 2005b, A&A, 443, 571
Porquet D. et al., 2008, A&A, 488, 549
Predehl P., Kulkarni S. R., 1995, A&A, 294, L29
Price S. D., Egan M. P., Carey S. J., Mizuno D. R., Kuchar T. A., 2001, AJ, 121, 2819
Quataert E., Loeb A., 2005, ApJ, 635, L45
Rea N. et al., 2013, ApJ, 775, L34
Reich W., Fuerst E., 1984, A&AS, 57, 165
Reid M. J., 1993, ARA&A, 31, 345
Reid M. J., Menten K. M., Zheng X. W., Brunthaler A., Xu Y., 2009, ApJ, 705, 1548
Renaud M., Paron S., Terrier R., Lebrun F., Dubner G., Giacani E., Bykov A. M., 2006, ApJ, 638, 220
Revnivtsev M. G. et al., 2004, A&A, 425, L49
Revnivtsev M., Sazonov S., Churazov E., Forman W., Vikhlinin A., Sunyaev R., 2009, Nature, 458, 1142
Reynolds M. T., Miller J. M., 2010, ApJ, 716, 1431
Rodríguez-Fernández N. J., Martín-Pintado J., de Vicente P., 2001, A&A, 377, 631
Roy S., Bhatnagar S., 2006, J. Phys.: Conf. Ser., 54, 152
Ryu S. G., Koyama K., Nobukawa M., Fukuoka R., Tsuru T. G., 2009, PASJ, 61, 751
Ryu S. G., Nobukawa M., Nakashima S., Tsuru T. G., Koyama K., Uchiyama H., 2013, PASJ, 65, 33
Sakano M., Koyama K., Murakami H., Maeda Y., Yamauchi S., 2002, ApJS, 138, 19
Sakano M., Warwick R. S., Decourchelle A., Predehl P., 2003a, MNRAS, 340, 747
Sakano M., Warwick R. S., Decourchelle A., 2003b, Workshop on Galaxies and Clusters of Galaxies, 9
Sakano M., Warwick R. S., Hands A., Decourchelle A., 2004, Mem. Soc. Astron. Ital., 75, 498
Sakano M., Warwick R. S., Decourchelle A., Wang Q. D., 2005, MNRAS, 357, 1211
Sasaki M., Breitschwerdt D., Baumgartner V., Haberl F., 2011, A&A, 528, A136
Sawada M., Tsujimoto M., Koyama K., Law C. J., Tsuru T. G., Hyodo Y., 2009, PASJ, 61, 209
Seiradakis J. H., Lasenby A. N., Yusef-Zadeh F., Wielebinski R., Klein U., 1985, Nature, 317, 697
Senda A., Murakami H., Koyama K., 2002, ApJ, 565, 1017
Senda A., Murakami H., Koyama K., 2003, Astron. Nachr. Suppl., 324, 151
Shibata K., Tajima T., Steinolfson R. S., Matsumoto R., 1989, ApJ, 345, 584
Simpson J. P., Colgan S. W. J., Cotera A. S., Erickson E. F., Hollenbach D. J., Kaufman M. J., Rubin R. H., 2007, ApJ, 670, 1115
Skinner G. K., Foster A. J., Willmore A. P., Eyles C. J., 1990, MNRAS, 243, 72
Sofue Y., Handa T., 1984, Nature, 310, 568
Soldi S. et al., 2006, Astron. Telegram, 885, 1
Soldi S. et al., 2014, in Sjouwerman L., Lang C., Ott J., eds, Proc. IAU Symp. 303, The Galactic Center: Feeding and Feedback in a Normal Galactic Nucleus. Cambridge Univ. Press, Cambridge, p. 126
Staguhn J., Stutzki J., Uchida K. I., Yusef-Zadeh F., 1998, A&A, 336, 290
Stiele H., Pietsch W., Haberl F., Hatzidimitriou D., Barnard R., Williams B. F., Kong A. K. H., Kolb U., 2011, A&A, 534, A55
Stolte A. et al., 2014, ApJ, 789, 115
Strüder L. et al., 2001, A&A, 365, L18
Sturm R. et al., 2013, A&A, 558, A3
Su M., Slatyer T. R., Finkbeiner D. P., 2010, ApJ, 724, 1044
Sunyaev R. A., Markevitch M., Pavlinsky M., 1993, ApJ, 407, 606
Tanaka Y., 2002, A&A, 382, 1052
Tanaka Y., Koyama K., Maeda Y., Sonobe T., 2000, PASJ, 52, L25
Tanaka K., Kamegai K., Nagai M., Oka T., 2007, PASJ, 59, 323
Tanaka K., Oka T., Nagai M., Kamegai K., 2009, PASJ, 61, 461
Tang S., Wang Q. D., 2005, ApJ, 628, 205
Tatischeff V., Decourchelle A., Maurin G., 2012, A&A, 546, A88
Terrier R. et al., 2010, ApJ, 719, 143
Trap G. et al., 2009, A&A, 504, 501
Trap G. et al., 2011, A&A, 528, A140
Tsuboi M., Inoue M., Handa T., Tabara H., Kato T., Sofue Y., Kaifu N., 1986, AJ, 92, 818
Tsuru T. G., Nobukawa M., Nakajima H., Matsumoto H., Koyama K., Yamauchi S., 2009, PASJ, 61, 219
Tüllmann R. et al., 2011, ApJS, 193, 31
Turner M. J. L. et al., 2001, A&A, 365, L27
Uchida Y., Sofue Y., Shibata K., 1985, Nature, 317, 699
Uchida K., Morris M., Serabyn E., 1990, ApJ, 351, 443
Uchida K., Morris M., Yusef-Zadeh F., 1992, AJ, 104, 1533
Uchida K. I., Morris M. R., Serabyn E., Bally J., 1994, ApJ, 421, 505
Uchiyama H., Nobukawa M., Tsuru T., Koyama K., Matsumoto H., 2011, PASJ, 63, 903
Uchiyama H., Nobukawa M., Tsuru T. G., Koyama K., 2013, PASJ, 65, 19
Wang D. X., Xiao K., Lei W. H., 2002a, MNRAS, 335, 655
Wang Q. D., Gotthelf E. V., Lang C. C., 2002b, Nature, 415, 148
Wang Q. D., Lu F., Lang C. C., 2002c, ApJ, 581, 1148
Wang W., Jiang Z. J., Cheng K. S., 2005, MNRAS, 358, 263
Wang Q. D., Lu F. J., Gotthelf E. V., 2006a, MNRAS, 367, 937
Wang Q. D., Dong H., Lang C., 2006b, MNRAS, 371, 38
Wang Q. D. et al., 2010, MNRAS, 402, 895
Wang Q. D. et al., 2013, Science, 341, 981
Weaver R., McCray R., Castor J., Shapiro P., Moore R., 1977, ApJ, 218, 377

Werner N. et al., 2004, A&A, 416, 311
Wijnands R., Miller J. M., Wang Q. D., 2002, ApJ, 579, 422
Yamauchi S., Shimizu M., Nakashima S., Nobukawa M., Tsuru T. G., Koyama K., 2014, PASJ, 66, 1256
Yelda S., Ghez A. M., Lu J. R., Do T., Meyer L., Morris M. R., Matthews K., 2014, ApJ, 783, 131
Yoast-Hull T. M., Gallagher J. S., III, Zweibel E. G., 2014, ApJ, 790, 86
Yusef-Zadeh F., Morris M., 1987a, AJ, 94, 1178
Yusef-Zadeh F., Morris M., 1987b, ApJ, 320, 545
Yusef-Zadeh F., Morris M., 1987c, ApJ, 322, 721
Yusef-Zadeh F., Morris M., 1988, ApJ, 329, 729
Yusef-Zadeh F., Morris M., Chance D., 1984, Nature, 310, 557
Yusef-Zadeh F., Wardle M., Parastaran P., 1997, ApJ, 475, L119
Yusef-Zadeh F., Law C., Wardle M., Wang Q. D., Fruscione A., Lang C. C., Cotera A., 2002, ApJ, 570, 665
Yusef-Zadeh F., Hewitt J. W., Cotton W., 2004, ApJS, 155, 421
Yusef-Zadeh F., Wardle M., Muno M., Law C., Pound M., 2005, Adv. Space Res., 35, 1074
Yusef-Zadeh F., Morris M., 1989, Comments on Astrophysics, 13, 273
Yusef-Zadeh F., Muno M., Wardle M., Lis D. C., 2007, ApJ, 656, 847
Zhang Z.-Y., Gao Y., Henkel C., Oswalt T. D., Tan K. F., Zhang Y., 2014, ApJ, 784, LL31
Zoglauer A. et al., 2015, ApJ, 798, 98

APPENDIX A: XMM–NEWTON OBSERVATIONS

Table A1. List of all *XMM–Newton* observations considered in this work. Exposure Mode: U, S stand for unscheduled and scheduled, respectively. Filters: Med, thn and tck stand for medium, thin and thick filters, respectively. FF, eFF, SW, Ti, TU stand for full frame, extended full frame, small window, timing and time uncompressed, respectively.

OBSID	rev	EPIC-pn Exp Mod	EPIC-pn Exp ID	EPIC-MOS1 Exp Mod	EPIC-MOS1 Exp ID	EPIC-MOS2 Exp Mod	EPIC-MOS2 Exp ID	EPIC-pn Mode	EPIC-pn Filter	EPIC-MOS1 Mode	EPIC-MOS1 Filter	EPIC-MOS2 Mode	EPIC-MOS2 Filter	Threshold pn c/s	Threshold M1 c/s	Threshold M2 c/s
NEW CMZ XMM–Newton scan																
0694640101	2335	S	003	S	001	S	002	FF	med	FF	med	FF	med	6.0	2.0	2.0
0694640201	2335	S	003	S	001	S	002	FF	med	FF	med	FF	med	6.0	2.0	2.0
0694640301	2335	S	003	S	001	S	002	FF	med	FF	med	FF	med	6.0	2.0	2.0
0694640401	2335	S	003	S	001	S	002	FF	med	FF	med	FF	med	8.0	2.5	2.5
0694640501	2335	S	003	S	001	S	002	FF	med	FF	med	FF	med	6.0	2.0	2.0
0694640601	2335	S	003	S	001	S	002	FF	med	FF	med	FF	med	6.0	2.0	2.0
0694640701	2335	S	003	S	001	S	002	FF	med	FF	med	FF	med	6.0	2.0	2.0
0694640801	2335	S	003	S	001	S	002	FF	med	FF	med	FF	med	6.0	2.0	2.0
0694640901	2335	S	003	S	001	S	002	FF	med	FF	med	FF	med	6.0	2.0	2.0
0694641001	2335	S	003	S	001	S	002	FF	med	FF	med	FF	med	6.0	2.0	2.0
0694641101	2335	S	003	S	001	S	002	FF	med	FF	med	FF	med	6.0	2.0	2.0
0694641201	2335	S	003	S	001	S	002	FF	med	FF	med	FF	med	6.0	2.0	2.0
0694641301	2335	S	003	S	001	S	002	FF	med	FF	med	FF	med	6.0	2.0	2.0
0694641401	2335	S	003	S	001	S	002	FF	med	FF	med	FF	med	6.0	2.0	2.0
0694641501	2335	S	003	S	001	S	002	FF	med	FF	med	FF	med	6.0	2.0	2.0
0694641601	2335	S	003	S	001	S	002	FF	med	FF	med	FF	med	6.0	2.0	2.0
OLD CMZ XMM–Newton scan																
0112970101	0145	U	002	U	002	U	002	FF	med	FF	med	FF	med	6.0	2.0	2.0
0112970201	0145	S	003	S	001	S	002	eFF	med	FF	med	FF	med	6.0	2.0	2.0
0112970401	0143	S	003	S	001	S	002	eFF	med	FF	med	FF	med	6.0	2.0	2.0
0112970501	0144	S	003	S	001	S	002	eFF	med	FF	med	FF	med	6.0	2.0	2.0
0112970701	0139	S	003	S	001	S	002	eFF	med	FF	med	FF	med	6.0	2.0	2.0
0112970801	0144	S	003	S	001	S	002	eFF	med	FF	med	FF	med	6.0	1.5	1.5
0112971001	0145	S	003	S	001	S	002	FF	tck	FF	med	FF	med	5.0	1.5	1.5
0112971301	0143	S	003	S	001	S	408	SW	med	TU	med	RF	med	6.0	1.5	1.5
0112971501	0240	S	003	S	001	S	002	eFF	med	FF	med	FF	med	6.0	2.0	2.0
0112971601	0240	S	003	S	001	S	002	eFF	med	FF	med	FF	med	6.0	2.0	2.0
0112971701	0240	S	003	S	011	S	010	SW	med	TU	med	SW	med	6.0	2.0	2.0
0112971801	0240	S	003	S	001	S	002	eFF	med	FF	med	FF	med	6.0	2.0	2.0
0112971901	0240	S	003	S	001	S	002	eFF	med	FF	med	FF	med	5.0	1.5	1.5
0112972101	0318	S	003	S	001	S	002	eFF	med	FF	med	FF	med	6.0	1.5	1.5

Table A1 – *continued*

OBSID	rev	EPIC-pn Exp Mod	EPIC-pn Exp ID	EPIC-MOS1 Exp Mod	EPIC-MOS1 Exp ID	EPIC-MOS2 Exp Mod	EPIC-MOS2 Exp ID	EPIC-pn Mode	EPIC-pn Filter	EPIC-MOS1 Mode	EPIC-MOS1 Filter	EPIC-MOS2 Mode	EPIC-MOS2 Filter	Threshold pn c/s	Threshold M1 c/s	Threshold M2 c/s
							*Pointing towards Sgr A**									
							2002									
0111350101	0406	U	002	S	006	S	005	FF	tck	FF	med	FF	med	6.0	2.0	2.0
0111350301	0516	S	001	S	006	S	005	FF	tck	FF	med	FF	med	6.0	2.0	2.0
							2004									
0202670501	0788	U	002	U	003	U	003	eF	F med	FF	med	FF	med	6.0	2.0	2.0
0202670601	0789	S	003	S	001	S	002	eF	F med	FF	med	FF	med	6.0	2.0	2.0
0202670701	0866	S	003	S	001	S	002	FF	med	FF	med	FF	med	6.0	2.0	2.0
0202670801	0867	S	003	S	001	S	002	FF	med	FF	med	FF	med	6.0	1.5	1.5
							2006									
0302882601	1139	S	003	S	001	S	002	FF	med	FF	med	FF	med	6.0	2.0	2.0
0302884001	1236	S	003	S	001	S	002	FF	med	FF	med	FF	med	7.0	2.0	2.0
							2007									
0402430301	1339	S	001	S	002	S	003	FF	med	FF	med	FF	med	8.0	2.0	2.0
0402430401	1340	U	002	U	002	U	002	FF	med	FF	med	FF	med	8.0	2.0	2.0
0402430701	1338	S	001	S	002	S	003	FF	med	FF	med	FF	med	8.0	2.0	2.0
0504940201	1418	S	003	S	001	S	002	FF	med	FF	med	FF	med	8.0	2.0	2.0
							2008									
0511000301	1508	S	003	S	001	S	002	FF	thn	FF	thn	FF	thn	7.0	2.0	2.0
0511000401	1610	S	003	U	002	U	002	FF	thn	FF	thn	FF	thn	7.0	2.5	2.5
0505670101	1518	U	002	U	002	U	002	FF	med	FF	med	FF	med	8.0	2.0	2.0
							2009									
0554750401	1705	S	003	S	001	S	002	FF	med	FF	med	FF	med	8.0	2.5	2.5
0554750501	1706	S	003	S	001	S	002	FF	med	FF	med	FF	med	8.0	2.5	2.5
0554750601	1707	U	002	S	001	S	002	FF	med	FF	med	FF	med	8.0	2.5	2.5
							2011									
0604300601	2069	S	003	S	001	S	002	FF	med	FF	med	FF	med	7.0	2.0	2.0
0604300701	2070	U	002	S	001	S	002	FF	med	FF	med	FF	med	7.0	2.0	2.0
0604300801	2071	U	002	U	002	U	002	FF	med	FF	med	FF	med	8.0	2.0	2.0
0604300901	2072	S	003	S	001	S	002	FF	med	FF	med	FF	med	7.0	2.0	2.0
0604301001	2073	S	003	S	001	S	002	FF	med	FF	med	FF	med	7.0	2.0	2.0
0658600101	2148	S	001	S	002	S	003	FF	med	FF	med	FF	med	8.0	2.5	2.5
0658600201	2148	S	001	S	002	S	003	FF	med	FF	med	FF	med	7.0	1.8	1.8
							2012									
0674600601	2245	S	003	S	001	S	002	FF	med	FF	med	FF	med	7.0	2.0	2.0
0674600701	2246	S	003	S	001	S	002	FF	med	FF	med	FF	med	7.0	2.0	2.0
0674600801	2248	S	003	S	001	S	002	FF	med	FF	med	FF	med	6.0	1.8	1.8
0674601001	2249	S	003	S	001	S	002	FF	med	FF	med	FF	med	7.0	1.8	1.8
0674601101	2247	S	003	U	002	U	002	FF	med	FF	med	FF	med	6.0	2.0	2.0

Note. c/s is counts (photons) per second.

Table A2. List of all *XMM–Newton* observations considered in this work. Exposure Mode: U, S stand for unscheduled and scheduled, respectively. Filters: Med, thn, tck stand for medium, thin and thick filters, respectively. FF, eFF, SW, Ti, TU stand for full frame, extended full frame, small window, timing and time uncompressed, respectively.

OBSID	rev	EPIC-pn		EPIC-MOS1		EPIC-MOS2		EPIC-pn		EPIC-MOS1		EPIC-MOS2		Threshold		
		Exp Mod	Exp ID	Exp Mod	Exp ID	Exp Mod	Exp ID	mode	filter	mode	filter	mode	filter	pn c/s	M1 c/s	M2 c/s
Other observations of the CMZ																
0030540101	0504	S	003	S	001	S	002	SW	tck	SW	tck	SW	tck	6.0	2.0	2.0
0144220101	0596	U	002	U	002	U	002	SW	med	FF	med	FF	med	6.0	1.5	1.5
0152920101	0607	S	003	S	001	S	002	FF	tck	FF	tck	FF	tck	6.0	1.5	1.5
0144630101	0688	S	003	S	001	S	002	SW	med	TU	med	SW	med			
0203930101	0868	S	003	S	001	S	002	eF	F med	FF	med	FF	med	6.0	1.5	1.5
0205240101	0956	S	003	S	001	S	002	FF	med	FF	med	FF	med	6.0	1.5	1.5
0304220301	1048	S	004	S	002	S	003	SW	med	FF	med	FF	med	6.0	1.5	1.5
0304220101	1063	S	003	S	001	S	002	SW	med	FF	med	FF	med	6.0	1.5	1.5
0303210201	1065	S	003	S	001	S	002	SW	med	TU	med	TU	med	6.0	1.5	1.5
0302882501	1139	S	003	S	001	S	002	FF	med	FF	med	FF	med	6.0	2.0	2.0
0302882701	1139	S	003	S	001	S	002	FF	med	FF	med	FF	med	6.0	2.0	2.0
0302882801	1139	S	003	S	001	S	002	FF	med	FF	med	FF	med	6.0	2.0	2.0
0302882901	1139	S	003	S	001	S	002	FF	med	FF	med	FF	med	6.0	2.0	2.0
0302883001	1139	S	003	S	001	S	002	FF	med	FF	med	FF	med	6.0	2.0	2.0
0302883101	1139	S	003	S	001	S	002	FF	med	FF	med	FF	med	6.0	2.0	2.0
0302883201	1139	S	003	S	001	S	002	FF	med	FF	med	FF	med	6.0	2.0	2.0
0305830701	1157	S	003	S	001	S	002	FF	med	FF	med	FF	med	6.0	1.5	1.5
0302883901	1236	S	003	S	001	S	002	FF	med	FF	med	FF	med	6.0	2.0	2.0
0302884101	1236	S	003	S	001	S	002	FF	med	FF	med	FF	med	6.0	2.0	2.0
0302884201	1236	S	003	S	001	S	002	FF	med	FF	med	FF	med	6.0	2.0	2.0
0302884301	1236	S	003	S	001	S	002	FF	med	FF	med	FF	med	6.0	2.5	2.5
0302884401	1236	S	003	S	001	S	002	FF	med	FF	med	FF	med	6.0	2.0	2.0
0302884501	1236	S	003	S	001	S	002	FF	med	FF	med	FF	med	6.0	2.0	2.0
0406580201	1241	S	003	S	001	S	002	FF	med	FF	med	FF	med	6.0	2.0	2.0
0410580401	1243	N	000	S	002	S	003	Ti	tck	FF	tck	TU	tck	6.0	2.0	2.0
0410580501	1245	N	000	S	002	S	003	Ti	tck	FF	tck	TU	tck	6.0	2.0	2.0
0400340101	1244	S	003	S	001	S	002	FF	med	FF	med	FF	med	6.0	2.0	2.0
0506291201	1322	N	000	S	001	S	002	Ti	med	FF	med	FF	med	6.0	2.0	2.0
0504940101	1418	S	003	S	001	S	002	FF	med	FF	med	FF	med	6.0	2.0	2.0
0504940401	1418	S	003	S	001	S	002	FF	med	FF	med	FF	med	6.0	2.0	2.0
0504940501	1418	S	003	S	001	S	002	FF	med	FF	med	FF	med	6.0	2.0	2.0
0504940601	1418	S	003	S	001	S	002	FF	med	FF	med	FF	med	7.0	2.0	2.0
0504940701	1418	S	003	S	001	S	002	FF	med	FF	med	FF	med	6.0	2.0	2.0
0511010701	1505	S	003	S	001	S	002	FF	med	FF	med	FF	med	6.0	2.5	2.5
0511000101	1508	S	003	S	001	S	002	FF	thn	FF	thn	FF	thn	6.0	2.0	2.0
0511000501	1508	S	003	S	001	S	002	FF	thn	FF	thn	FF	thn	6.0	2.0	2.0
0511000701	1508	S	003	S	001	S	002	FF	thn	FF	thn	FF	thn	6.0	2.0	2.0
0511000901	1508	S	003	S	001	S	002	FF	thn	FF	thn	FF	thn	6.0	2.5	2.5
0511001101	1508	S	003	S	001	S	002	FF	thn	FF	thn	FF	thn	6.0	2.5	2.5
0511001301	1508	S	003	S	001	S	002	FF	thn	FF	thn	FF	thn	6.0	2.0	2.0
0511000201	1510	S	003	S	001	S	002	FF	thn	FF	thn	FF	thn	6.0	2.5	2.5
0511000601	1510	S	003	S	001	S	002	FF	thn	FF	thn	FF	thn	6.0	2.5	2.5
0511000801	1512	S	003	S	001	S	002	FF	thn	FF	thn	FF	thn	6.0	2.5	2.5
0511001001	1512	S	003	S	001	S	002	FF	thn	FF	thn	FF	thn	6.0	2.5	2.5
0511001201	1512	S	003	S	001	S	002	FF	thn	FF	thn	FF	thn	8.0	2.5	2.5
0511001401	1512	S	003	S	001	S	002	FF	thn	FF	thn	FF	thn	6.0	2.5	2.5
0505870301	1511	S	003	S	001	S	002	FF	med	FF	med	FF	med	6.0	2.0	2.0
0603850201	1891	S	003	S	001	S	002	FF	med	FF	med	FF	med	6.0	2.0	2.0
0655670101	2065	N	000	S	001	S	002	Ti	med	FF	med	FF	med	6.0	2.0	2.0

Note. c/s is counts (photons) per second.

Table A3. List of all *XMM–Newton* observations considered in this work. Total and cleaned exposure time (in seconds) for each camera, respectively.

OBSID	obs date	Exp pn	Exp M1	Exp M2	Exp pn	Exp M1	Exp M2
			NEW CMZ XMM–Newton scan				
0694640101	2012-09-07	41 978	43 452	43 605	38 739	38 980	38 985
0694640201	2012-08-30	45 035	46 616	46 619	45 038	46 616	46 619
0694640301	2012-08-31	40 041	41 616	41 619	40 041	41 616	41 619
0694640401	2012-09-02	52 954	51 442	51 460	38 736	40 073	40 075
0694640501	2012-09-05	44 976	46 606	46 621	32 935	33 180	33 185
0694640601	2012-09-06	40 042	41 614	41 621	40 042	41 614	41 621
0694640701	2012-10-02	42 539	44 099	44 120	42 539	44 117	44 120
0694640801	2012-10-06	40 041	41 616	41 619	40 041	41 616	41 619
0694640901	2012-09-12	43 031	44 617	44 604	42 202	43 784	43 786
0694641001	2012-09-23	46 021	47 607	47 620	46 041	47 614	47 620
0694641101	2012-09-24	40 041	41 616	41 619	40 041	41 616	41 619
0694641201	2012-09-26	40 008	41 559	41 577	40 008	41 588	41 598
0694641301	2012-09-26	53 842	56 260	56 348	46 667	48 012	48 018
0694641401	2012-09-30	45 816	46 751	46 920	32 466	33 767	33 770
0694641501	2012-10-06	49 746	51 483	51 486	39 167	40 518	40 507
0694641601	2012-10-08	40 005	41 585	41 585	27 250	27 795	27 803
			OLD CMZ XMM–Newton scan				
0112970101	2000-09-23	12 870	15 806	15 611	12 252	14 679	14 637
0112970201	2000-09-23	13 499	17 394	17 392	12 999	16 894	16 892
0112970401	2000-09-19	25 411	29 365	29 391	21 880	23 849	23 847
0112970501	2000-09-21	21 119	24 914	24 911	10 289	14 084	14 081
0112970701	2000-09-11	19 518	23 419	23 413	19 383	23 221	23 218
0112970801	2000-09-21	19 969	23 892	23 892	13 462	17 198	17 198
0112971001	2000-09-24	12 599	16 492	16 482	8774	12 529	12 529
0112971301	2000-09-19	12 800	0	13 091	0	0	0
0112971501	2001-04-01	20 293	25 020	25 017	6752	7017	7017
0112971601	2001-03-31	0	3996	3949	0	0	0
0112971701	2001-03-31	11 000	0	11 799	0	0	0
0112971801	2001-04-01	9927	14 513	14 542	1900	2069	2069
0112971901	2001-04-01	4698	9191	9191	4147	8379	8379
0112972101	2001-09-04	21 687	26 039	26 055	20 130	23 515	3517
			*Pointing towards Sgr A**				
0111350101	2002-02-26	40 030	52 105	52 120	40 030	52 118	52 120
0111350301	2002-10-03	15 377	16 960	16 996	8261	9877	9880
			2004				
0202670501	2004-03-28	110 170	5733	6087	45 847	0	0
0202670501	2004-03-28	0	107 784	108 572	0	0	0
0202670501	2004-03-30	0	650	848	0	0	0
0202670601	2004-03-30	112 204	585	538	56 926	0	0
0202670601	2004-03-30	0	120 863	122 251	0	0	0
0202670701	2004-08-31	127 470	132 469	132 503	78 857	78 921	78 915
0202670801	2004-09-02	130 951	132 997	133 036	91 795	93 131	93 126
			2006				
0302882601	2006-02-27	4937	6563	6568	1700	3160	3163
0302884001	2006-09-08	4987	6563	6570	4787	6365	6370
			2007				
0402430301	2007-04-01	101 319	93 947	94 022	50 962	50 955	50 958
0402430401	2007-04-03	93 594	97 566	96 461	36 886	36 892	36 876
0402430701	2007-03-30	32 338	33 912	33 917	21 240	22 820	22 825
0504940201	2007-09-06	11 092	12 649	12 652	7392	8949	8960
			2008				
0511000301	2008-03-03	5057	6615	6620	3305	4863	4868
0511000401	2008-09-23	5058	4358	4342	5058	4358	4342
0505670101	2008-03-23	96 601	97 787	97 787	64 200	65 143	65 153

Table A3 – *continued*

OBSID	obs date	Exp pn	Exp M1	Exp M2	Exp pn	Exp M1	Exp M2
			2009				
0554750401	2009-04-01	38 034	39 614	39 619	31 934	33 358	33 363
0554750501	2009-04-03	42 434	44 016	44 018	38 634	40 216	40 218
0554750601	2009-04-05	32 837	38 816	38 818	31 485	37 464	37 466
			2011				
0604300601	2011-03-28	45 306	48 467	48 491	28 768	30 121	30 119
0604300701	2011-03-30	42 305	48 579	48 584	32 872	39 149	39 156
0604300801	2011-04-01	37 321	38 642	38 494	33 771	36 149	36 129
0604300901	2011-04-03	36 568	37 589	37 573	19 941	21 140	21 143
0604301001	2011-04-05	48 210	47 757	47 646	32 571	33 917	33 914
0658600101	2011-08-31	47 585	49 169	49 159	47 653	49 169	49 177
0658600201	2011-09-01	51 324	52 903	52 908	39 634	41 109	41 115
			2012				
0674600601	2012-03-13	19 594	21 167	21 172	8594	9296	9301
0674600701	2012-03-15	14 040	15 616	15 618	6802	8209	8212
0674600801	2012-03-19	21 041	22 615	22 618	16 784	18 358	18 358
0674601001	2012-03-21	22 034	23 616	23 619	19 841	21 416	21 419
0674601101	2012-03-17	25 682	24 638	24 628	8956	8173	8178

Table A4. List of all *XMM–Newton* observations considered in this work. Total and cleaned exposure time (in seconds) for each camera, respectively.

OBSID	obs date	Exp pn	Exp M1	Exp M2	Exp pn	Exp M1	Exp M2
			Other observations of the CMZ				
0030540101	2002-09-09	27 689	27 842	27 844	27 339	27 495	27 494
0144220101	2003-03-12	46 746	49 905	49 843	28 820	31 550	31 461
0152920101	2003-04-02	50 182	51 639	51 774	48 486	50 082	50 097
0144630101	2003-09-11	8469	0	8661	0	316	311
0203930101	2004-09-04	46 544	50 438	50 446	39 078	43 003	43 013
0205240101	2005-02-26	46 919	50 625	50 604	14 946	15 251	15 243
0304220301	2005-08-29	20 031	20 213	20 226	6417	6615	6620
0304220101	2005-09-29	8051	8237	8250	5621	5816	5821
0303210201	2005-10-02	23 472	0	0	23	314	315
0302882501	2006-02-27	7561	9176	9178	6364	7999	8002
0302882701	2006-02-27	5237	6851	6869	2937	4564	4569
0302882801	2006-02-27	5937	7558	7571	5537	7164	7171
0302882901	2006-02-27	5936	7566	7569	4437	6066	6069
0302883001	2006-02-27	5937	7540	7558	3137	4766	4771
0302883101	2006-02-27	9814	11 432	11 448	8614	10 248	10 258
0302883201	2006-03-29	4896	6518	6526	3898	5547	5539
0305830701	2006-04-04	6399	11 266	11 256	0	1028	1028
0302883901	2006-09-08	4987	6565	6568	4787	6365	6368
0302884101	2006-09-08	4987	6565	6570	4000	5578	5583
0302884201	2006-09-08	4987	6565	6570	4987	6565	6570
0302884301	2006-09-09	4987	6565	6568	4987	6565	6568
0302884401	2006-09-09	4036	5616	5621	4037	5616	5621
0302884501	2006-09-09	6787	8364	8370	6787	8364	8369
0406580201	2006-09-18	28 034	29 607	29 609	13 896	14 809	14 814
0410580401	2006-09-22	0	32 558	0	0	32 367	32 326
0410580501	2006-09-26	0	32 116	0	0	30 108	30 096
0400340101	2006-09-24	40 001	41 575	41 580	16 312	17 481	17 486
0506291201	2007-02-27	0	38 616	38 621	0	30 937	30 937
0504940101	2007-09-06	5058	6615	6620	4958	6515	6520
0504940401	2007-09-06	5058	6615	6620	5058	6615	6620
0504940501	2007-09-06	5057	6615	6620	5006	6563	6568
0504940601	2007-09-06	5058	6615	6620	1720	3175	3181
0504940701	2007-09-06	5058	6615	6620	4558	6115	6120
0511010701	2008-02-27	7455	9004	9004	5803	7362	7368
0511000101	2008-03-03	6943	8500	8500	546	796	800
0511000501	2008-03-04	5058	6615	6620	4658	6215	6220
0511000701	2008-03-04	5058	6615	6620	4506	6063	6068
0511000901	2008-03-04	5058	6615	6620	5058	6514	6518
0511001101	2008-03-04	5057	6615	6620	5057	6615	6620
0511001301	2008-03-04	5058	6615	6620	3800	5132	5137
0511000201	2008-09-23	5058	6615	6620	5058	6615	6620
0511000601	2008-09-23	5058	6615	6620	5058	6615	6620
0511000801	2008-09-27	5035	6602	6620	5035	6615	6620
0511001001	2008-09-27	5034	6615	6620	5034	6615	6620
0511001201	2008-09-27	5034	6615	6620	5034	6615	6620
0511001401	2008-09-27	5034	6615	6620	5034	6615	6620
0505870301	2008-03-10	29 885	31614	31 494	7249	7250	7255
0603850201	2010-04-07	22 503	21 643	21 663	16 919	18 271	18 266
0655670101	2011-03-19	0	103 934	103 954	0	80 716	80 729

This paper has been typeset from a TEX/LATEX file prepared by the author.